Damping of Coherent Oscillations in Intense Ion Beams

Dämpfung von kohärenten Schwingungen in intensiven Ionenstrahlen
Zur Erlangung des Grades eines Doktors der Naturwissenschaften (Dr. rer. nat.)
genehmigte Dissertation von M.Sc. Ivan Karpov aus Irkutsk
Tag der Einreichung: 6. 12. 2016, Tag der Prüfung: 6. 02. 2017
Darmstadt 2017 — D 17

1. Gutachten: Prof. Dr. rer. nat. Oliver Boine-Frankenheim TU Darmstadt
2. Gutachten: Prof. Dr. Shaukat Khan TU Dortmund

TECHNISCHE
UNIVERSITÄT
DARMSTADT

Fachbereich 18 -
Elektrotechnik und
Informationstechnik
Institut für Theorie
Elektromagnetischer Felder

Damping of Coherent Oscillations in Intense Ion Beams
Dämpfung von kohärenten Schwingungen in intensiven Ionenstrahlen

Genehmigte Dissertation von M.Sc. Ivan Karpov aus Irkutsk

1. Gutachten: Prof. Dr. rer. nat. Oliver Boine-Frankenheim TU Darmstadt
2. Gutachten: Prof. Dr. Shaukat Khan TU Dortmund

Tag der Einreichung: 6. 12. 2016
Tag der Prüfung: 6. 02. 2017

Darmstadt 2017 — D 17

Bitte zitieren Sie dieses Dokument als:
URN: urn:nbn:de:tuda-tuprints-59835
URL: http://tuprints.ulb.tu-darmstadt.de/5983

Erklärung zur Dissertation

Hiermit versichere ich, die vorliegende Dissertation ohne Hilfe Dritter nur mit den angegebenen Quellen und Hilfsmitteln angefertigt zu haben. Alle Stellen, die aus Quellen entnommen wurden, sind als solche kenntlich gemacht. Diese Arbeit hat in gleicher oder ähnlicher Form noch keiner Prüfungsbehörde vorgelegen.

Darmstadt, den Dezember 6, 2016

(Ivan Karpov)

Zusammenfassung

Die Dekohärenz eines transversal versetzten Ionenpakets ist ein wichtiger strahldynamischer Vorgang in Synchrotronen und Speicherringen. Ein Versatz kann durch einen Injektionsfehler nach der Paket-zu-Paket Übergabe zwischen Synchrotronen oder durch einen extern erzeugten Kraftstoß entstehen. Dekohärenz führt zur transversalen Emittanzvergrößerung, die Strahlverluste und eine Verminderung der Strahlqualität verursachen kann. Um die Aufweitung des Strahls zu verhindern, kann ein transversales Rückwirkungssystem oder "Transverse Feedback System" (TFS) verwendet werden. Die TFS-Dämpfungszeit sollte kürzer sein als die charakteristische Dekohärenzzeit, die stark durch das Zusammenspiel unterschiedlicher Intensitätseffekte (z. B. Raumladung und Impedanzen) beeinflusst wird.

Diese Arbeit beschreibt die Entwicklung analytischer Modelle, welche Dekohärenz und Emittanzvergrößerung unter Berücksichtigung von Chromatizität, Raumladung und Spiegelladungen innerhalb der ersten Synchrotronschwingungsperiode wiedergeben. Eine Pulsantwortfunktion unter Berücksichtigung von Intensitätseffekten wird aus einem Modell für die Strahlübertragungsfunktion abgleitet. Im Falle eines Gleichstromtrahls zeigt das zweidimensionale analytische Modell, dass die Raumladung die Dekohärenz verlangsamt und oberhalb einer Schwellintensität vollständig unterdrückt. Die Vorhersagen der analytischen Modelle wurden durch Simulationen der Teichlendynamik mit den selbstkonsistenten Raumladungsfeldern bestätigt. Zusätzlich wurde die Entstehung eines Halos und die Strahlverluste während der Dekohärenz in den Simulationen beobachtet. Unter Verwendung eines nicht-selbstkonsistenten Teilchen-Kern-Modells wurden diese Effekte erfolgreich interpretiert.

Das zweidimensionale analytische Modell wurde auf den Fall der Teilchenpakete erweitert. Die Simulationsergebnisse reproduzieren die analytischen Vorhersagen. Die Schwellintensitäten der Dekohärenzabschwächung sind höher im Vergleich zum Gleichstromtrahl, die Spiegelladungen können aber die Dekohärenz wiederherstellen.

Im Rahmen der Arbeit wurden dedizierte Experimente am SIS18-Synchrotron an der GSI Darmstadt durchgeführt, die Ergebnisse wurden mit Simulationen und analytischen Vorhersagen verglichen. Der Beitrag von Nichtlinearitäten und Spiegelladungen ist vernachlässigbar, während die Chromatizität und die Raumladung die Dekohärenz bestimmen.

Zur Untersuchung der Dämpfungseffizienz eines Rückwirkungssystem wurde ein umfangreiches TFS-Modul für die numerischen Simulationen entwickelt. Die TFS-Bandbreite sollte das charakteristische Spektrum des Strahles umfassen, wobei die Intensitätseffekte berücksichtigt werden müssen. Schwellwerte der Verzögerungsfehler, die eine Instabilität des Strahls verursachen können, und der Rauschenpegel, der zur Emittanzvergrößerung führt, wurden bestimmt.

Abstract

Transverse decoherence of a displaced ion bunch is an important phenomenon in synchrotrons and storage rings. An offset can be caused by an injection error after the bunch-to-bucket transfer between synchrotrons or by an externally generated kick. Decoherence results in a transverse emittance blowup, which can cause particle losses and a beam quality degradation. To prevent the beam blowup, a transverse feedback system (TFS) can be used. The damping time should be shorter than the characteristic decoherence time, which can be strongly affected by the interplay of different intensity effects (e.g., space charge and impedances).

This thesis describes the development of the analytical models that explain decoherence and emittance growth with chromaticity, space charge, and image charges within the first synchrotron period. The pulsed response function including intensity effects was derived from the model for beam transfer functions. For a coasting beam, the two-dimensional model shows that space charge slows down and above intensity threshold suppresses decoherence. These predictions were confirmed by particle tracking simulations with self-consistent space charge fields. Additionally, halo buildup and losses during decoherence were observed in simulations. These effects were successfully interpreted using a non self-consistent particle-core model.

The two-dimensional model was extended to the bunched beams. The simulation results reproduce the analytical predictions. The intensity threshold of decoherence suppression is higher in comparison to a coasting beam, image charges can restore decoherence.

In the present work dedicated experiments were performed in the SIS18 synchrotron at GSI Darmstadt and the results were compared with simulations and analytical predictions. The contribution of nonlinearities and image charges is negligible while chromaticity and space charge dominate decoherence.

To study the damping efficiency of TFS, a comprehensive TFS module was developed for simulations. The system bandwidth should cover the characteristic spectrum including intensity effects. Delay errors, which can cause a beam instability, and the level of noise, which results in an emittance blowup, were determined.

Contents

1 Introduction

Since the first half of the 20th century, particle accelerators play an important role for the development of science and technology in modern society. About two-third of the accelerator systems have applications in industry such as material processing, treatment, and analysis [1]. Others are widely used for radioisotope production for various medical tests in nuclear medicine and produce particle beams for cancer therapy [1, 2]. Of about 30,000 particle accelerators at work worldwide, less than a fraction of a percent are scientific research and discovery machines [3]. The problem of the finite breakdown voltage – one of the limiting factors of electrostatic accelerators [4] – initiated the development of oscillating field linear particle accelerators (linacs) [5] and different types of circular accelerators [6]. After the invention of the synchrotron [7, 8, 9] and discovery of the strong-focusing principle [10], it was possible to construct high-energy high-intensity facilities.

1.1 Synchrotrons

In synchrotrons, each component serves a specific purposes (Fig. 1.1):

- the dipole magnets are used to bend the particle trajectory in a fixed closed-loop path,
- the quadrupole magnets confine a particle beam in the transverse plane,
- the rf cavities generate the alternating electric field for particle acceleration,
- the septum magnets are used for injection and extraction processes.

During the acceleration process a particle beam moves on the same trajectory by means of synchronous adjustment of the rf frequency and the magnetic field strength. Particles pass through rf cavities with a proper phase with respect to the longitudinal electric field. In this case, it is not possible to accelerate a continuous beam and particles are grouped longitudinally in a number of bunches.

In the longitudinal plane, particles are confined by the potential imposed by rf cavities and perform synchrotron oscillations. In the transverse plane, particles pass through alternating field gradients which lead to transverse oscillations (betatron oscillations) with a location-dependent amplitude. The number of transverse/longitudinal oscillations per revolution is called a betatron/synchrotron tune. These single-particle oscillations are referred as incoherent oscillations.

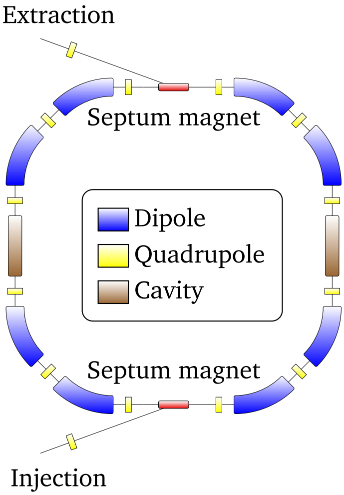

Figure 1.1.: A sketch of a synchrotron. The particle trajectory is bent by dipole magnets. The transverse focusing is maintained by quadrupole magnets. An acceleration is given by rf cavities. The septum magnets are used for beam transport source-synchrotron or synchrotron-experiments.

The inability of synchrotrons to accelerate particles from zero kinetic energy requires an injection of the pre-accelerated particle beams. This can be realized by an accelerator chain containing different structures like particle sources, linacs, and other synchrotrons. For example, at GSI Helmholtzzentrum für Schwerionenforschung GmbH (GSI), protons (or ions) generated in the ion source are accelerated in the UNIversal Linear ACcelerator (UNILAC) [11] and transported to the Schwerionensynchrotron 18 (SIS18) [12] for further acceleration. For the upcoming Facility for Antiproton and Ion Research (FAIR) at GSI (Fig. 1.2), SIS18 will serve as a booster for the Schwerionensynchrotron 100 (SIS100) and a single-turn injection scheme will be used [13]. In this scheme, at the end of the transfer line the bunch is deflected by the special type septum magnet [15] onto the designed orbit at the center of the kicker. Then the kicker magnet compensates the remaining angle and the beam follows the designed orbit (Fig. 1.3).

The synchronization errors or beam energy errors result in a non-fully compensated angle after injection. This is equivalent to the situation in which a whole beam or a part of the beam experiences the transverse kick that changes the transverse velocity of all particles. These particles will oscillate collectively following the initial kick. Thus, additionally to the incoherent oscillations there are coherent oscillations of the beam. The interplay of both incoherent and coherent oscillations can lead to beam blowup and particle losses. The former is crucial for the experiments that require dense beams with small transverse dimensions. The latter can result in activation of the accelerator

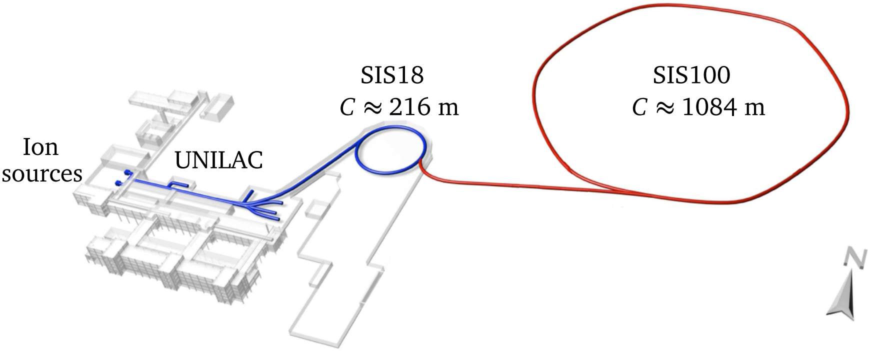

Figure 1.2.: The SIS18 - SIS100 part of the accelerator chain of the FAIR project at GSI. Particles generated by the ion sources are accelerated by UNILAC. Reaching kinetic energy of 11.4 MeV/u they are transported to the booster synchrotron SIS18. For one of the reference scenario, after the acceleration up to 200 MeV/u $^{238}U^{28+}$ bunches are injected to the main synchrotron SIS100. The experiments are not shown (figure from [14]).

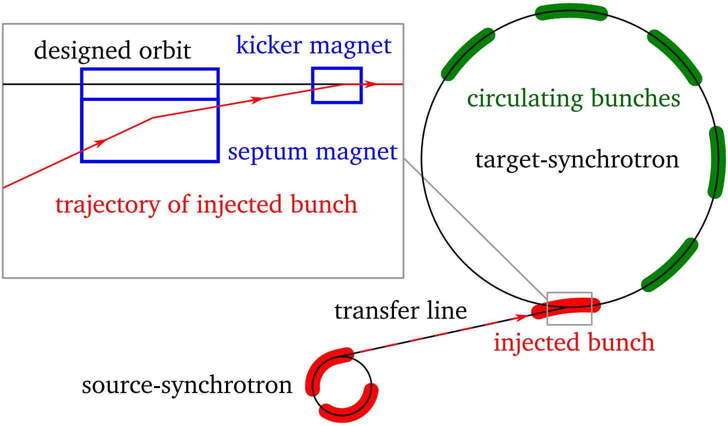

Figure 1.3.: A sketch of the single-turn injection process. The bunch transported from the source synchrotron is deflected by the septum magnet. Crossing the designed orbit at the position of the kicker, its transverse angle is corrected.

components, vacuum degradation, and a quench of superconducting magnets [16, 17, 18, 19].

1.2 Beam blowup due to decoherence after injection or kick

A particle performing the betatron oscillations moves in the transverse phase space. The area of the phase space occupied by all particles of the beam is called the transverse beam emittance ϵ. This quantity describes the beam quality. For example, at any location in the accelerator the transverse beam size is proportional to $\sqrt{\epsilon}$.

Any particle beam has the energy spread and the finite transverse size defined by the particle transverse beam emittance. The transverse restoring force of the focusing magnets depends on the particle energy and can also depend on the transverse position. A change of the restoring force results in a change of the oscillation frequency. Thus, the beam has a spread of betatron oscillation frequencies by means of chromaticity and transverse nonlinearities.

An injection error or an initial kick corresponds to the displacement of the beam in the phase space. Without frequency spread, the beam will perform coherent oscillations and the beam emittance will not change. In the presence of a frequency spread, particles will redistribute in the phase space occupying a larger area, and the transverse emittance will blow up. Particle mixing in phase space also leads to turn-by-turn reduction of the total bunch offset. This process is called transverse decoherence.

In different accelerators there are different ranges of the acceptable beam blowup and losses. For example, at the European Organization for Nuclear Research (CERN), in the Proton Synchrotron (PS), which has similar beam parameters as SIS100, particle losses after injection should be below 5%. In the Large Hadron Collider (LHC) [20], the requirements are more challenging because of high energy stored in the beam (362 MJ per beam).

1.3 Contribution of intensity effects

New advanced experiments demand high-intensity and high-quality beams. Such beams should have small transverse emittances and contain a large number of particles. For low- and medium energy accelerators, collisionless interactions between particles via self-fields and interaction with beam surroundings become important. They can be described in terms of transverse space charge and transverse impedances, correspondingly. The space charge forces change the incoherent frequencies in the beam and produce an additional frequency spread. Transverse impedances change the coherent frequency and can lead to beam instabilities.

The contribution of both effects is foreseen for the SIS100 synchrotron, because of a high beam intensity and a large transverse beam size compared to the accelerator beam pipe. Under these conditions, transverse space charge can significantly change the decoherence process. Usage of superconducting magnets defines challenging requirements for the acceptable beam blowup and losses in the SIS100.

1.4 Transverse feedback systems

Transverse feedback systems serve two main purposes: to damp beam instabilities originated from interaction of the beam with its surroundings [21, 22, 23] and to damp injection errors [24, 25, 26]. The former is considered to be a long term operation where the characteristic time of the process exceeds or in the order of the synchrotron period. The latter is described here in more detail.

To damp the injection errors, the transverse feedback systems perform the following steps during its operation (Fig. 1.4):

- the pick-ups collect the signals induced by a beam with a transverse displacement,
- the detected signals are processed in order to generate the correction signal that is proportional to the transverse velocity of the beam at the position of the kicker,
- after a time delay, the kicker applies the signal that causes damping of coherent beam oscillations.

Varying the strength of the correction signal, the characteristic damping time can be adjusted such that the active damping is faster than the decoherence process. In this case, the transverse beam emittance can be preserved.

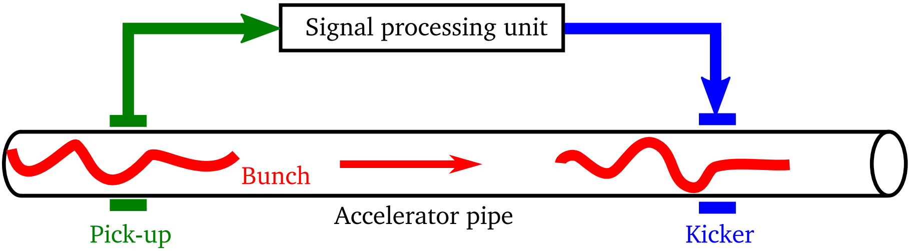

Figure 1.4.: The principle of the transverse feedback systems. The transverse displacement of the beam is detected by pick-ups and then transmitted to the signal processing unit. After the time delay, the correction signal is applied to the same bunch.

1.5 Current status and motivation

A slower decoherence with chromaticity and space charge was observed during the injection process of proton bunches in the Proton Synchrotron (PS) at CERN [26]. It was also demonstrated in particle tracking simulations [27] and was referred as the loss of Landau damping [28, 29, 30]. An attempt to describe decoherence in bunches with space charge was presented in Ref. [31]. The analytical model is based on the space change tune spread due to variation of the local particle density along the bunch.

Recently, a new approach was applied to describe the long-term behavior of decoherence and recoherence following a small initial offset [32, 33]. The initial kick can be represented as a combination of bunch head-tail eigenmodes, which are prone to different Landau damping rates. This approach predicts that after a transition time a mixture of the remaining eigenmodes continues to oscillate, exhibiting a characteristic time pattern.

The effect of impedances on the decoherence process is discussed in Ref. [34]. The developed 2D approach for bunches in the case of constant imaginary impedances shows a slower decoherence for higher beam intensity. Furthermore, this approach was expanded by the two-particle model in Ref. [35] to obtain bunch offset evolution in assumption of a small chromaticity tune spread compared to the synchrotron tune.

The emittance growth after an initial offset in the presence of space charge and image charges was discussed by Reiser [36, 37]. The role of space charge and its interplay with other intensity effects, which is important for the design of the SIS100 synchrotron as part of the FAIR project [38], still needs to be clarified.

Most experimental and theoretical work concerning transverse feedback systems are dedicated to damping of beam instabilities. For example, simulation and theoretical results describing the efficiency of feedback systems for interplay with chromaticity and different impedances were recently discussed in Ref. [39]. The damping of injection errors in the presence of space charge and TFS imperfections has not been studied in detail.

This work addresses the development of the analytical models for the initial stage of the decoherence process in intense ion bunches affected by interplay of chromaticity, space charge, and image charges for arbitrary offsets. We also focus on the short term operation of the transverse feedback systems (i.e. damping of injection errors) in the presence of space charge and TFS imperfections (limited system bandwidth, delay errors, and noise).

1.6 Overview of the thesis

In Chap. 2 basic concepts of particle beam dynamics in synchrotrons are introduced. It builds the theoretical background that is used in this thesis. Consideration of transverse decoherence and emittance blowup due to chromaticity for low-intensity beams is presented in Chap. 3. Chap. 4 makes the reader familiar with modification of the initial stage of decoherence due to space charge and image charges. Starting with case of coasting beams, we develop the model based on the modified pulse response function to describe the decoherence process. The extended model is applied for the bunched beams during the initial stage of decoherence where synchrotron motion can be neglected. After the intensity threshold, we demonstrate the significant contribution of image charges. To validate the analytical models, we use particle tracking simulations with self-consistent field calculations. The necessary details of the computational model are introduced in Chap. 5 and the results are presented in Chap. 6. In simulations we also show the halo buildup during the decoherence process and derive the particle-core model in Sec. 6.2.

In Chap. 7 we discuss measurements in the SIS18 synchrotron at GSI. After the description of the experimental setup, we point out the main effects that contribute to the decoherence process in our measurements and show comparisons with simulations. Finally, Chap. 8 makes the reader familiar with an active damping of the injection errors. We describe implementation of transverse feedback system imperfections and their contribution to the emittance preservation.

The thesis concludes with the summary of results and an outlook in Chap. 9.

2 Basic beam dynamics and intensity effects in synchrotrons

2.1 Transverse beam dynamics

In particle accelerators, the motion of a particle with charge q, velocity $\vec{v}$, and mass m is governed by the Lorentz force [40]

$$\vec{F} = q\left(\vec{E} + \vec{v} \times \vec{B}\right) = \frac{\mathrm{d}\vec{p}}{\mathrm{d}t}, \tag{2.1}$$

where $\vec{E}$ is the electric field, $\vec{B}$ is the magnetic field, $\vec{p} = \gamma m \vec{v}$ is the particle momentum, $\gamma = (1-\beta^2)^{-1/2}$ is the relativistic factor, $\beta = v/c$, and c is the speed of light. In a constant magnetic field with strength B, a particle circulates around an accelerator with a radius ρ that satisfies the relation

$$B\rho = \frac{p}{q}. \tag{2.2}$$

The quantity $B\rho$ – the *magnetic rigidity* – reflects the energy of the accelerated particles in the synchrotron. In such accelerators, dipole or bending magnets are used to keep particles on the *closed orbit*, defined as a particle trajectory that closes onto itself after a complete revolution. The *reference particle* is a particle which moves on the *reference closed orbit* through the center of all magnets.

It is convenient to define the coordinate system co-moving with the reference particle (Fig. 2.1), whose position at given time t is defined as $s = \int_0^t v_0 \mathrm{d}\tilde{t}$, where v_0 is the velocity of the reference particle. Then the coordinates of other particles can be expressed by a vector $(x, x', y, y', z, \Delta p/p_0)$, where x, y, z are coordinates of the particle, $x' = \mathrm{d}x/\mathrm{d}s$ and $y' = \mathrm{d}y/\mathrm{d}s$ are derivatives of x and y with respect to s, and $\Delta p = p - p_0$ is the momentum deviation. Without restoring transverse forces, particles with $x' \neq 0$ and $y' \neq 0$ will travel in transverse direction and will be lost when they reach an accelerator pipe wall. To avoid this, a series of quadrupole magnets is used for particle focusing.

Starting with the simplified case of $\Delta p/p_0 = 0$ and $z = 0$, transverse particle motion obeys Hill's equation,

$$x''(s) + k(s)x(s) = 0, \tag{2.3}$$

where $k(s)$ is the quadrupole focusing strength. Below, no coupling between transverse planes and the longitudinal plane is assumed, and for both transverse coordinates x, y

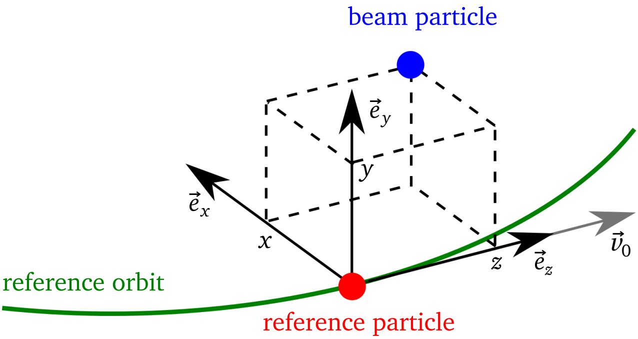

Figure 2.1.: The co-moving coordinate system with the reference particle.

one can use the same equations. In most cases x- and y-indices are omitted in this work for the sake of readability. For synchrotrons $k(s) = k(s + C)$ is periodic, where C is the length of the reference closed orbit or the accelerator circumference. The solution to Eq. 2.3 can be written as

$$\begin{aligned} x(s) &= \sqrt{\epsilon_{\text{sp}}\beta(s)}\cos\left(\Psi(s) + \psi_0\right), \\ x'(s) &= -\sqrt{\frac{\epsilon_{\text{sp}}}{\beta(s)}}\left[\alpha(s)\cos\left(\Psi(s) + \psi_0\right) + \sin\left(\Psi(s) + \psi_0\right)\right], \end{aligned} \tag{2.4}$$

and a particle performs *betatron oscillations*. Here, $\beta(s)$, $\alpha(s) = \beta'(s)$ and $\gamma(s) = (1 + \alpha^2(s))/\beta(s)$ are the *Twiss parameters* [41], ϵ_{sp} is the integration constant or the *single-particle emittance*, which is discussed below, and ψ_0 is the initial phase. The *beta function* $\beta(s)$ defines the particle oscillation amplitude $\sqrt{\epsilon_{\text{sp}}\beta(s)}$ and the *betatron phase*

$$\Psi(s) = \int_0^s \frac{\mathrm{d}\tilde{s}}{\beta(\tilde{s})}. \tag{2.5}$$

The number of betatron oscillations per one revolution is defined from Eq. 2.5 by

$$Q = \frac{1}{2\pi}\oint \frac{\mathrm{d}\tilde{s}}{\beta(\tilde{s})}, \tag{2.6}$$

and is called the *betatron tune*. This parameter is important for accelerator design and operation. The tune of a reference particle is called the *bare tune* Q_0. The *working point* is a choice of $Q_{0,x}, Q_{0,y}$, which defines beam quality and beam lifetime in synchrotrons.

In the presence of field errors, the particle motion can become unstable if tunes fulfill the resonance condition [42]

$$k\,Q_x + l\,Q_y = n, \tag{2.7}$$

where k, l, n are integer numbers, and $|k| + |l|$ is the order of the resonance. Depending on beam requirements and machine settings, the working point should be chosen to avoid resonances of a specific order, where higher order resonances are less destructive.

From Eq. 2.4 the evolution of particle coordinates can be expressed using transport matrices [41]. The particle coordinates at the position s_2 can be obtained from the coordinates at the position s_1 by $(x, x')^{\mathrm{T}}_{s_2} = \mathbf{M}(s_2, s_1)(x, x')^{\mathrm{T}}_{s_1}$ with a transfer matrix

$$\mathbf{M}(s_2, s_1) = \mathbf{B}(s_2)\begin{pmatrix} \cos\Delta\Psi & \sin\Delta\Psi \\ -\sin\Delta\Psi & \cos\Delta\Psi \end{pmatrix}\mathbf{B}^{-1}(s_1), \tag{2.8}$$

where $\Delta\Psi = \Psi(s_2) - \Psi(s_1)$ is the phase advance, and the matrices $\mathbf{B}$ and its inverse $\mathbf{B}^{-1}$ are defined by

$$\mathbf{B}(s) = \begin{pmatrix} \sqrt{\beta(s)} & 0 \\ -\frac{\alpha(s)}{\sqrt{\beta(s)}} & \frac{1}{\sqrt{\beta(s)}} \end{pmatrix} \text{ and } \mathbf{B}^{-1}(s) = \begin{pmatrix} \frac{1}{\sqrt{\beta(s)}} & 0 \\ \frac{\alpha(s)}{\sqrt{\beta(s)}} & \sqrt{\beta(s)} \end{pmatrix}. \tag{2.9}$$

This approach is widely used for analytical and simulation studies of the beam dynamics.

To explain the meaning of ϵ_{sp}, we combine $x(s)$ and $x'(s)$ in Eq. 2.4 as

$$\epsilon_{\mathrm{sp}} = \gamma(s)x^2(s) + 2\alpha(s)x(s)x'(s) + \beta(s)x'^2(s). \tag{2.10}$$

As we consider in this work the case without acceleration, ϵ_{sp} is an invariant of particle transverse motion and defines an ellipse in phase space (x, x') shown in Fig. 2.2. To quantify the beam quality, the *rms beam emittance* is used, which is the rms value of single-particle emittances. The rms beam emittance can be calculated using the rms beam size σ_x, the rms beam divergence $\sigma_{x'}$, and the correlation $\sigma_{xx'}$,

$$\epsilon = \sqrt{\sigma_x^2\sigma_{x'}^2 - \sigma_{xx'}^2}. \tag{2.11}$$

These quantities are given by central moments:

$$\sigma_x^2 = \langle x^2\rangle - \langle x\rangle^2, \tag{2.12}$$

$$\sigma_{x'}^2 = \langle x'^2\rangle - \langle x'\rangle^2, \tag{2.13}$$

$$\sigma_{xx'} = \langle xx'\rangle - \langle x\rangle\langle x'\rangle, \tag{2.14}$$

where $\langle\cdot\rangle$ denotes a mean value.

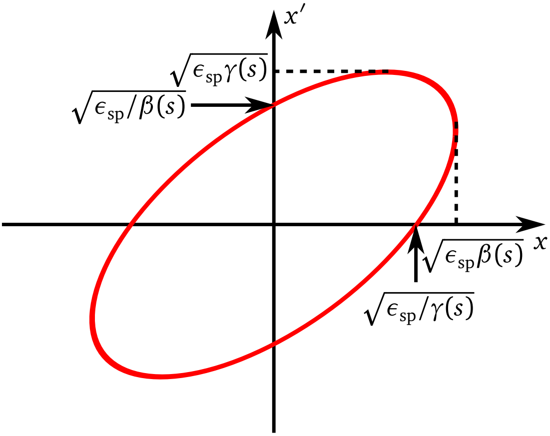

Figure 2.2.: Horizontal phase-space. An ellipse is given by Eq. 2.10 with the area of $\pi\epsilon_{\text{sp}}$.

If an accelerator is composed of linear elements such as dipole and quadrupole magnets, ϵ is constant according to the Liouville's theorem. However, for non-stationary beam distributions the rms beam emittance can grow which is discussed in Sec. 3.3.

Now we consider an *off-momentum particle* with $\Delta p/p_0 \neq 0$. This particle oscillates around a new closed orbit shifted from the reference orbit by the value $\Delta x(s) = D(s)\Delta p/p_0$, where $D(s)$ is the *dispersion function*. Then the total path length of the particle differs from C,

$$\frac{\Delta C}{C} = \frac{1}{C}\left[\oint \mathrm{d}s \frac{D(s)}{\rho}\right]\frac{\Delta p}{p_0} = \alpha_c \frac{\Delta p}{p_0}, \tag{2.15}$$

where α_c is the *momentum compaction factor*. The momentum deviation provides a velocity deviation

$$\frac{\Delta v}{v_0} = \frac{1}{\gamma^2}\frac{\Delta p}{p_0}, \tag{2.16}$$

which, together with the change in the path length, results in the shift of an angular revolution frequency defined using the *slip factor* η by

$$\frac{\Delta\omega}{\omega_0} = -\left(\frac{1}{\gamma_{\text{T}}^2} - \frac{1}{\gamma^2}\right)\frac{\Delta p}{p_0} = -\eta\frac{\Delta p}{p_0} = -\frac{\Delta T}{T_0}. \tag{2.17}$$

Here $\omega_0 = 2\pi/T_0$ and T_0 are the angular revolution frequency and the revolution period of the reference particle, correspondingly, $\gamma_{\text{T}} = \sqrt{1/\alpha_c}$ is the transition-γ, which corresponds to the beam energy where the revolution period is independent of the particle momentum. The shift of revolution frequency affects the longitudinal beam dynamics, which is discussed in the next section.

The momentum deviation affects betatron oscillations because the focusing force from quadrupole magnets is inversely proportional to a particle momentum [43]. It results in a change of the betatron tune described by the tune shift

$$\frac{\Delta Q_\xi}{Q_0} = \xi \frac{\Delta p}{p_0}, \tag{2.18}$$

where ξ is the *normalized chromaticity*. In the absence of higher-order magnets, the chromaticity mainly comes from the quadrupole magnets. This is usually called the *natural* or *linear chromaticity*. For large $\Delta p/p_0$, a particle that satisfies the resonance condition given by Eq. 2.7 will be lost. To avoid this, sextupole magnets can be used for chromaticity compensation.

The series of all magnets in the synchrotron is called the *lattice*. To simplify analysis and derivations in this work, we use the *constant-focusing lattice* for the description of the transverse beam dynamics. In this case, the periodic focusing strength and the beta function are the constant values

$$k(s) = \left(\frac{2\pi Q_0}{C}\right)^2, \text{ and } \beta(s) = \frac{C}{2\pi Q_0}, \tag{2.19}$$

respectively. Then the transfer matrix is simplified from Eq. 2.8 to

$$\mathbf{M}_{\mathrm{CF}}(s_2, s_1) = \begin{pmatrix} \cos\left[\frac{2\pi Q_0}{C}(s_2 - s_1)\right] & \frac{C}{2\pi Q}\sin\left[\frac{2\pi Q_0}{C}(s_2 - s_1)\right] \\ -\frac{2\pi Q}{C}\sin\left[\frac{2\pi Q_0}{C}(s_2 - s_1)\right] & \cos\left[\frac{2\pi Q_0}{C}(s_2 - s_1)\right] \end{pmatrix}, \tag{2.20}$$

and Eq. 2.3 is simplified to the equation of a harmonic oscillator,

$$x''(s) + \left(\frac{2\pi Q_0}{C}\right)^2 x(s) = 0. \tag{2.21}$$

2.2 Longitudinal dynamics

Two type of particle beams can be used in synchrotrons: *coasting* and *bunched* beams. In coasting beams, particles are uniformly distributed along the ring and circulate with the constant velocity in accordance with their momentum.

In bunches, particles occupy a particular region in the longitudinal phase space $(z, \Delta p/p_0)$ defined by the *rf bucket*. The reference particle is synchronized with rf phase and receives or loses the same energy per each passage through an rf cavity. An off-momentum particle performs *synchrotron oscillations* in the longitudinal plane. For a sinusoidal electric field, they can be described by synchrotron equations of motion [41]

$$\frac{\mathrm{d}\Delta p}{\mathrm{d}t} = \frac{\omega_0 q V}{2\pi\gamma m\beta^2 c^2}(\sin\phi - \sin\phi_0), \tag{2.22}$$

$$\frac{\mathrm{d}\phi}{\mathrm{d}t} = h\omega_0\eta\frac{\Delta p}{p_0}, \tag{2.23}$$

where h is the harmonic number of the rf system, V is the rf voltage, ϕ_0 is the phase of the reference particle with respect to the rf wave, and $\phi = \phi_0 + 2\pi hz/C$ is the phase of the off-momentum particle. Taking a derivative of Eq. 2.23 and substituting $\Delta p/p_0$ from Eq. 2.22, we can get the linearized equation for the phase ϕ

$$\frac{\mathrm{d}^2(\phi-\phi_0)}{\mathrm{d}t^2} = \frac{h\omega_0^2 q V\eta}{2\pi\gamma m\beta^2 c^2}(\sin\phi - \sin\phi_0) \approx \frac{h\omega_0^2 q V\eta\cos(\phi_0)}{2\pi\gamma m\beta^2 c^2}(\phi-\phi_0) = -\omega_s^2(\phi-\phi_0), \tag{2.24}$$

where the *angular synchrotron frequency* is

$$\omega_s = \omega_0\sqrt{\frac{hqV|\eta\cos\phi_0|}{2\pi\gamma m\beta^2 c^2}}. \tag{2.25}$$

Without acceleration, the phase stability condition $\eta\cos\phi_0 < 0$ requires $\phi_0 = 0$ for the beams those are below transition with $\gamma < \gamma_\mathrm{T}$ and $\eta < 0$. The number of synchrotron oscillations per revolution period is called the *synchrotron tune*

$$Q_s = \frac{\omega_s}{\omega_0}. \tag{2.26}$$

For larger ϕ, the equation of synchrotron motion is non-linear which results in a synchrotron tune spread of the beam. In this work, Eq. 2.24 is used for analytical derivation. The role of rf nonlinearities in simulations and measurements is discussed in Sec. 6.5.

2.3 Space charge force

So far we discussed single-particle dynamics, in which interactions between particles and beam interactions with its surroundings are not taken into account. In general, the full set of Maxwell's equations coupled with equations of motion should be solved for a self-consistent treatment of particle dynamics in intense beams. This work focuses on transverse dynamics of ion bunches, in which the characteristic length of variation of the charge density along the longitudinal direction is much larger than the transverse beam size. Thus, in the frame of the reference particle, the longitudinal component of the electric field can be neglected and the fields contained only in the 2D transverse plane can be considered [44]. Locally, the particle distribution in bunches is in good approximation stationary and fields can be computed by solving the Poisson equation.

To quantify the contribution of self-fields, we start with the case of coasting beams with a round cross-section in a perfectly conducting round beam pipe. Particles are uniformly distributed and the beam offset is zero. Following [45], a beam with the total number of particles N_p is approximated as a cylinder with the constant radius a and uniform density $\varrho = \lambda/(\pi a^2)$, where $\lambda = N_p/C$ is the linear density (Fig. 2.3). Due to radial symmetry the radial component of the electric field $E_{\mathrm{sc},r}$ can be obtained from Gauss's law (integration over volume and surface of a cylinder with radius $r < a$ and length l) in cylindrical coordinates (r, θ, z)

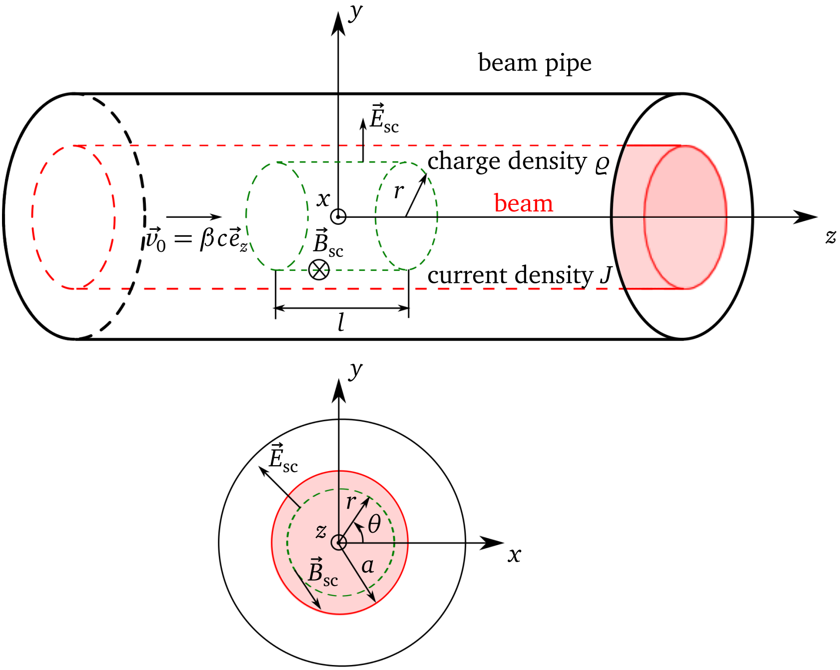

Figure 2.3.: A coasting beam approximated as a cylinder circulating with constant velocity $v_0 = \beta c$. The cylindrical volume used for calculation of electric and magnetic fields is denoted by green lines.

$$\int_0^{2\pi}\int_0^{l} E_{\mathrm{sc},r}\, r \,\mathrm{d}\theta \,\mathrm{d}z = \int_0^{r}\int_0^{2\pi}\int_0^{l} \varrho \,\mathrm{d}\tilde{r}\,\tilde{r}\,\mathrm{d}\theta\,\mathrm{d}z, \tag{2.27}$$

where ε_0 is the vacuum permittivity. The azimuthal component of the magnetic field $B_{\mathrm{sc},\theta}$ is given by Stock's law (integration over surface and a path the enclose the cylinder cross section)

$$\int_0^{2\pi} B_{\mathrm{sc},\theta} r \mathrm{d}\theta = \int_0^{2\pi} \int_0^{r} \mu_0 J \tilde{r} \mathrm{d}\theta \mathrm{d}\tilde{r} \tag{2.28}$$

where μ_0 is the vacuum permeability, $J = q\varrho\beta c$ is the current density. The resulting radial force for $r < a$ is given by Eq. 2.1

$$F_{\mathrm{sc},r} = q(E_{\mathrm{sc},r} - vB_{\mathrm{sc},\theta}) = \frac{\lambda q^2}{2\pi\varepsilon_0}(1-\beta^2)\frac{r}{a^2} = \frac{\lambda q^2}{2\pi\varepsilon_0\gamma^2}\frac{r}{a^2} = \frac{qE_{\mathrm{sc},r}}{\gamma^2} = \frac{qE_{\mathrm{sc},r}}{\gamma^2}, \tag{2.29}$$

which is linear in r. The factor of $1/\gamma^2$ comes from the cancellation of electric and magnetic parts. Replacing r in Eq. 2.29 by the transverse coordinate x results in the horizontal force $F_{\mathrm{sc},x}$. We can include this force in Eq. 2.21 by expressing x'' in terms of transverse acceleration $\ddot{x}$,

$$x'' = \frac{\mathrm{d}^2 x}{\mathrm{d}s^2} = \frac{1}{\beta^2 c^2}\frac{\mathrm{d}^2 x}{\mathrm{d}t^2} = \frac{\ddot{x}}{\beta^2 c^2} = \frac{1}{\beta^2 c^2}\frac{F_{\mathrm{sc},x}}{\gamma m} = \frac{2\lambda r_p}{\gamma^3\beta^2 a^2}x, \tag{2.30}$$

where $r_p = q^2/(4\pi\varepsilon_0 mc^2)$ is the classical particle radius. The simplified Hill's equation including the space charge force is

$$\begin{aligned} x''(s) + \left[\left(\frac{2\pi Q_0}{C}\right)^2 - \frac{2\lambda r_p}{\gamma^3\beta^2 a^2}\right]x(s) = \\ x''(s) + \left[\frac{2\pi(Q_0 - \Delta Q_{\mathrm{sc}})}{C}\right]^2 x(s) - \left[\frac{2\pi\Delta Q_{\mathrm{sc}}}{C}\right]^2 x(s) = 0 \end{aligned} \tag{2.31}$$

where the space charge tune shift parameter

$$\Delta Q_{\mathrm{sc}} = \frac{\lambda r_p C^2}{4\pi^2\gamma^3\beta^2 a^2 Q_0} = \frac{\lambda r_p C}{8\pi\gamma^3\beta^2\epsilon} > 0, \tag{2.32}$$

corresponds to the tune depression of particles $Q = Q_0 - \Delta Q_{\mathrm{sc}}$ in the coasting beam with the transverse Kapchinskij-Vladimirskij (KV) distribution [46]. We neglect the last term by assuming $\Delta Q_{\mathrm{sc}} \ll Q_0$.

In heavy ion synchrotrons, the transverse particle distribution is close to a Gaussian distribution. The strongest tune shift occurs for particles with small amplitudes in the beam center, and the tune shift decreases for larger amplitudes. This results in an amplitude dependent space charge tune shift which can be obtained analytically [47, 48]. The horizontal tune of the particle with emittances $\epsilon_{\mathrm{sp},x}, \epsilon_{\mathrm{sp},y}$ in a beam with a round cross section is given by [48]

$$Q(\epsilon_{\mathrm{sp},x}, \epsilon_{\mathrm{sp},y}) = Q_0 - 2\Delta Q_{\mathrm{sc}} \int_0^{1/4} \mathrm{d}u \frac{\left[I_0\left(\epsilon_{\mathrm{sp},x}u\right) - I_1\left(\epsilon_{\mathrm{sp},x}u\right)\right] I_0\left(\epsilon_{\mathrm{sp},y}u\right)}{\exp\left[(\epsilon_{\mathrm{sp},x} + \epsilon_{\mathrm{sp},y})u\right]}, \tag{2.33}$$

where I_k is the modified Bessel function of the order k. For a Gaussian transverse distribution the maximum space charge tune shift is twice larger than for the rms-equivalent KV beam. The tune distribution obtained from a statistical method [49] is shown in Fig. 2.4. Here 10^8 particles are populated according to a Gaussian distribution with long tails (the truncation at $5\sigma_x$) in both transverse directions creating a beam with a round cross section. To calculate the tune distribution function, the analytically calculated tunes of each particle is distributed in 100 bins of equal width in the range $[-2\Delta Q_{\mathrm{sc}}, 0]$. The distribution starts with zero at the maximum tune shift $-2\Delta Q_{\mathrm{sc}}$ because only few particles are at the beam center. We see no particles with the bare tune Q_0 and there is a gap from $\approx 0.25\Delta Q_{\mathrm{sc}}$ to 0.

In bunches the linear density is not constant. Typically, a transverse size of ion bunches is a few order of magnitude smaller than the bunch length. One can use an approximation that a bunch consists of many longitudinal slices which behave independently of each other. The space charge tune shift of each slice depends on the local line density. This results in a tune spread along the bunch. As the synchrotron oscillation period is much longer than the revolution period one can obtain an instan-

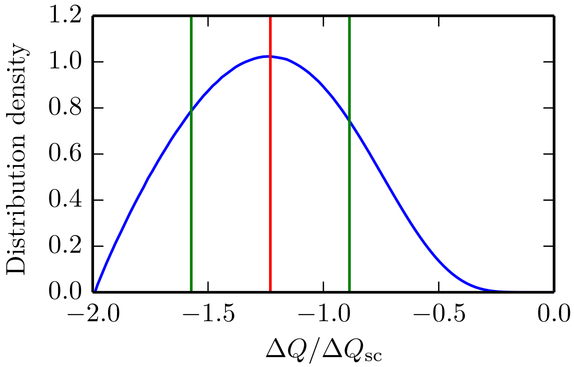

Figure 2.4.: Tune spread due to non-linear space charge in a coasting beam with a Gaussian transverse profile. The blue line is the distribution density, the red line denotes the average tune, the green lines are shifted from the average tune by the rms tune spread.

taneous tune distribution in bunches. For a Gaussian longitudinal distribution and a KV transverse distribution, the tune distribution is given by [31]

$$\frac{\mathrm{d}N}{\mathrm{d}Q} = \left[\Delta Q_{\mathrm{sc}} \sqrt{\pi \ln \left(\frac{\Delta Q_{\mathrm{sc}}}{\Delta Q} \right)} \right]^{-1}, \tag{2.34}$$

where in the definition of the space charge parameter (Eq. 2.32) we substitute λ by the peak linear density in a bunched beam λ_0. For a Gaussian transverse beam profile, the tune distribution can also be obtained by the statistical method [50] if we assume that the longitudinal motion of particles is frozen (Fig. 2.5). Only few particles have the strongest tune shift at the bunch center, similarly to the case of coasting beams. There is no gap near zero tune shifts because of a weak space charge in the bunch tails. In this work, these numerically obtained tune distributions (Figs. 2.4 and 2.5) are used to verify the self-consistent space charge solvers for particle tracking simulations (Sec. 5.3).

The space charge force is an internal force and it does not affect motion of the beam center. However, each particle oscillates with its own *incoherent tune* depressed by space charge. In free space a beam after a transverse kick will perform *coherent oscillation* with the *coherent* tune equal to Q_0. In the next section we discuss the effect that changes coherent beam dynamics.

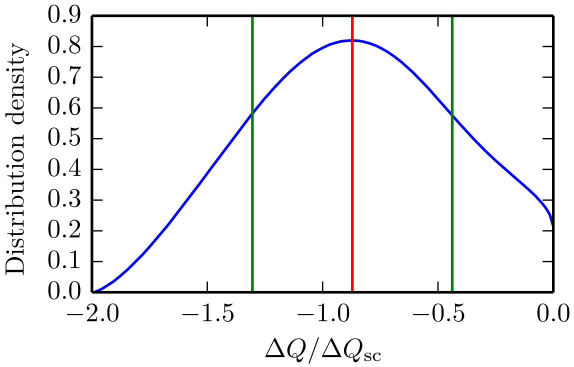

Figure 2.5.: Tune spread due to non-linear space charge in bunches with Gaussian longitudinal and transverse profile. The blue line is the distribution density, the red line denotes the average tune, the green lines are shifted from the average tune by the rms tune spread.

2.4 Image charges and impedances

The dynamics of a charged particle beam can be affected by its surroundings. For a smooth and perfectly conducting wall, this interaction can be evaluated in terms of *image charges*. We consider the case of a circular pipe with radius b and a round beam with radius a. Assuming $a \ll b$, a displaced beam is approximated as a line charge $q\lambda$ that induces surface charges. They can be represented as an image line charge $-q\lambda$ at the distance $b^2/\langle x\rangle$, where $\langle x\rangle$ is the average beam displacement (Fig. 2.6). At the same time, the beam current $I = \lambda q\beta c$ induces surface currents that can be represented as an image current $-I$ at the distance $b^2/\langle x\rangle$. The electric and magnetic fields due to image charge and current result in a horizontal force which in the beam center is given by [45]

$$F_{\mathrm{ic},x} = \frac{\lambda q^2(1-\beta^2)}{2\pi\varepsilon_0}\,\frac{\langle x\rangle}{b^2-\langle x\rangle^2} \approx \frac{\lambda q^2}{2\pi\varepsilon_0\gamma^2}\,\frac{\langle x\rangle}{b^2}. \tag{2.35}$$

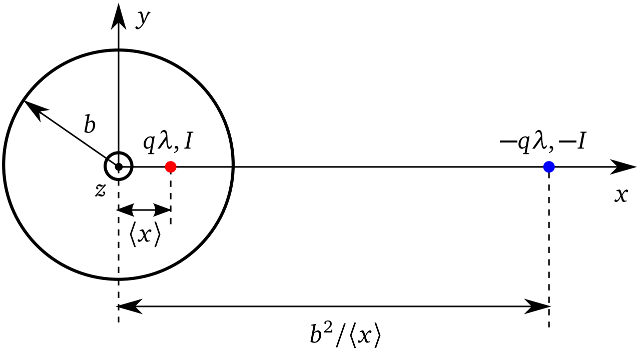

Figure 2.6.: Coherent oscillation of the beam (the red circle) inside a circular, perfectly conducting beam pipe, and its image charge and current (the blue circle).

To obtain an equation of beam motion, we average the simplified Hill's equation (Eq. 2.21) over the particle distribution and add this force using Eq. 2.30:

$$\begin{aligned} &\langle x''\rangle(s) + \left[\left(\frac{2\pi Q_0}{C}\right)^2 - \frac{2\lambda r_p}{\gamma^3\beta^2 b^2}\right]\langle x\rangle(s) = \\ &\langle x''\rangle(s) + \left[\frac{2\pi(Q_0-\Delta Q_{\mathrm{ic}})}{C}\right]^2\langle x\rangle(s) - \left[\frac{2\pi\Delta Q_{\mathrm{ic}}}{C}\right]^2\langle x\rangle(s) = 0, \end{aligned} \tag{2.36}$$

where the image charge tune shift parameter

$$\Delta Q_{\mathrm{ic}} = \frac{\lambda r_p C^2}{4\pi^2\gamma^3\beta^2 Q_0 b^2} = \Delta Q_{\mathrm{sc}} \frac{a^2}{b^2}, \tag{2.37}$$

corresponds the coherent tune shift $-\Delta Q_{\mathrm{ic}}$.

In bunches, image charges produce the coherent tune spread along the bunch. This effect is discussed in more detail in Sec. 4.3.

Generally, interaction of a beam and the accelerator components can be characterized using the *transverse dipole coupling impedance*

$$Z_\perp(\omega) = -\frac{i}{q\beta I\langle x\rangle} \oint \mathrm{d}s \vec{F}_\perp(\omega) = -\frac{i}{\beta I\langle x\rangle} \oint \mathrm{d}s \left(\vec{E}(\omega) + \vec{v} \times \vec{B}(\omega)\right)_\perp, \tag{2.38}$$

where $\vec{E}(\omega)$ and $\vec{B}(\omega)$ are the Fourier images of electric and magnetic fields. Due to transverse impedances a beam can become unstable, which is shortly discussed in the following section.

2.5 Beam transfer function and Landau Damping

We consider a beam that is excited by a driving force of the angular frequency ω. The *beam transfer function* (BTF) is defined as the ratio of the beam response to the excitation in the frequency domain [51]. Here, we discuss the BTF for the case when the single particle tune shift is dominated by the linear space charge and chromaticity. The analytical expression for normalized BTF R is given by [52, 53, 54, 55]

$$R(Q, \delta Q, \Delta Q_{\mathrm{sc}}) = \left[\frac{1}{R_0(Q + \Delta Q_{\mathrm{sc}}, \delta Q)} - \frac{\Delta Q_{\mathrm{sc}}}{\delta Q}\right]^{-1}, \tag{2.39}$$

where BTF is expressed as function of tune $Q = \omega/\omega_0$, and R_0 is the normalized BTF without space charge. For a Gaussian tune distribution centered at Q_0 with the rms tune spread δQ, R_0 is defined using the complex error function $w(z) = \exp(-z^2)\left[1 - \mathrm{erf}(-iz)\right]$ as

$$R_0(Q, \delta Q) = \delta Q \int_{-\infty}^{\infty} \frac{\mathrm{d}\tilde{Q}}{\tilde{Q} - Q} \exp\left[-\frac{(Q_0 - \tilde{Q})^2}{2\delta Q^2}\right] = \sqrt{\frac{\pi}{2}}\, w\left(\frac{Q_0 - Q}{\delta Q\sqrt{2}}\right), \tag{2.40}$$

where the contribution of the BTF around the tune $Q = -Q_0$ is neglected [56].

In a particle beam, the coherent oscillations can serve as a source of the driving force. Oscillations of a coasting beam can be represented by a superposition of coherent modes having spatial and time dependence [56],

$$x_n(s, t) \propto \exp\left(\frac{i2\pi n s}{C} - i\Omega t\right), \tag{2.41}$$

where Ω is the angular frequency of the mode, and n is the mode number. Depending on the phase velocity, there are two different types of dipole waves: *fast waves* and *slow waves*. A fast wave has a phase velocity higher then the particle's velocity, and a slow wave vice versa. The unperturbed angular frequencies of these waves are

$$\Omega_{\mathrm{fw}} = (n + Q_0)\omega_0, \text{ for fast waves,} \tag{2.42}$$

$$\Omega_{\mathrm{sw}} = (n - Q_0)\omega_0, \text{ for slow waves.} \tag{2.43}$$

The transverse impedances can change the coherent mode frequency producing the complex frequency shift. To examine the stability of a particular mode, we use the *dispersion relation* [47]. For the slow wave, it is given by

$$\frac{1}{R(Q, \delta Q_{\mathrm{sw}}, \Delta Q_{\mathrm{sc}})} = -\frac{\Delta Q_{\mathrm{coh}}}{\delta Q_{\mathrm{sw}}}, \tag{2.44}$$

where the coherent tune shift of the mode for the beam with a zero momentum spread is

$$\Delta Q_{\mathrm{coh}} = i\frac{\lambda q^2 Z_\perp(\Omega_{\mathrm{sw}})}{4\pi m\gamma Q_0}, \tag{2.45}$$

Here, the tune distribution used in R_0 is centered at $Q = \Omega_s/\omega_0$ instead of Q_0 and has the tune spread

$$\delta Q_{\mathrm{sw}} = |\xi Q_0 + \eta(n - Q_0)|\,\frac{\delta p}{p_0}. \tag{2.46}$$

where δp is the momentum spread. To obtain boundary of stability, we first plot $1/R(Q, \delta Q, \Delta Q_{\mathrm{sc}})$ the *stability diagram* [51], where Q is scanned from $-\infty$ to ∞ (Fig. 2.7). Then we plot the r.h.s. of Eq. 2.44 where the impedance is taken at frequency Ω_{sw}. If this point lies on the side that contains the origin, the mode is stable due to Landau damping [41, 51, 56]. Otherwise the mode is unstable. Landau damping can be lost due to space charge that shifts the stability along the real part of ΔQ (the bottom plot in Fig. 2.7).

The dispersion relation for fast waves can be obtained by changing the sign of the r.h.s. of Eq. 2.44. The imaginary part of the coherent frequency shift due to impedances is negative for fast waves because $\mathrm{Re}[Z_\perp(\omega)] > 0$ for $\omega > 0$ [51]. Thus, fast waves are always stable.

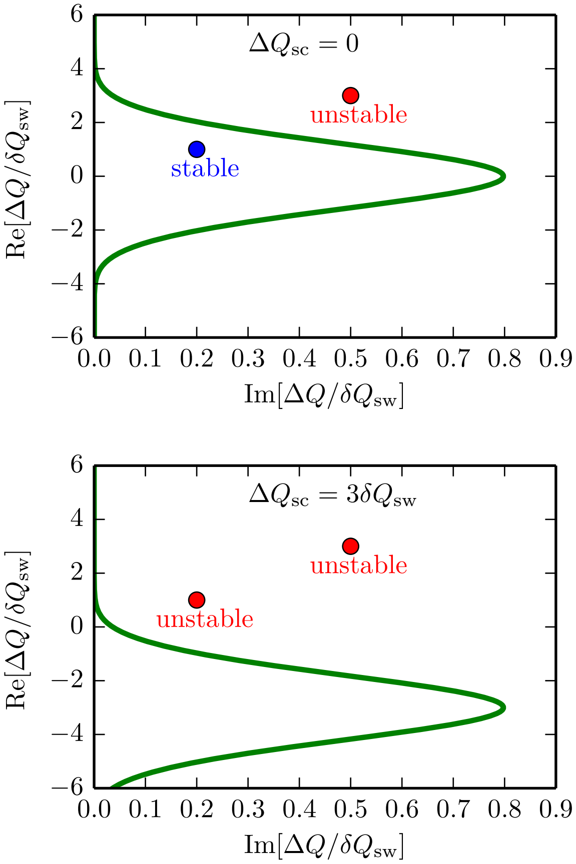

Figure 2.7.: Stability diagram $1/R(Q, \delta Q_{\mathrm{sw}}, \Delta Q_{\mathrm{sc}})$ with (the bottom plot) and without (the top plot) space charge in the complex plane with $\Delta Q = Q - \Omega_{\mathrm{sw}}/\omega_0$ for a Gaussian frequency distribution centered at frequency $Q = \Omega_s/\omega_0$ and with the tune spread δQ_{sw}. Points are from the r.h.s of the dispersion relation given by Eq. 2.44.

3 Transverse decoherence without intensity effects

After a transverse offset, the amplitude of beam centroid oscillations decays due to the spread of individual particle frequencies. This process is usually called *decoherence* or *phase-mixing*. It can be used for diagnostic purposes (e.g. for chromaticity measurements [57]), but it can also reduce machine performance. For example, after the bunch-to-bucket transfer in synchrotrons, decoherence can produce an emittance blowup. There are different sources of the particle tune spread in a beam: chromaticity, transverse nonlinearities, rf nonlinearities, space charge, and impedances. In this chapter, we discuss decoherence without intensity effects where the process is governed by linear chromaticity. We start with the case of decoherence for coasting beams in Sec. 3.1. For a bunched beam, we include the linear synchrotron motion for calculation of the bunch offset (Sec. 3.2) and the transverse emittance (Sec. 3.3). Then we describe observations of decoherence signals for bunches after the transverse kick in Sec. 3.4. Finally, we show the relation between decoherence of bunched and coasting beams in Sec. 3.5.

3.1 Decoherence of 2D beams and pulse response function

In case of coasting beams with uncoupled transverse planes, the decoherence process can described as a 1D problem. We consider a beam that has initial offset A_0. Without momentum spread, the beam will perform harmonic oscillations with a constant amplitude. The momentum spread and chromaticity produce the tune spread. The betatron phases of individual particles will diverge resulting in reduction of the beam amplitude.

The turn-by-turn particle betatron phase is

$$\psi(N,\Delta p) = 2\pi Q_0 N + 2\pi Q_0 N \xi \frac{\Delta p}{p_0}, \tag{3.1}$$

where N is the turn number. The amplitude of single particle oscillations remains constant in the constant-focusing lattice and the particle phase determines the particle coordinates according to Eq. 2.4 and Eq. 2.19:

$$x(N,\Delta p) = \mathrm{Re}\left[\sqrt{\frac{\epsilon_{\mathrm{sp}} C}{2\pi Q}} \exp\left(i\psi(N,\Delta p) + i\psi_0\right)\right]. \tag{3.2}$$

Assuming a beam with an arbitrary transverse profile and a Gaussian longitudinal distribution, the beam offset evolution after the initial displacement is defined by

$$\begin{aligned}\langle x\rangle(N) &= A_0 \mathrm{Re}\left[\int_{-\infty}^{+\infty} \mathrm{d}\Delta p \, \frac{1}{\sqrt{2\pi}\delta p} \exp\left(-\frac{\Delta p_i^2}{2\delta p^2}\right) \exp(i\psi(N,\Delta p))\right] \\ &= A_0 \exp\left\{-2(\pi\delta Q_\xi N)^2\right\} \cos(2\pi Q_0 N) = A_0 G_0(N),\end{aligned} \tag{3.3}$$

where σ_z is the rms bunch length, $\delta Q_\xi = |\xi| Q_0 \delta p/p_0$ is the tune spread due to chromaticity and momentum spread, and $G_0(N)$ is the *pulse response function* of a coasting beam with a Gaussian tune distribution [56, 58]. We define the characteristic decoherence time by

$$N_{\mathrm{dec0}} = (\sqrt{2}\pi\delta Q_\xi)^{-1}, \tag{3.4}$$

which corresponds to the $1/e$-decrease of the oscillation amplitude. The decoherence processes is faster for the larger parameter δQ_ξ.

For low-intensity beams, the pulse response function can be calculated from the BTF using the inverse Fourier transform,

$$G_0(N, \delta Q_\xi) = \frac{1}{4\pi\delta Q_\xi} \mathrm{Re}\left[\int_{-\infty}^{+\infty} \mathrm{d}Q \, R_0(Q, \delta Q_\xi) e^{i2\pi Q N}\right]. \tag{3.5}$$

The symbol Re appears here because we neglected the contribution due to tunes around $-Q_0$ [56].

3.2 Decoherence of bunched beams

In bunched beams, a particle with the initial momentum Δp_i and the initial longitudinal position z_i has a betatron tune that changes turn-by-turn by

$$Q(N) = Q_0 + \xi Q_0 \frac{\Delta p(N)}{p_0} = Q_0 + \xi Q_0 \left[\frac{\Delta p_i}{p_0} \cos(2\pi Q_s N) + z_i \frac{2\pi Q_s}{\eta C} \sin(2\pi Q_s N)\right], \tag{3.6}$$

where linear synchrotron oscillations are considered (see Sec. 2.2). The betatron phase as a function of N is given by integration of Eq. 3.6 multiplied by 2π:

$$\begin{aligned}\psi(N, z_i, \Delta p_i) &= 2\pi Q_0 \int_0^N \mathrm{d}\tilde{N} \left\{1 + \xi \left[\frac{\Delta p_i}{p_0} \cos(2\pi Q_s \tilde{N}) + z_i \frac{2\pi Q_s}{\eta C} \sin(2\pi Q_s \tilde{N})\right]\right\} \\ &= 2\pi Q_0 N + \frac{Q_0 \xi}{Q_s} \left[\frac{\Delta p_i}{p_0} \sin(2\pi Q_s N) + z_i \frac{2\pi Q_s}{\eta C} (1 - \cos(2\pi Q_s N))\right].\end{aligned} \tag{3.7}$$

Using the evolution of the particle coordinate,

$$x(N,z_i,\Delta p_i) = \mathrm{Re}\left[\sqrt{\frac{\epsilon_{\mathrm{sp}} C}{2\pi Q}}\exp(i\psi(N,z_i,\Delta p_i) + i\psi_0)\right], \tag{3.8}$$

we calculate the bunch offset, similarly to Eq. 3.3,

$$\begin{aligned}\langle x\rangle(N) &= A_0 \mathrm{Re}\left[\int_{-\infty}^{+\infty} \mathrm{d}z_i \int_{-\infty}^{+\infty} \mathrm{d}\Delta p_i \, \frac{1}{2\pi\sigma_z \delta p} \exp\left[-\frac{z_i^2}{2\sigma_z^2} - \frac{\Delta p_i^2}{2\delta p^2}\right] \exp(i\psi(N,z_i,\Delta p_i))\right] \\ &= A_0 \mathrm{F}_\xi(N)\cos(2\pi Q_0 N).\end{aligned} \tag{3.9}$$

Here the chromaticity parameter is

$$q_\xi = \frac{|\xi| Q_0}{Q_s}\frac{\delta p}{p_0}, \tag{3.10}$$

and the envelope of beam oscillations is

$$\mathrm{F}_\xi(N) = \exp\left\{-2q_\xi^2 \sin^2(\pi Q_s N)\right\}. \tag{3.11}$$

The bunch offset returns to the initial value after the synchrotron period $N_s = 1/Q_s$, which is called *recoherence*. For a fixed value of the synchrotron tune, both processes are fully defined by the chromaticity parameter. A larger q_ξ leads to a faster decay and a stronger modulation of the beam oscillation amplitude (Fig. 3.1). For $q_\xi > 1/\sqrt{2}$, the characteristic decoherence time is defined from Eq. 3.11 by

$$N_{\mathrm{dec}} = \frac{N_s}{\pi}\arcsin\left(\frac{1}{\sqrt{2}q_\xi}\right), \tag{3.12}$$

which corresponds to the $1/e$-decrease of the oscillation amplitude. From Eq. 3.12, $N_{\mathrm{dec}} \le N_s/2$, and it is decreases for larger q_ξ.

To obtain evolution of the local beam offset $\langle x\rangle(N,z)$, we integrate Eq. 3.8 only over the transverse distribution and particle momenta,

$$\langle x\rangle(N,z) = A_0 \exp\left[-\frac{q_\xi^2 \sin^2(2\pi Q_s N)}{2}\right]\cos\left(2\pi Q_0 N + 2\,\mathrm{sgn}(\xi)\, q_\xi \sin^2(\pi Q_s N)\frac{z}{\sigma_z}\right), \tag{3.13}$$

where sgn(x) is the sign function. Chromaticity and momentum spread produce intra-bunch oscillations which evolve in time (Fig. 3.2). The amplitude of these oscillations is modulated with the synchrotron frequency and can be suppressed significantly for large q_ξ (Fig. 3.3).

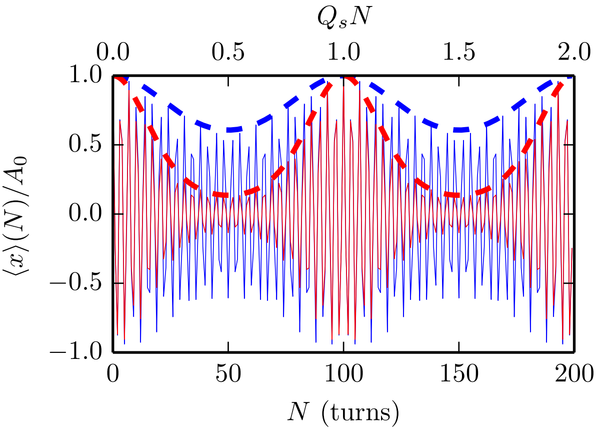

Figure 3.1.: Time evolution of the beam offset after the initial displacement for different chromatic tune spread and $Q_s = 0.01$. Red lines are for $q_\xi = 1.0$, blue lines are for $q_\xi = 0.5$. The solid lines are the bunch offsets (Eq. 3.9) and the dashed lines are given by Eq. 3.11.

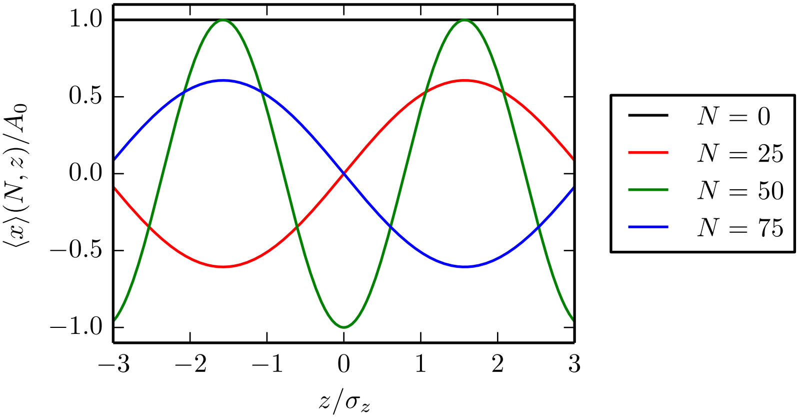

Figure 3.2.: Decoherence due to momentum spread and chromaticity results in intrabunch oscillations of the local offset (Eq. 3.13). Beam parameters: $Q_0 = 4.29$, $q_\xi = 1.0$, $Q_s = 0.01$.

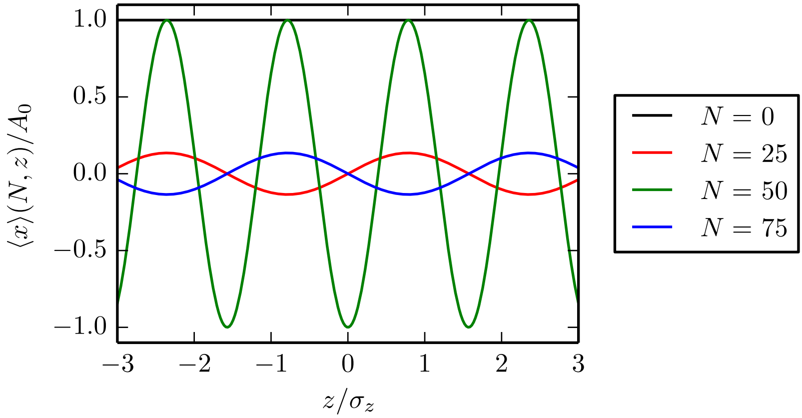

Figure 3.3.: Larger chromaticity reduces the amplitude of intrabunch oscillations. Beam parameters: $Q_0 = 4.29$, $q_\xi = 2.0$, $Q_s = 0.01$.

3.3 Emittance growth due to decoherence

Phase-mixing causes a change of the particle distribution in the transverse phase-space. The combination of magnet field nonlinearities, non-linear rf fields, and intensity effects causes an irreversible emittance blowup. Here, we discuss the emittance blowup in bunches for the case of chromaticity, linear synchrotron motion, and Gaussian momentum distribution.

The time evolution of beam size, divergence, and correlation is given by:

$$\sigma_x^2(N) = \frac{\epsilon C}{2\pi Q_0}\left[1 + \frac{K^2}{2}\left(1 + \mathrm{F}_\xi^4(N)\cos(4\pi Q_0 N)\right) - K^2\mathrm{F}_\xi^2(N)\cos^2(2\pi Q_0 N)\right], \tag{3.14}$$

$$\sigma_{x'}^2(N) = \frac{\epsilon 2\pi Q_0}{C}\left[1 + \frac{K^2}{2}\left(1 - \mathrm{F}_\xi^4(N)\cos(4\pi Q_0 N)\right) - K^2\mathrm{F}_\xi^2(N)\sin^2(2\pi Q_0 N)\right], \tag{3.15}$$

$$\sigma_{xx'}(N) = \epsilon\frac{K^2}{2}\mathrm{F}_\xi^2(N)\sin(4\pi Q_0 N)\left[1 - \mathrm{F}_\xi^2(N)\right], \tag{3.16}$$

where $K = A_0/\sigma_0$ is the initial offset normalized by the initial rms beam size $\sigma_0 = \sqrt{\epsilon_0 C/(2\pi Q_0)}$, and ϵ_0 is the initial rms beam emittance. The substitution of Eqs. 3.14, 3.15, 3.16 into Eq. 2.11 gives the time evolution of the rms emittance,

$$\epsilon^2(N) = \epsilon_0^2\left[1 + \frac{K^2}{2}\left(1 - \mathrm{F}_\xi^2(N)\right)\right]^2 - \epsilon_0^2\frac{K^4}{4}\mathrm{F}_\xi^4(N)\left(1 - \mathrm{F}_\xi^2(N)\right)^2. \tag{3.17}$$

Neglecting the second term, we get the *matched equivalent emittance* [59]

$$\epsilon_{\mathrm{equiv}}(N) = \frac{\pi Q_0}{C}\left[\sigma_x^2(N) + \frac{C}{2\pi Q_0}\sigma_{x'}^2(N)\right] = \epsilon_0\left[1 + \frac{K^2}{2}\left(1 - \mathrm{F}_\xi^2(N)\right)\right], \tag{3.18}$$

which is simply related to the beam oscillation envelope. The maximum difference between $\epsilon(N)$ and $\epsilon_{\mathrm{equiv}}(N)$ is about 0.5% for $K < 1$.

During the decoherence process the transverse emittance blows up and then returns to the initial value after the synchrotron period because of compensation of the betatron phase spread (Fig. 3.4). A larger parameter q_ξ provides a stronger emittance blowup. For $q_\xi \gg 1$ the maximum emittance growth approaches

$$\Delta\epsilon_{\max} = \frac{\epsilon_0 K^2}{2} = \frac{\epsilon_0 A_0^2}{2\sigma_0^2}, \tag{3.19}$$

and it does not depend on the transverse distribution (see, e.g., in Ref. [42]). The emittance blowup is always reversible for the considered case.

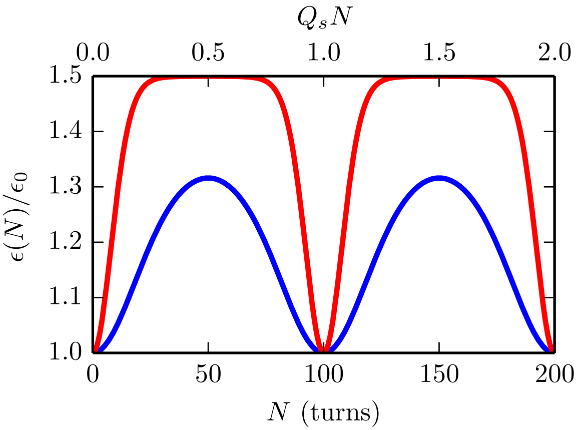

Figure 3.4.: Time evolution of the rms transverse emittance of the bunch after the initial offset for different chromatic tune spread and $Q_s = 0.01$ from Eq. 3.17. The red line is for $q_\xi = 1.0$, the blue line is for $q_\xi = 0.5$.

3.4 Observation of decoherence

The analytical calculation of the bunch offset evolution in Refs. [60, 61] assumes that at a certain time all particles experience the same transverse kick independent from the longitudinal position. For each time step the transverse bunch offset is calculated as the average of all particle coordinates. This is called a fixed-time monitoring of the beam dynamics [62]. A turn-by-turn signal of the bunch offset after the kick is calculated when the reference particle passes by a Beam Position Monitor (BPM).

In low-energy ion synchrotrons, bunches are longer than the diagnostics or injection kickers. Applying the constant kick in time, the initial betatron phase of a particle depends on its longitudinal position. In this case, the evolution of the bunch offset is calculated as the average of the detected local offset over the passage time through the BPM. This is called a fixed-position monitoring [62]. However, the BPM signals are given by particles which pass by the BPM with different time delays due to different momenta. The observed decoherence in this case is different from the fixed-time monitoring and Eq. 3.9 is not valid.

To describe decoherence observed at the fixed position, we expand the betatron phase given by Eq. 3.7 in assumption of a small time delay ΔN,

$$\begin{aligned}
\psi(N, z_i, \Delta p_i) &\approx \psi(N_0, z_i, \Delta p_i) + \frac{\mathrm{d}\psi}{\mathrm{d}N}\Delta N \\
&= \psi(N_0, z_i, \Delta p_i) + 2\pi\left[Q_0 + \xi Q_0 \frac{\Delta p(N_0)}{p_0}\right]\eta \int_0^{N_0} \mathrm{d}\tilde{N}\, \frac{\Delta p(\tilde{N})}{p_0} \\
&\approx \psi(N_0, z_i, \Delta p_i) + 2\pi Q_0 \eta \int_0^{N_0} \mathrm{d}\tilde{N}\, \frac{\Delta p(\tilde{N})}{p_0} \\
&= 2\pi Q_0 N_0 + \frac{Q_0(\xi+\eta)}{Q_s}\left[\frac{\Delta p_i}{p_0}\sin(2\pi Q_s N_0) + z_i \frac{2\pi Q_s}{\eta C}(1-\cos(2\pi Q_s N_0))\right]
\end{aligned} \tag{3.20}$$

where N_0 is the time when the reference particle pass by the BPM, and the second order terms of $\Delta p/p_0$ are neglected. This equation can be obtained from Eq. 3.7 by a substitution $\xi \to \xi + \eta$. Both ways of monitoring are equivalent if we substitute the parameter q_ξ in Eq. 3.11 by the effective parameter

$$q_{\text{eff}} = \frac{|\eta + \xi| Q_0}{Q_s} \frac{\delta p}{p_0} , \tag{3.21}$$

for the fixed-position monitoring. Below we present simulations with the fixed-time monitoring while using the notation of effective parameter q_{eff} given by Eq. 3.21 for direct comparisons with the measurements.

3.5 Early decoherence

As discussed above, the initial decoherence is important for the emittance blowup and is faster than the synchrotron period ($N_{\text{dec}} \le N_s/2$). A long ion bunch can be considered locally as a coasting beam with the corresponding line density $\lambda(z)$. Thus, for a time interval shorter than the synchrotron period, the bunch is a superposition of 2D slices of coasting beams. Without intensity effects, it means that we can expect similar behavior from a coasting beam and a bunched beam during the initial stage of decoherence. We show this by expanding $\sin(\pi Q_s N)$ in the time evolution of the beam offset (Eq. 3.9) with the substitution $q_\xi \to q_{\text{eff}}$ for $N \ll N_s$,

$$\langle x\rangle(N) \approx A_0 \exp\{-2(\pi\delta Q_{\text{eff}}N)\}\cos(2\pi Q_0 N), \tag{3.22}$$

where the effective tune spread is

$$\delta Q_{\text{eff}} = |\eta+\xi| Q_0 \frac{\delta p}{p_0} . \tag{3.23}$$

Thus, we can also define the pulse response function for the bunch beam for $N \ll N_s$ as a superposition of pulse response functions of 2D slices (Eq. 3.3),

$$G_{\text{b}}(N,\delta Q_{\text{eff}}) = \frac{\int_{z_{\min}}^{z_{\max}} G_0(N,\delta Q_{\text{eff}})\lambda(z)\text{d}z}{\int_{z_{\min}}^{z_{\max}} \lambda(z)\text{d}z}. \tag{3.24}$$

For large effective spread, a modification of the initial decoherence by the synchrotron motion is negligible (Fig. 3.5).

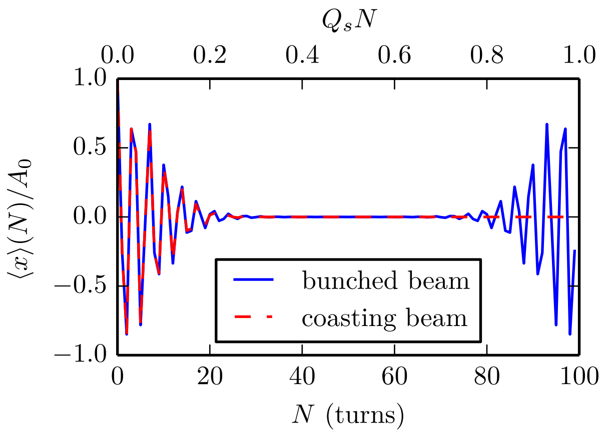

Figure 3.5.: Comparison of decoherence of a bunch and a coasting beam for $\delta Q_{\text{eff}} = 0.02$ and $Q_s = 0.01$.

4 Decoherence of intense beams

In previous chapter, we discussed the decoherence process and the emittance blowup following the initial offset when the tune spread is dominated by contribution of chromaticity and the slip factor. The additional incoherent tune shift and the tune spread in the presence of intensity effects impact the single particle dynamics as well as coherent beam dynamics. Here, we discuss the role of moderate and strong space charge in the decoherence process as it is foreseen in the SIS100 synchrotron. For higher beam intensities we also consider the contribution of image charges that can be significant for the thick beams required for the FAIR project.

4.1 2D case "coasting beam"

To understand decoherence in intense ion beams, we start with a case of coasting beams. As we discussed in Sec. 3.5, decoherence of low-intensity beams due to chromaticity is given by the pulse response function (see Eq. 3.3). As the pulse response function is related to the BTF according to Eq. 3.5, we attempt to obtain a similar relation in the presence of space charge.

We consider a KV transverse distribution that results in a linear space charge force. It make sense to revisit the equation of the modified BTF

$$R(Q,\delta Q_{\mathrm{eff}},\Delta Q_{\mathrm{sc}}) = \left[\frac{1}{R_0(Q+\Delta Q_{\mathrm{sc}},\delta Q_{\mathrm{eff}})} - \frac{\Delta Q_{\mathrm{sc}}}{\delta Q_{\mathrm{eff}}}\right]^{-1}. \tag{2.39 revisited}$$

It agrees with simulations for beams with Gaussian transverse distribution and measurements for the space charge strength $\Delta Q_{\mathrm{sc}} \leq 2\delta Q_{\mathrm{eff}}$ [63, 64]. As the pulse response function vanishes for $N < 0$, the real and the imaginary part of the BTF are related by the Hilbert transform (see [58]),

$$\mathrm{Im}[R(Q,\delta Q_{\mathrm{eff}},\Delta Q_{\mathrm{sc}})] = \mathscr{H}[\mathrm{Re}[R(Q,\delta Q_{\mathrm{eff}},\Delta Q_{\mathrm{sc}})]] = \frac{1}{\pi}\mathrm{p.v.}\int_{-\infty}^{+\infty} \mathrm{d}\tilde{Q}\,\frac{R(\tilde{Q},\delta Q_{\mathrm{eff}},\Delta Q_{\mathrm{sc}})}{Q-\tilde{Q}}, \tag{4.1}$$

which is defined using the Cauchy principal value (denoted here by p.v.). Using this property and the inverse Fourier transform, we get the pulse response function with space charge

$$\begin{aligned} G(N,\delta Q_{\mathrm{eff}},\Delta Q_{\mathrm{sc}}) &= \frac{1}{4\pi\delta Q_{\mathrm{eff}}}\mathrm{Re}\left[\int_{-\infty}^{+\infty} \mathrm{d}Q\, R(Q,\delta Q_{\mathrm{eff}},\Delta Q_{\mathrm{sc}})e^{i2\pi QN}\right] \\ &= \frac{1}{\pi\delta Q_{\mathrm{eff}}}\int\limits_{0}^{\infty} \mathrm{d}Q\, \cos(2\pi QN)\,\mathrm{Re}\left[R(Q,\delta Q_{\mathrm{eff}},\Delta Q_{\mathrm{sc}})\right]. \end{aligned} \tag{4.2}$$

It gives a closed form for the time evolution of the average beam offset. Performing numerical integration, we find that space charge results in a slower decoherence (Fig. 4.1).

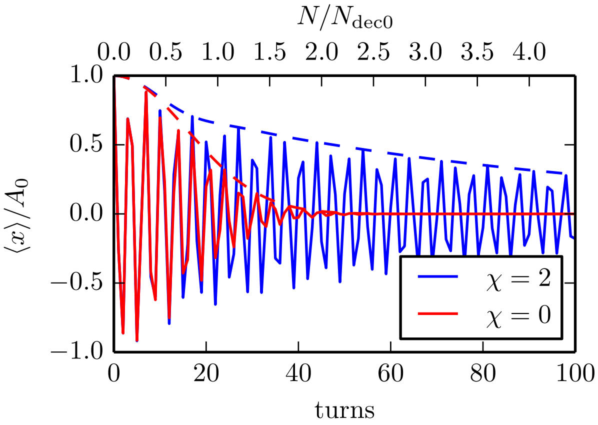

Figure 4.1.: Transverse decoherence of the kicked coasting beams with and without space charge from the model (Eq. 4.2). The solid lines are the turn-by-turn evolution of the beam offset and the dashed lines are the oscillation amplitudes A_{beam} (Eq. 4.3). Without space charge the $1/e$-decrease of the offset amplitude corresponds to $N = N_{\mathrm{dec0}} \approx 22.5$ turns given by Eq. 3.4 for $\delta Q_{\mathrm{eff}} = 0.01$.

To simplify comparison of decoherence with different space charge strength, we extract the beam oscillation amplitude calculating the analytic signal

$$A_{\mathrm{beam}} = A_0|G + i\mathscr{H}[G]|. \tag{4.3}$$

We define a 2D space charge parameter as the ratio of the characteristic tune shift (Eq. 2.32) to the effective spread (Eq. 3.23),

$$\chi = \frac{\Delta Q_{\mathrm{sc}}}{\delta Q_{\mathrm{eff}}}. \tag{4.4}$$

To demonstrate the systematic behavior of decoherence with space charge, we perform numerical integration Eq. 4.2 varying the space charge strength with finite steps. We obtain 2D array with values of the offset amplitude (Eq. 4.3) that correspond to different χ and the turn number N. Then, the values in the array are interpolated for obtaining the intermediate points (Fig. 4.2).

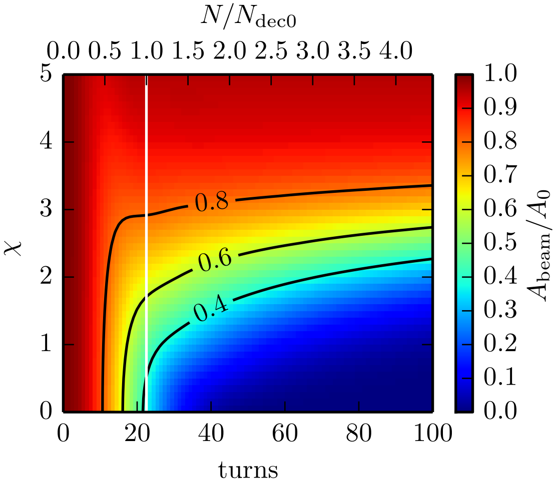

Figure 4.2.: Time evolution of the beam oscillation amplitude for 2D beams with different space charge, $\delta Q_{\mathrm{eff}} = 0.01$, $A_0 = 0.1\sigma_0$. Colors and the solid lines (contour lines) are given by Eq. 4.2. The vertical white line is $N_{\mathrm{dec0}} = 22.5$ turns (Eq. 3.4).

For $\chi > 3$ we observe the *loss of decoherence*: after a small reduction the amplitude of oscillations remains constant. To explain this effect, we use the stability diagram ($1/R$) shown in Fig. 4.3. Without impedances the coherent tune shift is zero $\Delta Q = 0$ (the green point). The stability diagram is shifted by space charge (the red line) along the real part of ΔQ (see Eq. 2.39). When the stability diagram is moved away from the coherent tune, Landau damping is lost. From our model we see that it is similar for the loss of decoherence. It can be also interpreted by the deformation of the real part of the BTF due to space charge (Eq. 2.39). For a larger space charge parameter,

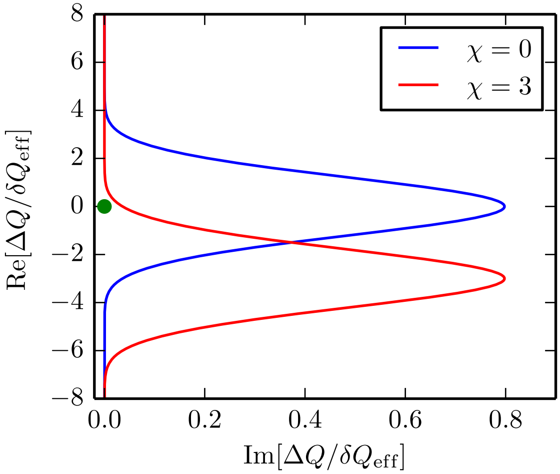

Figure 4.3.: Stability diagram with and without space charge from Eq. 2.39. The green point is the coherent tune without impedances.

Re[R] becomes a peaked function with a small width (Fig. 4.4). Integration in Eq. 4.2 with this function yields a slowly decaying pulse response function. On the one hand,

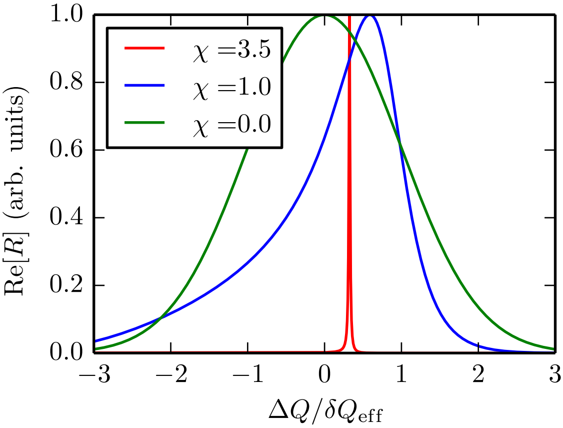

Figure 4.4.: Deformation of the beam transfer function due to space charge given by Eq. 2.39.

the numerical calculation of the green function is difficult for $\chi > 5$. In this case, the sharp peak of $\text{Re}[R]$ has to be evaluated for a set of tunes with high resolution. On the other hand, we know that for the case of $\delta Q_{\text{eff}} = 0$ which equivalent to $\chi \to \infty$ there is no decoherence. It is due to the fact the internal space charge forces do no affect the collective beam oscillations. Thus, for larger parameter χ, there is a stronger suppression of decoherence and the oscillation amplitude remains constant.

4.2 Bunched beams

In this section we present an extension of the analytical model (Eq. 4.2) to bunched ion beams. We focus on the initial stage of decoherence when the synchrotron motion can be neglected. Thus, as we discussed in Sec. 3.5, a bunch can be considered as a superposition of independent transverse 2D slices. To calculate the total bunch offset with space charge, we sum the offsets of the individual slices given by Eq. 4.2, similarly to Eq. 3.24

$$G_{\text{b,sc}}(N, q_{\text{eff}}, q_{\text{sc}}) = \frac{\int_{z_{\min}}^{z_{\max}} G(N, Q_s q_{\text{eff}}, Q_s q_{\text{sc}} \lambda(z)/\lambda_0)\lambda(z)\text{d}z}{\int_{z_{\min}}^{z_{\max}} \lambda(z)\text{d}z}, \tag{4.5}$$

Here, we define the space charge parameter as the ratio of the space charge tune shift in the center of the rms-equivalent bunch with a transverse KV distribution (Eq. 2.32) to the synchrotron tune (Eq. 2.26),

$$q_{\text{sc}} = \frac{\Delta Q_{\text{sc}}}{Q_s}. \tag{4.6}$$

Below we consider bunches with a Gaussian longitudinal profile.

Performing the numerical integration of Eq. 4.5 for different q_{sc}, we observe a slower decoherence for stronger space charge (Fig. 4.5), but for $q_{\text{sc}} > 3q_{\text{eff}}$ decoherence is still present. It is different from the case of coasting beams, where we observe loss of decoherence for $\chi > 3$ (see Fig. 4.2). For $q_{\text{sc}} = 3q_{\text{eff}}$, decoherence is lost only in the central slice where the amplitude of the local bunch offset is constant. In other slices with a weaker space charge, decoherence is present and reduces the local offset. Thus, the total bunch decreases as addition of the local offsets. For $q_{\text{sc}} = 15q_{\text{eff}}$ in accordance with the criteria for the local space charge strength, decoherence is lost for 93% of the bunch. Unfortunately, this can not be demonstrated because we face the same problem of the numerical integration which we discussed in Sec. 4.1.

4.3 Influence of image charges

In the previous section, we discussed the decoherence process governed by the interplay of chromaticity and space charge. The initial stage of decoherence in bunched

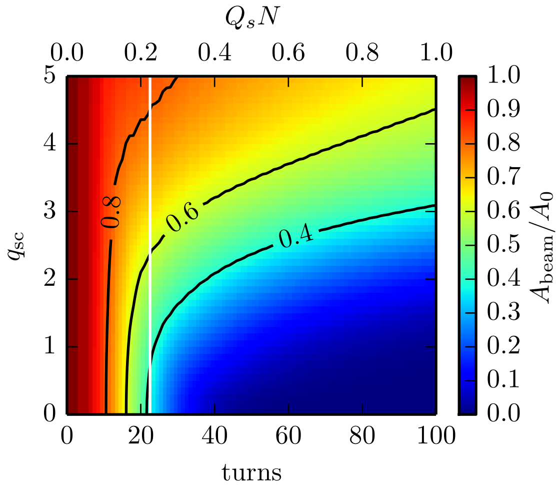

Figure 4.5.: Decoherence in bunches with space charge. Colors and solid lines are given by Eq. 4.5 with $q_{\mathrm{eff}} = 1$, and $Q_s = 0.01$. The vertical white line represents $N_{\mathrm{dec0}} = 22.5$ turns (Eq. 3.4).

beams can be also modified by impedances. We consider the effect of imaginary impedances that produce coherent tune shifts. The role of image charges in the decoherence process of coasting beams can be understood using the stability diagram. Image charges move the coherent tune shift towards the stability diagram shifted by space charge (Fig. 4.6). It means that image charges partly compensate the effect of space charge and can restore of Landau damping. In the similar way, the loss of decoherence can be removed for $\Delta Q_{\mathrm{ic}} \approx \Delta Q_{\mathrm{sc}}$ in coasting beams.

To illustrate the role of image charges in ion bunches, we consider the situation where $q_{\mathrm{sc}} \gg q_{\mathrm{eff}}$ and $q_{\mathrm{sc}} \gg q_{\mathrm{ic}}$, where the image charge parameter is

$$q_{\mathrm{ic}} = \frac{\Delta Q_{\mathrm{ic}}}{Q_s} \,. \tag{4.7}$$

In this case decoherence is lost for majority of longitudinal slices in the bunch. The tune shift induced by image charges in each slice can not restore decoherence locally, but ΔQ_{ic} varies along the bunch length. Thus, the bunch offset amplitude decreases because of the coherent tune spread which mixes betatron phases of different slices and causes intrabunch oscillations that can be modeled by

$$\langle x\rangle(N,z) = A_0 \cos\left(2\pi N Q_{\mathrm{coh}}(z)\right), \tag{4.8}$$

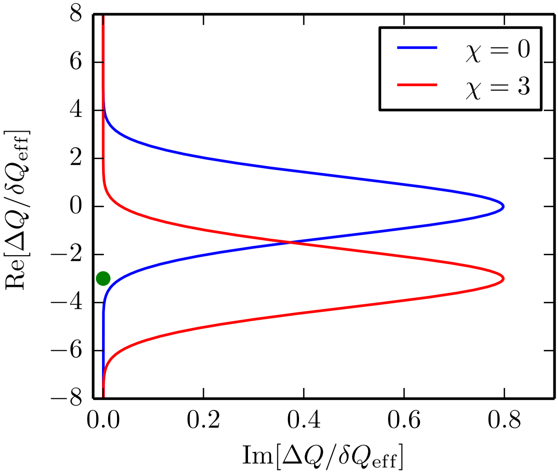

Figure 4.6.: Stability diagram with and without space charge from Eq. 2.39. The green point is the coherent tune shift due to image charges for $\Delta Q_{\mathrm{ic}} = \Delta Q_{\mathrm{sc}}$.

where $Q_{\mathrm{coh}}(z) = Q_0 - Q_s q_{\mathrm{ic}} \lambda(z)/\lambda_0$ is the local coherent tune of the slice. For a Gaussian longitudinal density the local bunch offset is shown in Fig. 4.7.

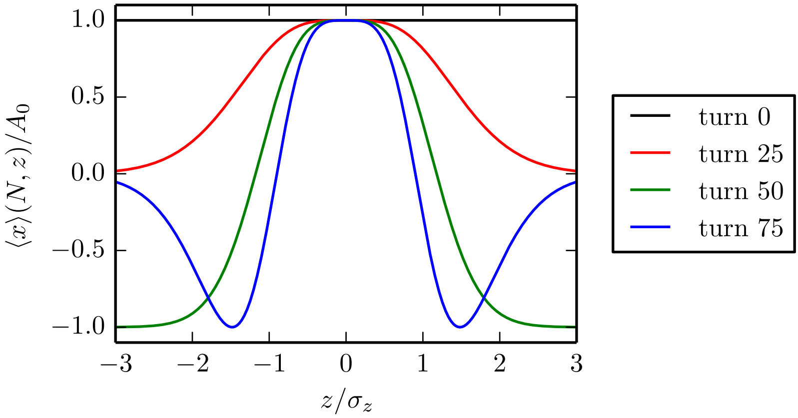

Figure 4.7.: Intrabunch oscillations caused by image charges and image currents given by Eq. 4.8 for $q_{\mathrm{ic}} = 1$ and $Q_s = 0.01$.

To describe the initial stage of decoherence in the presence of image charges, we neglect the synchrotron motion and consider a bunch as a superposition of longitudinal slices with different coherent tune shifts. We obtain the pulse response function as

$$G_{\mathrm{b,ic}}(N, q_{\mathrm{ic}}) = \frac{\int_{z_{\min}}^{z_{\max}} \cos\left(2\pi N Q_{\mathrm{coh}}(z)\right) \lambda(z) \mathrm{d}z}{\int_{z_{\min}}^{z_{\max}} \lambda(z) \mathrm{d}z}. \tag{4.9}$$

Integration of this equation results in a set of the bunch offset amplitudes that correspond to different q_{ic} and the turn number N. Performing the interpolation, we obtain the systematic behavior of decoherence due to image charges (Fig. 4.8). The contribution of image charges is negligible for $q_{\mathrm{ic}} < 0.5$, and decoherence is faster than the synchrotron period for $q_{\mathrm{ic}} > 1$.

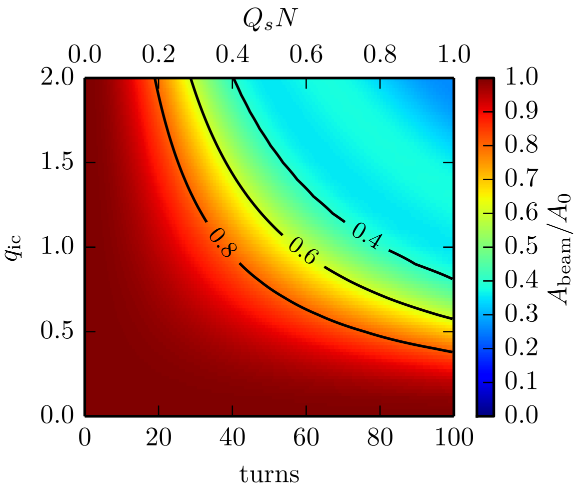

Figure 4.8.: Decoherence due to image charges. Colors and solid lines are calculated using Eq. 4.9 for $Q_s = 0.01$

4.4 Model for emittance blowup

Without space charge, the time evolution of emittance can be predicted from the oscillation envelope using Eqs. 3.17 or 3.18. To describe emittance growth in bunches with space charge and image charges, we use Eq. 3.18 in combination with the pulse response functions derived in previous sections,

$$\frac{\Delta\epsilon}{\epsilon_0} = \frac{1}{2}\frac{A_0^2}{\sigma_0^2}\left(1 - \left|G_{\mathrm{b,sc}} + i\mathscr{H}[G_{\mathrm{b,sc}}]\right|^2\right), \text{ for space charge,} \tag{4.10}$$

$$\frac{\Delta\epsilon}{\epsilon_0} = \frac{1}{2}\frac{A_0^2}{\sigma_0^2}\left(1 - \left|G_{\mathrm{b,ic}} + i\mathscr{H}[G_{\mathrm{b,ic}}]\right|^2\right), \text{ for image charges.} \tag{4.11}$$

Using the results of integration of Eq. 4.5 and Eq. 4.9, we get time evolution of the emittance blowup (Fig. 4.9). If we compare emittance blowup at a fixed N (for example at $N = N_{\mathrm{dec0}}$), the model predicts a smaller emittance blowup for stronger space charge. Intrabunch oscillations due to image charges produce stronger emittance blowup for larger q_{ic}.

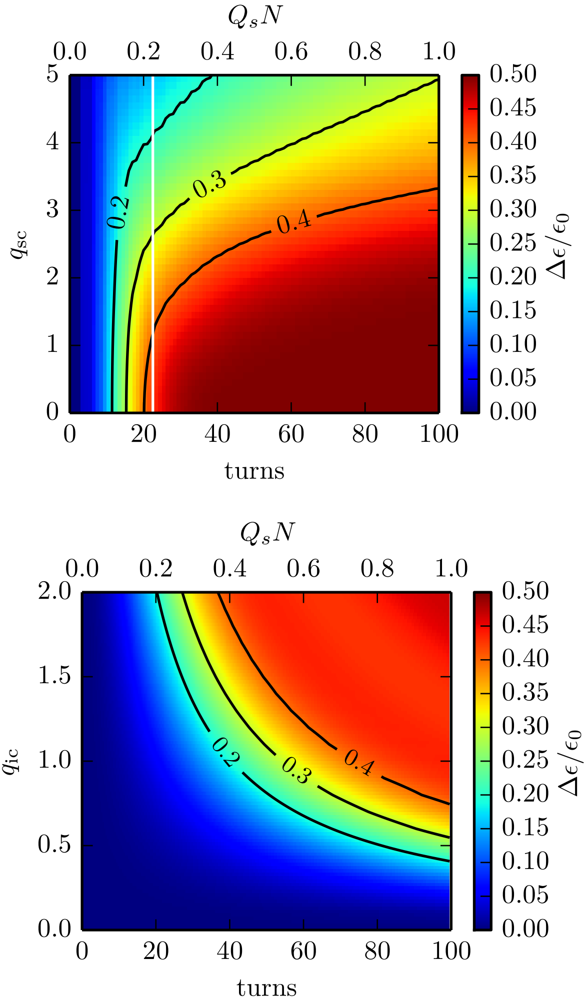

Figure 4.9.: Time evolution of the emittance blowup for decoherence with space charge given by Eq. 4.10 (the top plot) and for image charges given by Eq. 4.11 (the bottom plot). The vertical white line is $N_{\rm dec0} = 22.5$ turns (Eq. 3.4).

5 Simulations

For large accelerator complexes the time slots for measurements usually are limited. To study the effects for the planned accelerators simulations are used. Using new powerful supercomputers, allows to perform simulation scans for variety of system parameters. This allows to investigate new effects that can be further explained by simplified analytical models. In this work, a new GSI KRONOS cluster [65] was used to perform extensive simulation scans. Up to 800 cores were simultaneously used to perform the scans within an adequate time span of 4 hours.

To study the beam dynamics after the transverse kick, we perform simulations using a code derived from the particle tracking code PATRIC [66]. The transverse distribution dynamically changes during the decoherence process. This requires us to employ a self-consistent space charge solver for particle tracking simulations. In Sec. 5.1, we describe the simulation setup and main steps performed during the simulation run which are summarized in Fig. 5.1.

5.1 Computational model

A particle beam is represented as an ensemble of *macroparticles* in 6D phase space, each macroparticle corresponds to a number of real particles. At the beginning of a simulation run, particle coordinates are generated with the proper distributions according to the input parameters. For coasting beams, we use a Gaussian momentum distribution, and a uniform distribution in z. For bunched beams, a Gaussian distribution of longitudinal coordinates is used and momenta are generated according the distribution that is matched to the rf potential. Both types of particle beams have a Gaussian transverse profile. The distributions are truncated according to the certain criteria which are discussed below.

For the particle tracking, the constant-focusing lattice with bare tunes $Q_{0,x}, Q_{0,y}$ is used. The actual accelerator lattice is replaced by a set of identical elements with transport matrices given by Eq. 2.20. The number of elements corresponds to the number of simulation steps per revolution N_{st} and defines the time step $\Delta t = C/(v_0 N_{\mathrm{st}}) = \Delta s/v_0$. To perform self-consistent simulations of intense beams, the *particle-in-cell* method (PIC) [67] is employed. For every time step, a particle distribution is interpolated onto a grid. The potential of each grid point is obtained from the solution of the Poisson equation. Then, the interpolated electric field calculated from the potential is applied to the particle according to its position. In the general case, it is required to consider a 3D problem. However, for long ion bunches one can simplify this using the 2.5D space charge approach [66]. The particle density is interpolated onto a set of transverse 2D grids that divide the bunch into longitudinal slices (Fig. 5.2). On each 2D

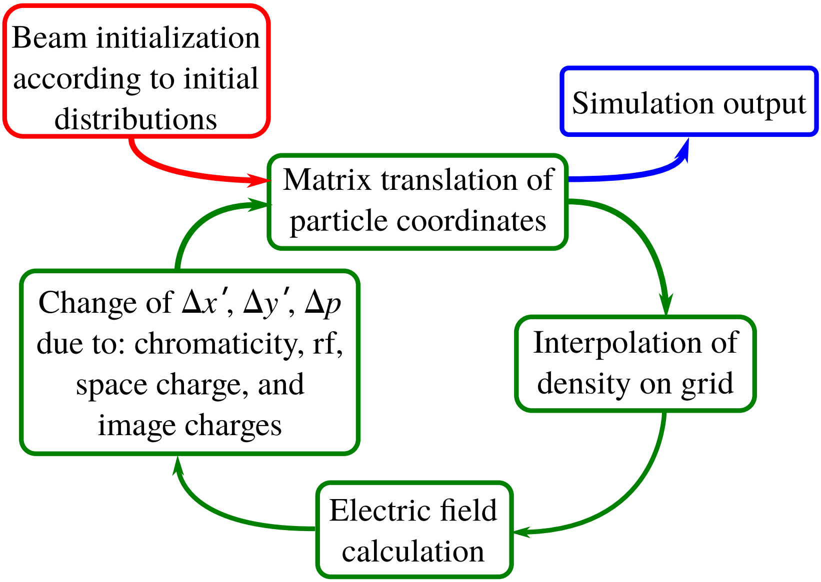

Figure 5.1.: Flowchart of the particle tracking simulations with a self-consistent space charge solver.

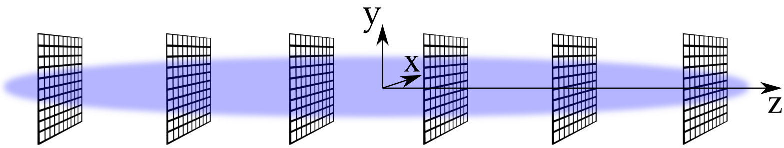

Figure 5.2.: Longitudinal slicing of the beam for the 2.5D space charge approach. According to the longitudinal particle position, the particle charge is interpolated between two neighbor transverse grids.

grid, the 2D Poisson equation is solved and longitudinal fields are neglected. For coasting beams, in absence of longitudinal fluctuations, the transverse beam profile does not depend on the longitudinal position. This allows us to reduce the calculation of transverse space charge fields to a 2D problem. To solve Poisson equation on a 2D grid, the code uses a fast FFT solver [67]. It is combined with the Green function technique in free space excluding the interaction with beam surroundings [68]. Then, the space charge force is applied to a particle as a transverse kick

$$\Delta x'_{\mathrm{sc}} = \frac{qE_{\mathrm{sc},x}(x,y,z)}{mc^2\beta^2\gamma^3}\Delta s, \tag{5.1}$$

where the electric field is interpolated to the position of the particle. After that, the interaction with beam surroundings is included via the impedance kick [66]. The kick due to image charges in a round pipe is given by

$$\Delta x'_{\mathrm{ic}} = 2\left(\frac{2\pi Q_0}{C}\right)^2 \frac{\Delta Q_{\mathrm{ic}}}{Q_0}\frac{\lambda(z)}{\lambda_0}x_{\mathrm{local}}(z)\Delta s \tag{5.2}$$

where x_{local} is the local offset of the beam, and the kick does not depend on the transverse particle position. The tune shift due to chromaticity is taken into account as a kick given by

$$\Delta x'_{\xi} = -2\left(\frac{2\pi Q_0}{C}\right)^2 \xi\frac{\Delta p}{p_0}x\Delta s. \tag{5.3}$$

For the longitudinal tracking in bunches, the kick approximation is applied such that for each particle z changes by the value

$$\Delta z = -\eta\frac{\Delta p}{p_0}\Delta s, \tag{5.4}$$

and once per turn the cavity kick is applied,

$$\frac{\Delta p}{p_0} \rightarrow \frac{\Delta p}{p_0} - \frac{qV}{\gamma mc^2\beta^2}f_{\mathrm{rf}}\left(\frac{2\pi hz}{C}\right), \tag{5.5}$$

where f_{rf} can be either linear or nonlinear function of the particle longitudinal coordinate depending on the rf potential. For coasting beams, the simulations are without longitudinal tracking, but each particle experiences the chromaticity kick according its momentum.

Time evolution of the beam offset and the transverse emittance is the standard output of the simulation run. Both fixed-time and fixed-position monitoring are implemented and available for simulations of the decoherence process.

5.2 Number of kicks per turn

In particle tracking simulations we use the kick approximation to model different effects which modify single-particle motion. In this section, we estimate N_{st} that is sufficient for accurate representation of the physical processes. To reproduce the integer part of the particle tune, the phase advance per simulation step should less then π. This gives the first limitation for the required number of steps $N_{\mathrm{st}} > 2Q_0$. In the presence of space charge or chromaticity, the transverse kick which corresponds to the incoherent tune shift ΔQ can be represented as a matrix

$$\mathbf{K} = \begin{pmatrix} 1 & 0 \\ -\frac{2\pi Q}{C}\frac{4\pi\Delta Q}{N_{\mathrm{st}}} & 1 \end{pmatrix}. \tag{5.6}$$

After each simulation step, the particle coordinates change according to the multiplication of matrices given by Eq. 2.20 and Eq. 5.6

$$\mathbf{M}_{\mathrm{st}} = \mathbf{M}_{\mathrm{CF}}(s+\Delta s, s)\mathbf{K} = \begin{pmatrix} \cos\left[\frac{2\pi Q_0}{N_{\mathrm{st}}}\right] - \frac{4\pi\Delta Q}{N_{\mathrm{st}}}\sin\left[\frac{2\pi Q_0}{N_{\mathrm{st}}}\right] & \frac{C}{2\pi Q}\sin\left[\frac{2\pi Q_0}{N_{\mathrm{st}}}\right] \\ -\frac{2\pi Q}{C}\left(\sin\left[\frac{2\pi Q_0}{N_{\mathrm{st}}}\right] + \frac{4\pi\Delta Q}{N_{\mathrm{st}}}\cos\left[\frac{2\pi Q_0}{N_{\mathrm{st}}}\right]\right) & \cos\left[\frac{2\pi Q_0}{N_{\mathrm{st}}}\right] \end{pmatrix}. \tag{5.7}$$

From this matrix we get the effective particle tune

$$Q_{\mathrm{eff}} = \frac{N_{\mathrm{st}}}{4\pi}\mathrm{Tr}\left[\mathbf{M}_{\mathrm{st}}\right] = \frac{N_{\mathrm{st}}}{2\pi}\arccos\left(\cos\left[\frac{2\pi Q_0}{N_{\mathrm{st}}}\right] - \frac{\Delta Q}{Q_0}\frac{2\pi Q_0}{N_{\mathrm{st}}}\sin\left[\frac{2\pi Q_0}{N_{\mathrm{st}}}\right]\right), \tag{5.8}$$

where $\mathrm{Tr}[\mathbf{M}_{\mathrm{st}}]$ is the trace of the matrix. The difference between Q_{eff} and the expected tune $Q_0 + \Delta Q$ depends on the number of steps per turn and saturates for $N_{\mathrm{st}} > 4\pi Q_0$ (Fig. 5.3). This region is preferred for simulations because the saturated error depends only on the ratio $\Delta Q/Q_0$ (Fig. 5.4). To reduce the systematic error in our simulations, we construct the transfer matrices from the total bare tune instead of using only the fraction part of the tune.

The discussed calculation of the error assumes the identical kicks for each simulation step within one turn. This is valid for the tune shifts produced by chromaticity and for the case of linear space charge force. Considering the Gaussian transverse distribution, the particles have the amplitude-dependent tune shift. In the beam center the space charge force is linear and produce the strongest tune depression. In this region the tune error can be estimated from Eq. 5.8. For particles with larger amplitude the transverse kick is nonlinear that results in a smaller overall tune shift after one revolution. Thus they have a smaller tune error of the same order as expected value but with the opposite sign (Fig. 5.5).

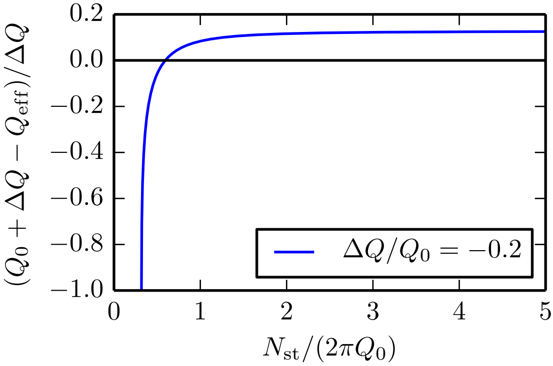

Figure 5.3.: Tune error as a function of number of cells (Eq. 5.8).

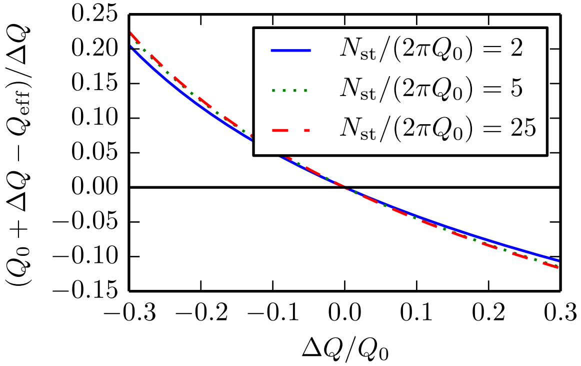

Figure 5.4.: Decoherence of the saturated systematic error on the tune shift for $N_{\text{st}} > 4\pi Q_0$.

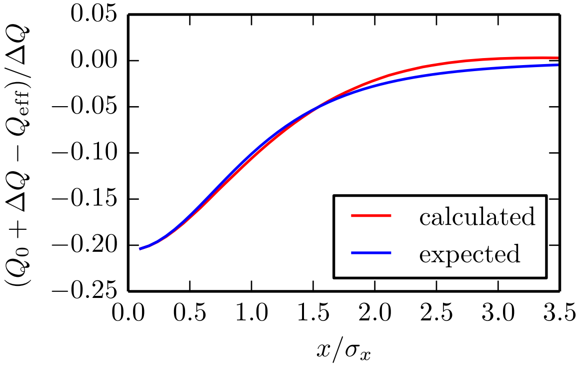

Figure 5.5.: The saturated systematic error of the particle in the presence of nonlinear space charge force. The tune shift due to space charge ΔQ is given by Eq. 2.33 for $\epsilon_{\mathrm{sp},y} = 0$ and $\epsilon_{\mathrm{sp},x} = x^2 2\pi Q_0/C$.

5.3 Validation

In the following subsections, we discuss the validation examples of the PATRIC code and requirements for self-consistent simulations of the decoherence process. For the presented simulation results, we use round beams with different horizontal and vertical bare tunes and transverse emittances. In this case, the both transverse plane are uncoupled and we can avoid the emittance exchange [69].

5.3.1 Space charge and image charges

To validate the space charge solver, we compare the tune distribution from the simulations with distributions obtained using the statistical method (Figs. 2.4 and 2.5). The particle tune is calculated from the particle coordinates using either the One-Turn-Matrix (OTM) method [70] or the Average Phase Advance (APA) method [71]. The latter has an advantage that it can be used for case when the space charge tune shift exceeds the fractional part of the bare tune. However, it requires knowledge of the bare tune.

The tune distribution depends on the truncation of the beam profile (Fig. 5.6). The truncation of the distribution changes the transverse field configuration and the peak transverse density. Starting from $3.5\sigma_0$ cut, the tune distribution agrees well with analytical expectation discussed in Sec. 2.3.

Space charge force calculation depends on the number of macroparticles N_{M} and the grid resolution. For decoherence simulations, we are interested in the time scale of one synchrotron period (usually 10^2—10^3 turns), where the change of transverse distribution

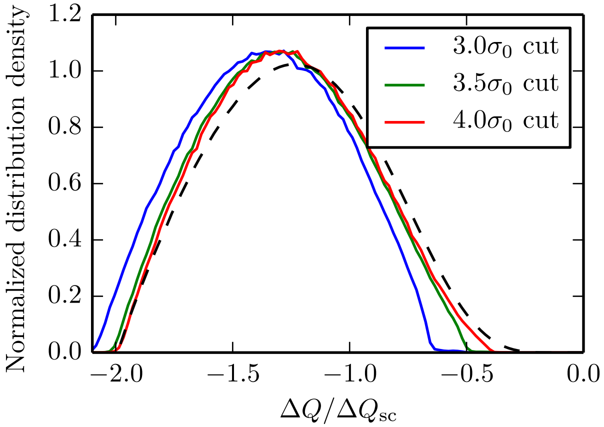

Figure 5.6.: Tune distribution obtained from simulations for a round beam with different truncation of a Gaussian transverse profile. The dashed line is given by the statistical method discussed in Sec. 2.3. Simulation parameters: $Q_{x,0} = 4.29$, $Q_{y,0} = 4.27$, $N_{\mathrm{M}} = 10^6$, and $N_{\mathrm{st}} = 60$.

due to phase-mixing has to be resolved. For most cases in this work, the transverse grid contains 128 × 128 cells and covers the beam with the truncation at $3.5\sigma_0$. The number of macroparticles for 2D simulations is $N_{\mathrm{M}} \sim 10^6$, and for simulations with bunches we can use up to 10^8 macroparticles. To speed up simulations for bunch beams, the calculations are parallelized via MPI [72]. The macroparticles are distributed between processors according to their longitudinal position. After the interpolation process, each processor solves the Poisson equation for the set of transverse grids. The line density variation results in variation of the space charge strength depending on z. To reproduce this effect, the sufficient number of transverse grids should be chosen. Depending on the space charge strength, in our simulations it varies from 40 to 120 grids per bunch.

The truncation of a longitudinal Gaussian distribution affects the local line density (Fig. 5.7). In simulations, we truncate the longitudinal beam profile at $3\sigma_z$ and the distribution of particle momenta at $3\delta p$. In this case the tune distribution of particles in the bunched beam from simulations sufficiently reproduce the analytical expectation (Fig. 5.8).

For the case of displaced beams, OTM and APA methods are not valid for the tune calculation because the particle motion is affected by the coherent oscillations. To validate the kick due to the image charges, we apply the initial offset to the 2D beam and observe the spectrum of the beam oscillations over 1000 turns. We see that the peak of the spectrum corresponds to the coherent tune shifted due to image charges and image currents (Fig. 5.9).

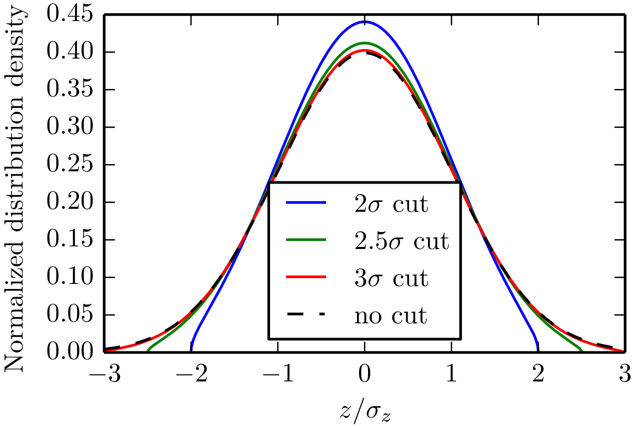

Figure 5.7.: Longitudinal Gaussian distributions with different truncations.

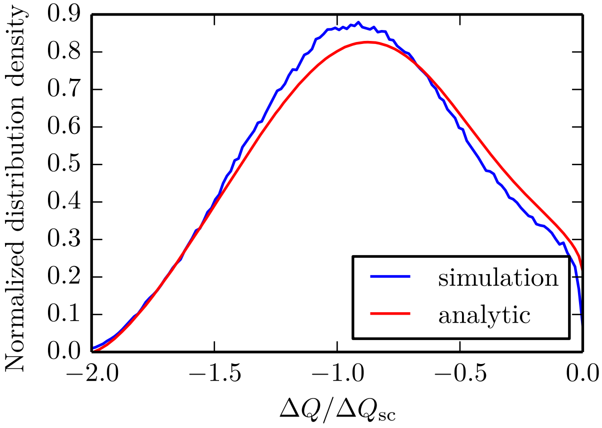

Figure 5.8.: Tune distribution obtained from simulations for the bunched beam with a Gaussian truncated transverse ($3.5\sigma_0$) and longitudinal ($3\sigma_z$) profiles.

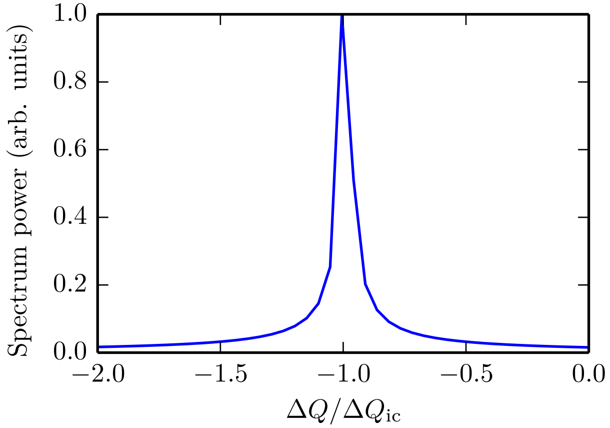

Figure 5.9.: Spectrum of the coherent beam oscillations in the presence of image charges. Simulation parameters: $Q_{0,x} = 4.29$, $Q_{y,0} = 3.27$, $\Delta Q_{\mathrm{ic}} = 0.02$.

5.3.2 Transverse decoherence for fixed-time and fixed-position monitoring

In this section, we compare the time evolution of the bunch offset after the initial displacement with analytic expressions presented in Chap. 3. For both fixed-time and fixed-position monitoring, the bunch offsets from simulations perfectly agree with Eq. 3.9 with the proper substitution of parameter q_ξ (Fig. 5.10). In this example, for the same chromaticity $\xi < 0$ and $\eta < 0$, decoherence observed at the fixed position is faster than decoherence observed at the fixed time.

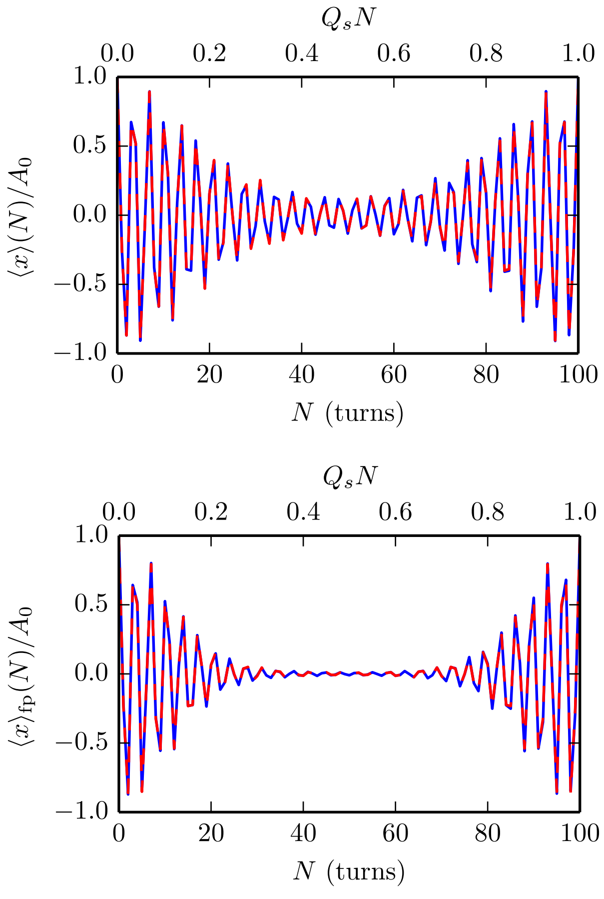

Figure 5.10.: Decoherence of the bunch observed using the fixed-time monitoring (the top plot) and the fixed-position monitoring (the bottom plot). Blue lines represent the time evolution of the beam offset from particle tracking simulations. Red dashed lines are given by Eq. 3.9 (the top plot). For the bottom plot, q_ξ is substituted by q_{eff}. Simulation parameters: $Q_{0,x} = 4.29$, $Q_s = 0.01$, $q_\xi = 1$, and $q_{\mathrm{eff}} = 1.5$.

6 Simulation results

In this chapter we discuss the simulation results and compare with the analytical predictions (Chap. 4). To cover the different regimes of the decoherence process, the extensive simulation scans have been carried out using GSI KRONOS cluster [65].

6.1 2D simulations

Starting with the 2D case, we verify the pulse response function with space charge given by Eq. 4.2. Derived for the linear space charge force, it agrees very well with simulations for a Gaussian transverse distribution for particular beam parameters (Fig. 6.1). To check an agreement for various strength of space charge, we performed a simulation scan with finite steps of the space charge parameter. We calculate the bunch offset amplitude as $\sqrt{\langle x\rangle^2 + \langle x'\rangle^2 (C/(2\pi Q_0))^2}$, and get an interpolated plot from the 2D arrays, similarly to Fig. 4.2. According to simulation scan for different space charge strength and the same effective spread, the model and the simulations agree for $\chi < 2$ or for $N < N_{\mathrm{dec0}}$ (Fig. 6.2). For stronger space charge ($\chi > 2$), decoherence is faster from simulations, and for $\chi > 4$ the loss of decoherence is also observed.

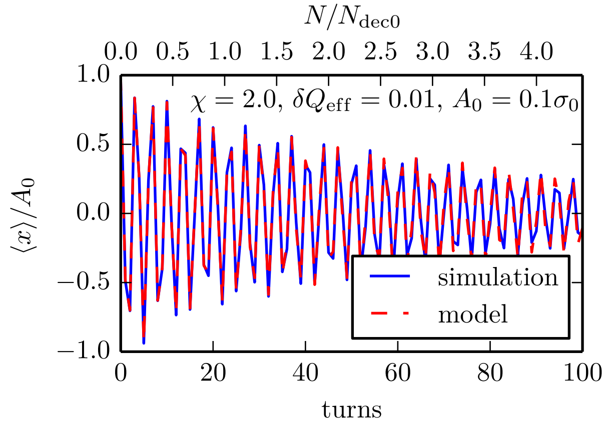

Figure 6.1.: Comparison of decoherence from the model (Eq. 4.2) and 2D simulations.

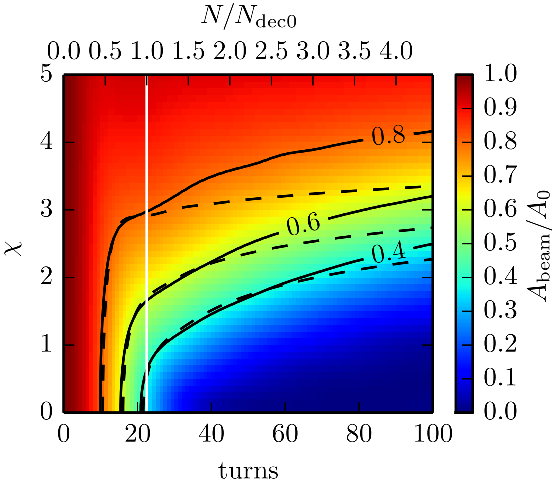

Figure 6.2.: Time evolution of the beam oscillation amplitude for 2D beams with different space charge, $\delta Q_{\text{eff}} = 0.01$, $A_0 = 0.1\sigma_0$. Colors and the solid lines (contour lines) are from simulations. Dashed lines are given by Eq. 4.2. The vertical white line is $N_{\text{dec0}} = 22.5$ turns (Eq. 3.4).

It is suggested that this difference is related to the particle excitation by coherent oscillations of the beam. In simulations we observe that some particles gain large amplitudes. They create a halo around the beam core and can be lost depending on the aperture size. The number of lost particles depends on the combination of space charge and the kick strength (Fig. 6.3). There are no excited particles for $\chi < 2$ where fast decoherence is present. The number of lost particles reaches maximum in the transition region before decoherence is lost and then decreases for stronger space charge. We also see that larger initial kicks lead to stronger losses. All these observations support the resonant excitation driven by the space charge force.

6.2 Halo buildup due to coherent oscillations and space charge

Here, we discuss the mechanism of halo buildup and losses observed in our simulations. To describe interaction of a particle with the coherent oscillations of the beam, we derive a particle-core model, similarly to Wangler at al. [73]. The considered model is not self-consistent because particles do not affect the beam centroid coordinate x_0 given by a simple harmonic equation

$$x_0(N) = A_0 \cos(2\pi Q_0 N). \tag{6.1}$$

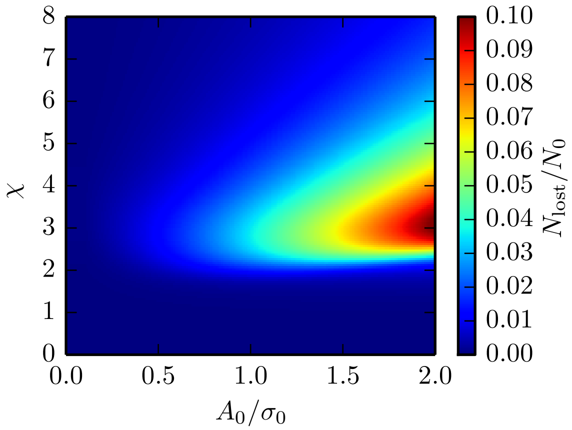

Figure 6.3.: Beam losses due to transverse excitation by coherent motion with space charge. The particles with the amplitude above $a_i = 3.5\sigma_0 + A_0$ are counted as lost particles and are removed from further calculations. The losses are saturated after 250 turn. The simulation scan is performed for $\delta Q_{\mathrm{eff}} = 0.01$.

This corresponds to the case when decoherence is lost ($\chi > 3$) and the beam continuously oscillates after the initial offset A_0. The single-particle equation of motion can be modeled as

$$\frac{\mathrm{d}^2 x}{\mathrm{d}N^2} + (2\pi Q_0)^2 \left(x - a f_{\mathrm{sc}} - a f_{\xi}\right) = 0, \tag{6.2}$$

where x is the transverse coordinate of a particle. Here, the normalized space charge force given for a KV transverse distribution with a beam radius a is given by

$$f_{\mathrm{sc}} = \begin{cases} \frac{2\Delta Q_{\mathrm{sc}}}{Q_0}\frac{x-x_0}{a}, & |x-x_0| < a \\ \frac{2\Delta Q_{\mathrm{sc}}}{Q_0}\frac{a}{(x-x_0)}, & |x-x_0| \geq a \end{cases} \tag{6.3}$$

and an additional focusing force due to chromaticity is

$$f_{\xi} = \frac{2\Delta Q_{\xi}}{Q_0}\frac{x}{a}. \tag{6.4}$$

The tune shift parameters ΔQ_{sc} and ΔQ_{ξ} relate to the single-particle tune $Q = Q_0 - \Delta Q_{\mathrm{sc}} + \Delta Q_{\xi}$. The particle can be excited if its tune is close to the coherent tune. It is assumed that the number of excited particles is small, and the field distribution does not change.

We solve Eq. 6.2 numerically using the leapfrog method [74] and present the results using a stroboscopic phase space map of an array of particle trajectories. The stroboscopic method accumulates many snapshots of a phase space taken once per oscillation period. In our case it is taken when the beam offset reaches the maximum value.

The chromaticity alone, and space charge alone, can not lead to a particle excitation. For example, for all of the 11 testparticles with different ΔQ_ξ and $\Delta Q_{\mathrm{sc}} = 0$, the amplitude of oscillations with respect to the closed orbit does not increase(Fig. 6.4). Due to different tunes particles redistribute in phase space. In the presence of space charge, the oscillation amplitude is constant with respect the beam center and particles remain in the beam core (Fig. 6.5).

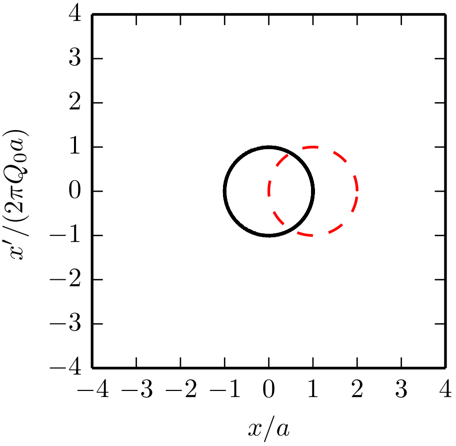

Figure 6.4.: Stroboscopic plot for 11 particles for zero space charge. The chromaticity tune shift ΔQ_ξ in the range of $[-0.03, 0.03]$, and all particles have zero initial amplitude with respect the beam center, $A_0 = a$. The red dashed circle is area ocupied by the beam in phase space. The plot contains 100 betatron periods.

The numerical solution for combination of effects is demonstrated for the case of 32 particles that have initial conditions $x = x_0$ and $x' = 0$ (Fig. 6.6). In this case, particles with tunes $Q \in [4.26, 4.27]$ are exited and leave the beam core because their incoherent tunes are close to $Q_0 = 4.29$. The rest particles oscillate inside the beam core. This example demonstrates the resonant excitation by the space charge force which we observe in the simulations for coasting beams in Sec. 4.1.

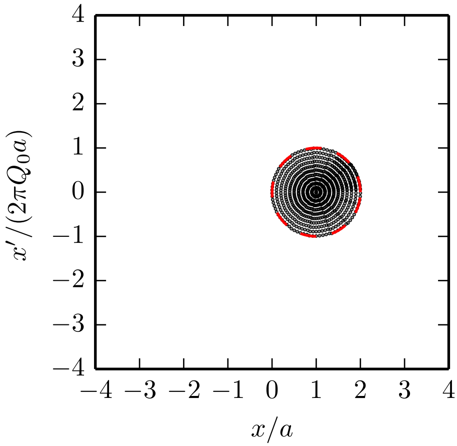

Figure 6.5.: Stroboscopic plot for 11 particles for zero chromaticity, different initial offsets in the range $[0, a]$, $\Delta Q_{\mathrm{sc}} = 0.05$, and $A_0 = a$. The red dashed circle is area occupied by the beam in phase space. The plot contains 100 betatron periods.

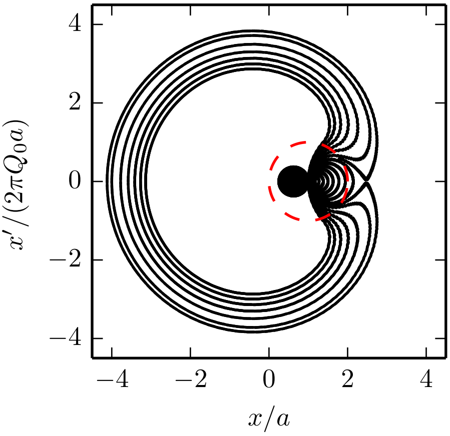

Figure 6.6.: Stroboscopic plot for 32 particles with different chromaticity tune shift ΔQ_ξ in the range $[-0.03, 0.03]$ and $\Delta Q_{\mathrm{sc}} = 0.05$, $Q_0 = 4.29$, $A_0 = a$. All particles have zero initial amplitude with respect to the beam center. The plot contains 800 betatron periods.

6.3 Simulations for bunched beams

In this section, we compare our simulations for bunches with the extended analytical model (Eq. 4.5). Without space charge, the beam oscillation amplitude corresponds to alternating decoherence and recoherence processes (Fig. 6.7). With space charge, decoherence is slower, recoherence is not related to Q_s, and after the transition time we have the beating of the remaining head-tail modes [33].

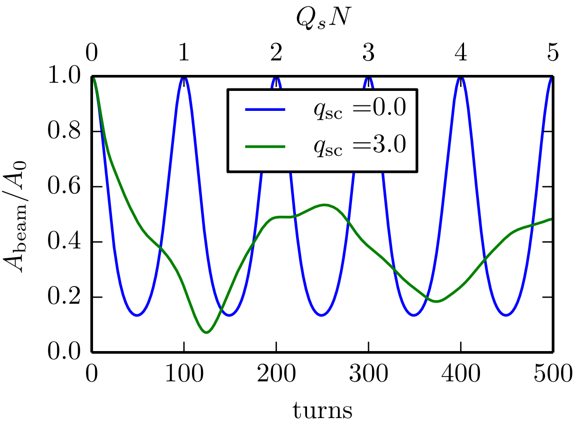

Figure 6.7.: Time evolution of the oscillation amplitude from simulations for bunches with Gaussian transverse and longitudinal distribution. Bunch parameters: $q_{\text{eff}} = 1, A_0 = \sigma_0, Q_s = 0.01$.

The simulation scan for different space charge shows that the model agrees well with simulations for $N < N_{\text{dec0}}$ as it is for coasting beams (Fig. 6.8). For $N > N_{\text{dec0}}$ decoherence in simulations is faster than decoherence from the model. The first reason is the resonant excitation of the particles which leads to fast losses (Fig. 6.9). The number of lost particles depends on the combination of different parameters: q_{sc}, q_{eff}, A_0, and the aperture radius. It would require a detailed analysis of simulations with a realistic lattice which is beyond the scope of this work. The second reason of the faster decoherence in simulations is the synchrotron motion. It produces an additional mixing of particles which is not included in the extended model.

The time evolution of the emittance from the same simulation scan shows that the model for emittance growth (Eq. 4.10) sufficiently well reproduces the simulation results (Fig. 6.10). Without space charge, there is an emittance growth for $N < N_s/2$. Later on, the emittance returns to the initial value after by $N = N_s$ as expected from Eq. 3.17.

The pulse response function does not depend on the initial oscillation amplitude, by definition, but the maximum emittance blowup is directly defined by A_0 (see Eq. 3.19).

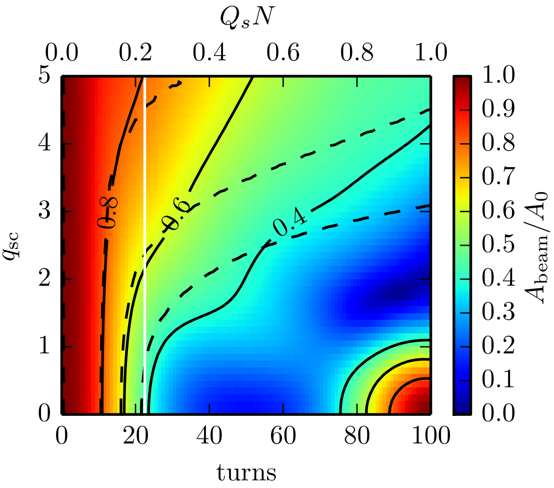

Figure 6.8.: Decoherence in bunches with space charge. Colors and solid lines are from simulations. Dashed contour lines are given by Eq. 4.5. The vertical white line is $N_{\text{dec0}} = 22.5$ turns (Eq. 3.4). Bunch parameters: $q_{\text{eff}} = 1$, $A_0 = \sigma_0$, $Q_s = 0.01$.

We compare decoherence for different A_0 in Fig. 6.11. Simulations with $q_{\text{sc}} = 4$ for $A_0 = 0.5\sigma_0$ and $A_0 = 1.0\sigma_0$ are almost identical and agree with the model (the dashed line) for $N < N_{\text{dec0}}$ (the top plot in Fig. 6.11). For the larger initial offset, decoherence is a bit faster due to stronger losses. Situation is similar for the emittance: the analytical approach (Eq. 4.10) reproduces the simulations for $N < N_{\text{dec0}}$ (the bottom plot in Fig. 6.11).

We find in simulations that the characteristic decoherence time N_{dec} depends on q_{sc} and q_{eff}. According to the simulation scan for different combination of these parameters for $A_0 = \sigma_0$, decoherence is slower for stronger space charge and the decoherence time can exceed the synchrotron period (Fig. 6.12). For larger effective spread we have a faster decoherence. In measurements, if the parameter q_{eff} is known, the decoherence time will allow to determine the space charge parameter q_{sc}.

6.4 Simulations with image charges

Simulations of decoherence process in the presence of space charge, chromaticity, and image charges are presented in this section. As we discussed in Sec. 4.2, the numerical evaluation of Eq. 4.5 is limited by $q_{\text{sc}} < 5q_{\text{eff}}$. Simulation for $q_{\text{sc}} > 15q_{\text{eff}}$ demonstrate loss of decoherence in bunches (Fig. 6.13). For the fixed ratio of the beam size and the

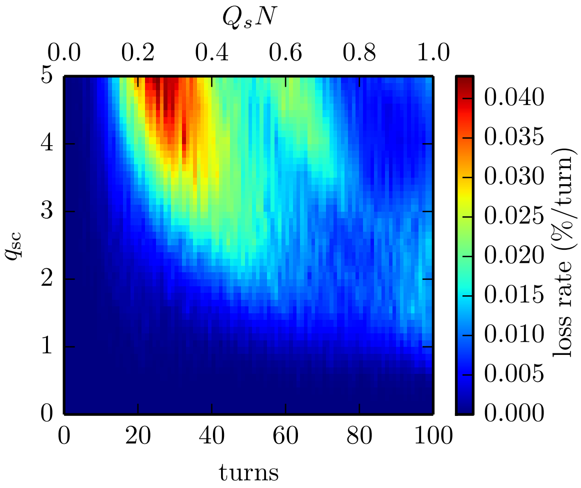

Figure 6.9.: Loss rate for different space charge from the simulation scan shown in Fig. 6.8. The aperture radius is $3.5\sigma_0 + A_0$.

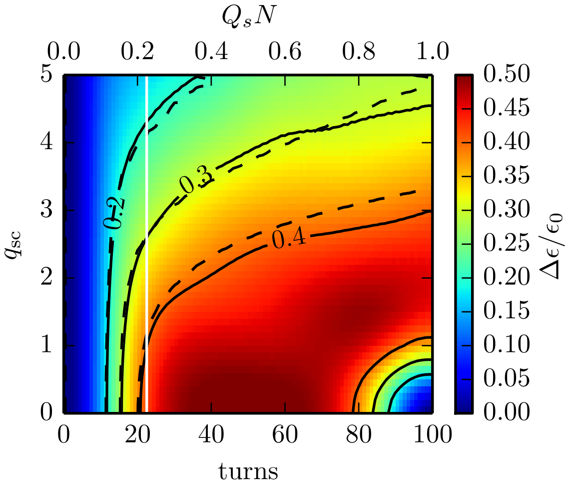

Figure 6.10.: Time evolution of the emittance blowup for decoherence with space charge shown in Fig. 6.8. Colors and solid lines are from simulations for bunches. Dashed lines are calculated using Eq. 4.10 from the oscillation amplitude given by Eq. 4.5. The vertical white line is $N_{\mathrm{dec0}} = 22.5$ turns (Eq. 3.4).

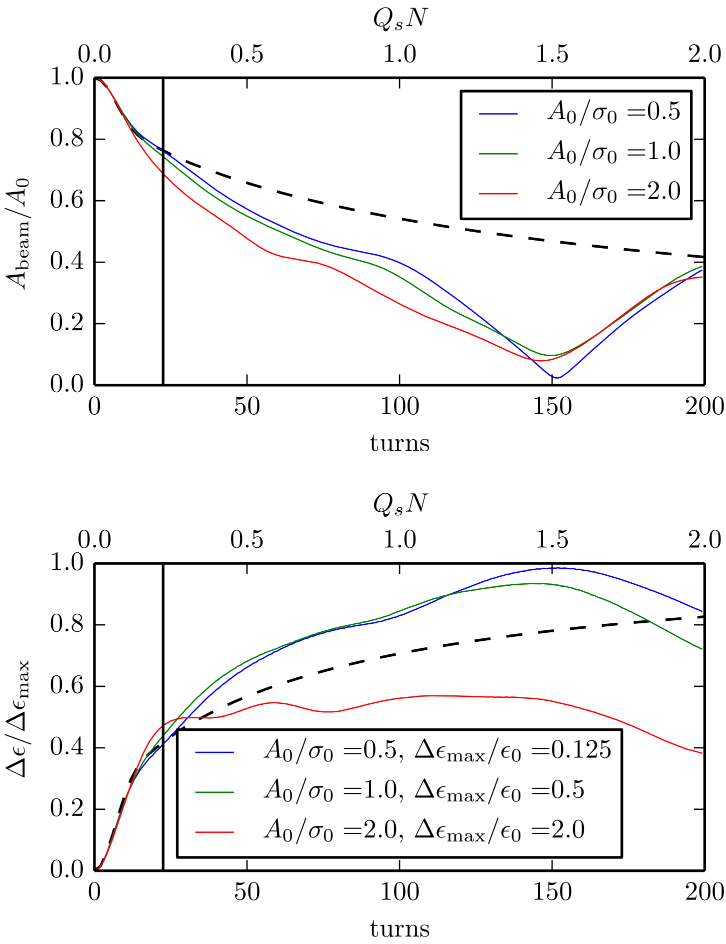

Figure 6.11.: Decoherence for different initial kick strength. The top plot is the time evolution of the beam oscillation amplitude. The dashed line is given by Eq. 4.5. The bottom plot is the time evolution of the emittance blowup. The dashed line is calculated using Eq. 4.10. The maximum emittance growth without space charge $\Delta\epsilon_{\mathrm{max}}$ is given by Eq. 3.19. The vertical black line is $N_{\mathrm{dec0}} = 22.5$ turns (Eq. 3.4). Bunch parameters are $q_{\mathrm{sc}} = 4$, $q_{\mathrm{eff}} = 1$, and $Q_s = 0.01$.

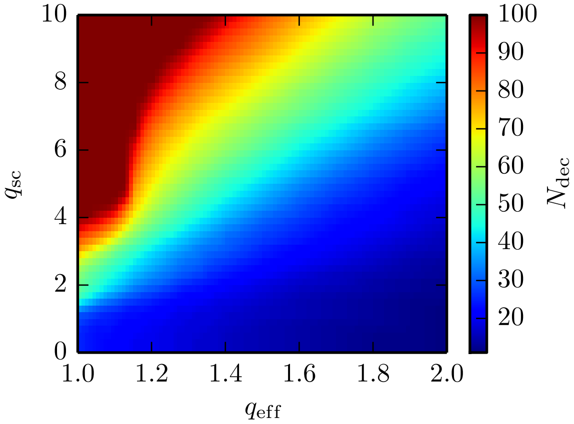

Figure 6.12.: The decoherence time for difference space charge and the effective tune spread. Beam parameters: $A_0 = \sigma_0$, $Q_s = 0.01$

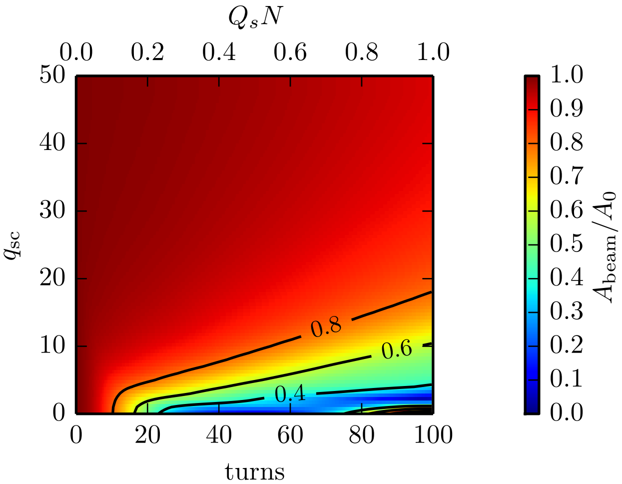

Figure 6.13.: Loss of decoherence in bunches with space charge from the simulation scan. Simulation parameters: $q_{\mathrm{eff}} = 1, A_0 = \sigma_0$, and $Q_s = 0.01$.

beam pipe, the tune shift induced by image charges is linearly proportional to the space charge strength (see Eq. 2.37). We compare the simulation scan shown in Fig. 6.13

with the simulation scan with included image charges for $a/b = 1/5$ (Fig. 6.14). We see that for $q_{\mathrm{ic}} < 0.5$ the coherent tune spread is small and decoherence is dominated by interplay of chromaticity and space charge. For $q_{\mathrm{ic}} > 1$, when conditions $q_{\mathrm{sc}} \gg q_{\mathrm{eff}}$ are fulfilled, the decoherence process can be sufficiently reproduced by the model of coherent tune spread (Eq. 4.9). In the intermediate region, all three effects contribute to the evolution of the beam offset.

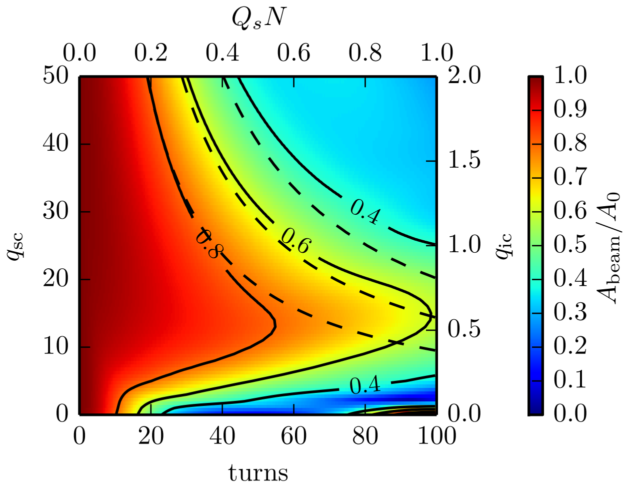

Figure 6.14.: Decoherence in bunches with space charge and image charges. Colors and solid lines are from simulations. Dashed lines are given by Eq. 4.9. Simulation parameters: $a/b = 1/5$, $q_{\mathrm{eff}} = 1$, $A_0 = \sigma_0$, $Q_s = 0.01$.

Time evolutions of the emittance blowup from simulation and from the model (Eq. 4.11) are compared in Fig. 6.15. In the image charges dominated region, the initial stage of the decoherence process agrees well with the analytical expectation. Starting from $N > N_s/2$ beam blowup is saturated and then reduces due to fast losses (the bottom plot in Fig. 6.15). This could be also related to the resonant excitation of particles driven by coherent oscillations and space charge. The more detailed understanding is a subject of further analysis which is not covered in the present work.

6.5 Simulations with nonlinear rf fields

As we discussed in Chap. 3, without intensity effects, the oscillation amplitude of the offset beam is modulated by alternating decoherence and recoherence processes. After each synchrotron period, the betatron phase spread is compensated, and the bunch

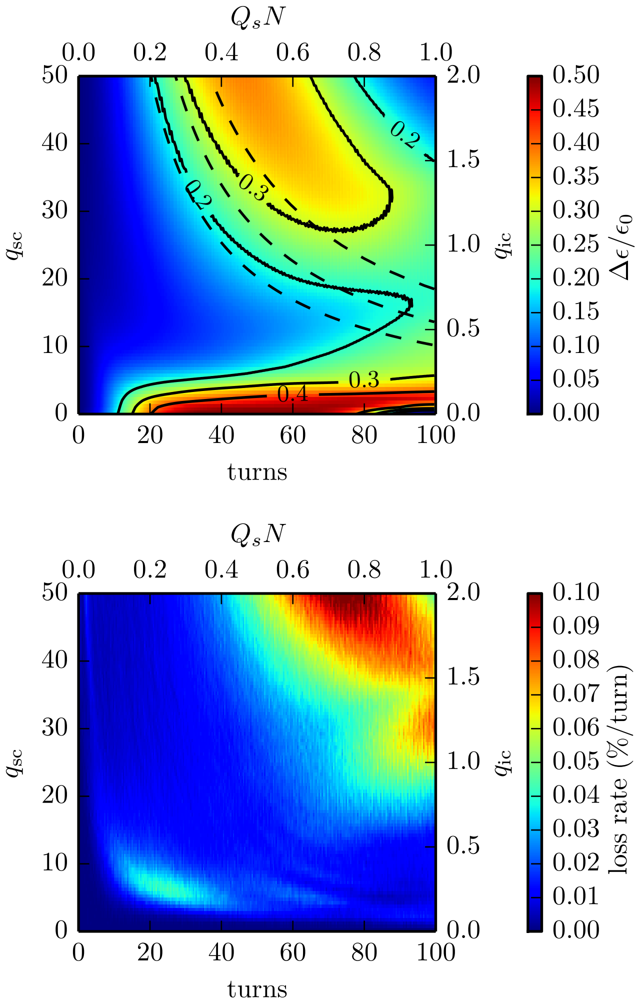

Figure 6.15.: Time evolution of the emittance blowup (the top plot) and losses (the bottom plot) for decoherence with space charge shown in Fig. 6.14. Colors and solid lines are from simulations for bunches. Dashed lines are calculated using Eq. 4.11. Simulation parameters: $a/b = 1/5$, $q_{\text{eff}} = 1$, $A_0 = \sigma_0$, $Q_s = 0.01$.

offset returns to the initial value. In the presence of non-linear synchrotron motion, the phase spread will not be fully compensated that can affect the recoherence processes. The results of the simulation scan for different bunch length show that the decoherence process is not affected by rf nonlinearities (Fig. 6.16). Thus, we neglect them also for the initial stage of decoherence with space charge and image charges. A small deference can be due to a change of the longitudinal beam profile for the match longitudinal distribution.

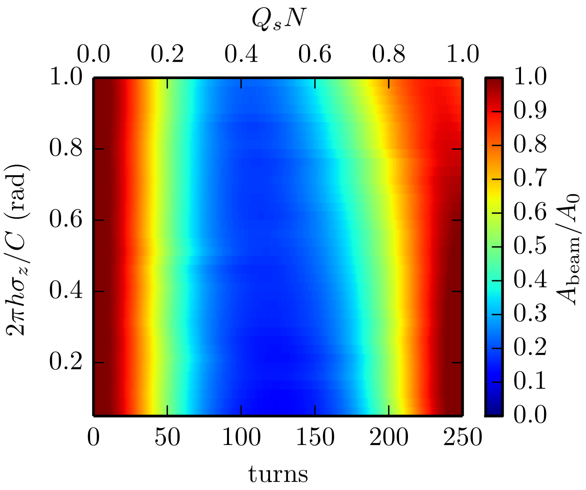

Figure 6.16.: Decoherence in bunches without space charge for different bunch length from simulations with sinusoidal rf fields. Bunch parameters: $q_{\rm eff} = 1$, $A_0 = \sigma_0$, $Q_s = 0.01$.

6.6 Summary of decoherence simulations in bunches

In general case, it is necessary to compare the space charge tune shift, the coherent tune shift, and the effective tune spread to understand which effect dominates the initial stage of the decoherence process. Image charges play no role for $q_{\rm ic} < 0.5$. Space charge slows down decoherence. If decoherence is lost for majority of longitudinal slices, the bunch offset amplitude does not change within the first synchrotron period. For the case where $q_{\rm ic} \approx 1$, decoherence is governed by interplay of chromaticity, space charge and image charges. It will be faster than decoherence given only by chromaticity and space charge. When the conditions $q_{\rm sc} \gg q_{\rm eff}$ and $q_{\rm ic} > 1$ are fulfilled decoherence is dominated by image charges.

7 Measurements

In this chapter, we discuss measurements in the SIS18 synchrotron at GSI Darmstadt and the comparisons with simulations. For the intensities achieved in the experiments we show that the initial stage of the decoherence process is mainly governed by the chromaticity and by space charge.

7.1 Experimental setup

We performed the decoherence measurements for intense ion beams in the SIS18 synchrotron [12] at GSI Darmstadt. In each cycle, four bunches of Ni_{58}^{26+} ions were stored at the kinetic energy of 100 MeV/u and kicked transversally with the kick duration of one turn. The bunch offset signals were simultaneously recorded using 12 BPMs. SIS18 general parameters and settings in our experiments are listed in Tab. 7.1. The number of particles per beam varied between $N_p = 1.6 \times 10^9$ and $N_p = 4 \times 10^9$.

7.2 Measurements of beam and machine parameters

To evaluate and compare decoherence signals from measurements, we need to determine the parameters q_{sc} and q_{eff}. In this section, we briefly discuss the diagnostics and methods which are used to measure the transverse beam size, the bunch length, and the machine chromaticity.

7.2.1 Beam position and the longitudinal profile

To measure the beam position, 12 shoe-box pick-ups are available in the SIS18 synchrotron. A BPM consists of two pairs of parallel plates for detection of the horizontal

Machine parameter	Symbol	Value
Horizontal tune	$Q_{0,x}$	4.29
Vertical tune	$Q_{0,y}$	3.27
Harmonic number	h	4
Slip factor	η	-0.79
Synchrotron tune	Q_s	4.1×10^{-3}

Table 7.1.: Machine parameters during the decoherence experiment.

and the vertical beam position. A particle beam passing by the BPM induces image charges on each pair of plates. The induced signals are proportional to the local beam current and to the local beam offset. In the vertical plane, it can be expressed by

$$\begin{aligned} U_\mathrm{u}(t) &\propto \lambda(t)(1+S_y y_\mathrm{local}(t)), \\ U_\mathrm{d}(t) &\propto \lambda(t)(1-S_y y_\mathrm{local}(t)), \end{aligned} \tag{7.1}$$

and similarly for the horizontal plane

$$\begin{aligned} U_\mathrm{l}(t) &\propto \lambda(t)(1+S_x x_\mathrm{local}(t)), \\ U_\mathrm{r}(t) &\propto \lambda(t)(1-S_x x_\mathrm{local}(t)), \end{aligned} \tag{7.2}$$

where S_y, and S_x are the sensitivities of the pick-up in the vertical and the horizontal plane, correspondingly. The horizontal local beam offset is then given by

$$x_\mathrm{local}(t) = \frac{1}{S_x}\frac{U_\mathrm{l}(t)-U_\mathrm{r}(t)}{U_\mathrm{l}(t)+U_\mathrm{r}(t)}, \tag{7.3}$$

and the vertical local beam offset is

$$y_\mathrm{local}(t) = \frac{1}{S_x}\frac{U_\mathrm{u}(t)-U_\mathrm{d}(t)}{U_\mathrm{u}(t)+U_\mathrm{d}(t)}. \tag{7.4}$$

The sensitivity of all BPM are similar in SIS18 [75]: $S_x = 6\times10^{-3}$ mm^{-1}, and $S_y = 20\times10^{-3}$ mm^{-1}.

Capacitive pick-ups can not transmit the DC component of the signal and are suitable only for bunched beam measurements [76]. Depending on the low cutoff frequency, there is a baseline shift in the BPM signals (Fig. 7.1), which has to be removed for the correct calculation of the bunch offset. After the baseline restoration and normalization (denoted as $\hat{U}$), the sum signal $\hat{U}_\mathrm{u}+\hat{U}_\mathrm{d}$ reflects the longitudinal bunch profile, which is close to a Gaussian distribution in our measurements (Fig. 7.2). The measured value of the peak line density is used for the estimations of the space charge parameter q_sc.

7.2.2 Transverse profile

In SIS18, an Ionization Profile Monitor (IPM) is used for measurements of the transverse beam profile [77, 78]. A particle beam ionizes the residual gas passing through the IPM, where the transverse electric field accelerates ions towards a micro-channel plate (MCP) (Fig. 7.3). After the ion impact, MCP emits electrons that hit a wire array placed behind it. The wire diameter is 1.5 mm and the center-to-center distance is 2.1 mm which defines the resolution of measurements. The data are acquired every 10 ms with the recording time of 0.5 ms. In our measurements, the acquisition time corresponds to about 6000 revolution turns which means that the IPM can not resolve

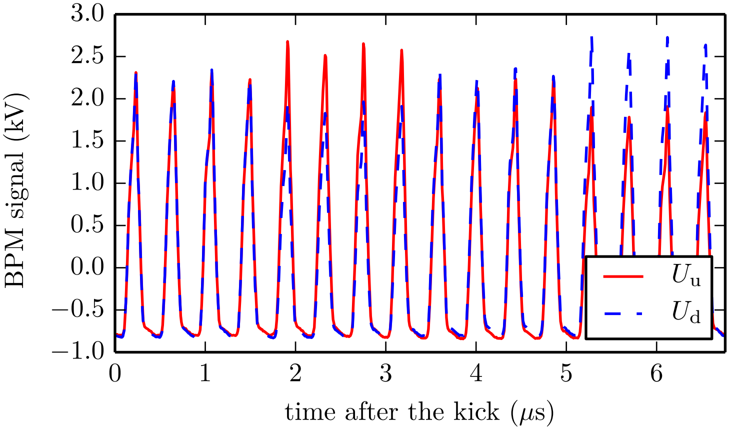

Figure 7.1.: The raw BPM signals of the bunches after the transverse kick in SIS18. The baseline is shifted due to the low frequency cutoff.

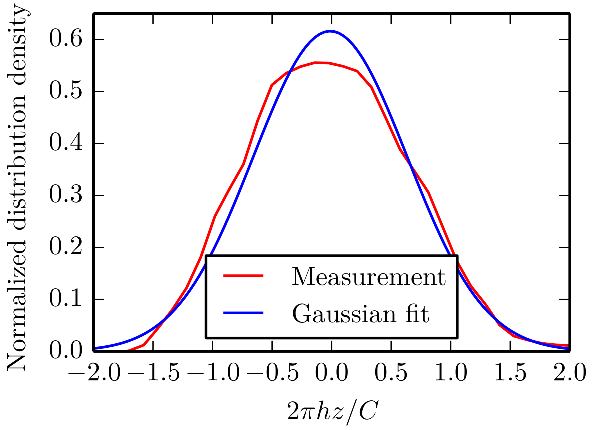

Figure 7.2.: The sum signal from BPM measurements in the vertical plane after the baseline restoration. The estimated rms bunch length is $\sigma_z \approx 5.6$ m.

detailed time evolution of the beam size during the decoherence process. The residual emittance blowup can be observed from the comparison of the beam profiles before and after the kick for the case of a weak space charge and a strong kick (Fig. 7.4).

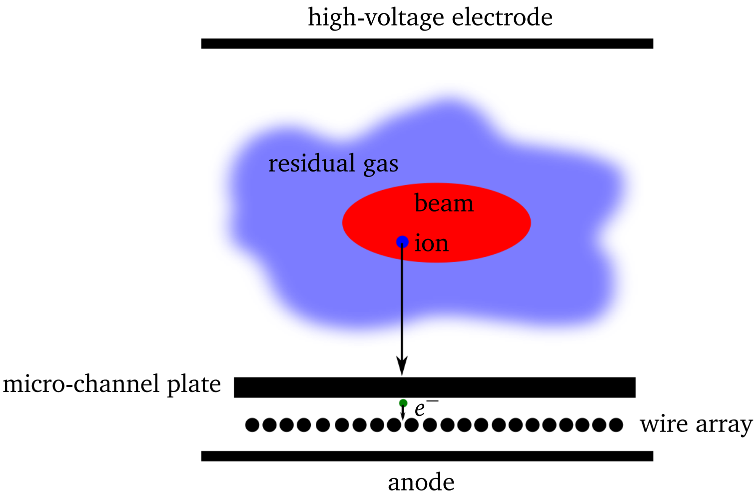

Figure 7.3.: Scheme of the ionization profile monitor operation.

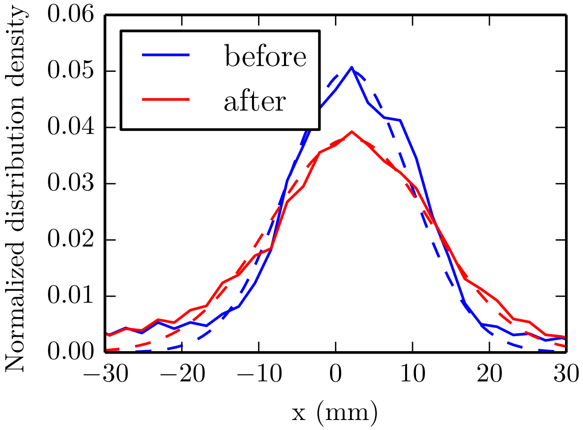

Figure 7.4.: The transverse beam profile in the horizontal plane before and 6000 turns after the transverse kick from measurements in SIS18. The dashed lines are the Gaussian fit. The estimated emittance blowup is $\Delta\epsilon/\epsilon_0 \approx 0.7$.

For the vertical plane, the transverse emittance can be calculated using the value of the vertical beta function at the position of IPM $\beta_{y,\mathrm{IPM}}$,

$$\epsilon_y = \frac{\sigma_y^2}{\beta_{y,\mathrm{IPM}}} \tag{7.5}$$

where the rms beam size in vertical plane σ_y is calculated from the beam profile. For the horizontal plane, the size depends on the momentum spread and the dispersion function. To calculate emittance, this fact has to be taken into account,

$$\epsilon_x = \frac{\sigma_x^2}{\beta_{x,\mathrm{IPM}}} - \frac{D_{x,\mathrm{IPM}}^2}{\beta_{x,\mathrm{IPM}}} \frac{\delta p^2}{p_0^2} \tag{7.6}$$

where $\beta_{y,\mathrm{IPM}}$, and $D_{x,\mathrm{IPM}}$ are the values of the horizontal beta function and the dispersion function at the position of IPM, correspondingly. For the case of short bunches where synchrotron motion is linear, the momentum spread of the beam can be estimated from the bunch length $\delta p/p_0 = 2\pi Q_s \sigma_z/(|\eta| C)$. In our measurements, bunches have the elliptical transverse cross section, which requires us to substitute ϵ in Eq. 2.32 by $(\epsilon_x + \sqrt{\epsilon_x \epsilon_y Q_{0,x}/Q_{0,y}})/2$ for the calculation of the space charge parameter q_{sc}.

7.2.3 Chromaticity measurements

To calculate the effective parameter q_{eff}, we measure the machine chromaticity using a standard method (e.g. in [79]). We shift the beam energy without changing the lattice and measure the change of the revolution frequency and the tune shift using *Schottky diagnostics* [80].

A finite number of particles causes random fluctuations from the uniform distribution which are called *Schottky noise* [81]. The spectrum of the sum signal observed by a Schottky pick-up – referred as the longitudinal Schottky spectrum – contains revolution harmonics

$$\omega_l = l\omega_0, \tag{7.7}$$

where $l \in \mathbb{Z}$. In bunches, the spectral lines split into a series of the synchrotron satellites separated by the frequency ω_s.

In the experiment, we change the bending radius of the dipole magnets. The magnetic field is automatically adapted to keep the constant magnetic rigidity. Then, we accelerate bunches to the energy that corresponds to the initial magnetic field in the dipole magnets. Thus, the beam goes on an off-momentum closed orbit and the energy deviation corresponds to the revolution frequency shift (Eq. 2.17), which can be measured using the longitudinal Schottky spectrum.

Considering the case of the low-intensity beam passing by the Schottky pick-up with zero transverse offset, the spectrum of the delta signal consists of *lower* and *upper Schottky side bands* [80],

$$\omega_l^{\pm} = (l \pm Q_{0,\mathrm{frac}})\,\omega_0. \tag{7.8}$$

where $Q_{0,\mathrm{frac}}$ is the fractional part of the bare tune. For bunches, they are split into synchrotron satellites corresponding to head-tail modes. The measured frequency of the central head-tail mode for both sidebands gives the tune

$$Q_{0,\mathrm{frac}} = l\,\frac{\omega_l^{+} - \omega_l^{-}}{2\omega_l}. \tag{7.9}$$

Plotting the tune shift as a function $\Delta p/p_0$, we fit the line with the slope ξ for the horizontal and the vertical planes (Fig. 7.5). The fitting results are $\xi_x = -1.32$, and $\xi_y = -2.13$, which are consistent with previous measurements [64]. The maximum error of the tune calculation can be estimated as the value of the synchrotron tune $Q_s = 3 \times 10^{-3}$, which means that the relative error is less than 10^{-3}.

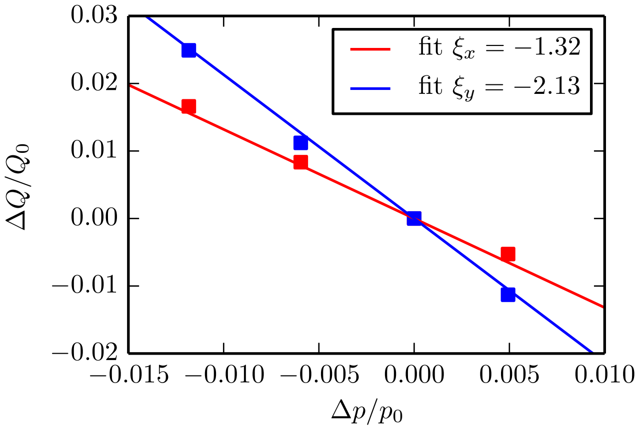

Figure 7.5.: Chromaticity measurements at 100 MeV/u. The red squares are the tune shifts in the vertical plane, the blue squares are the tune shifts in the horizontal plane. The error bars correspond to the marker sizes. The horizontal data point in the origin is hidden by the vertical data point.

7.3 Decisive effects of the decoherence process in experiments

The BPM signals of bunches after the transverse kick have been recorded for different machine and beam settings during the experiments at SIS18 in August 2014. In this section, we show that in our measurements the decoherence process was governed by the interplay of chromaticity and space charge.

From the recorded signals after the baseline restoration, we calculate the turn-by-turn evolution of the horizontal bunch offset as

$$\langle x \rangle_t(N) = \frac{1}{S_x} \frac{\int_{NT_0}^{NT_0+T_0/h} \mathrm{d}t \left[\hat{U}_\mathrm{l}(t) - \hat{U}_\mathrm{r}(t)\right]}{\int_{NT_0}^{NT_0+T_0/h} \mathrm{d}t \left[\hat{U}_\mathrm{l}(t) + \hat{U}_\mathrm{r}(t)\right]} , \tag{7.10}$$

and similarly the vertical bunch offset is

$$\langle y \rangle_t(N) = \frac{1}{S_y} \frac{\int_{NT_0}^{NT_0+T_0/h} \mathrm{d}t \left[\hat{U}_\mathrm{u}(t) - \hat{U}_\mathrm{d}(t)\right]}{\int_{NT_0}^{NT_0+T_0/h} \mathrm{d}t \left[\hat{U}_\mathrm{u}(t) + \hat{U}_\mathrm{d}(t)\right]} , \tag{7.11}$$

where $N = 0$ corresponds to time when the head of the considered bunch arrives to the BPM directly after the transverse kick. We see that decoherence of the bunch offset with space charge is slower than the synchrotron period and the later stage is the beating of the residual head-tail modes (Fig. 7.6). In general, the signals in the vertical plane have higher signal-to-noise ration than the signals in the horizontal plane due to a smaller plate gap. For the natural chromaticity settings in SIS18 $q_{\mathrm{eff},x} \approx q_{\mathrm{eff},y}$. Thus, the difference of decoherence signals for horizontal and vertical planes is because of different space charge strengths in the elliptical beams. To simplify comparison of the decoherence signals for different combinations of the beam and machine parameters, we extract the oscillation amplitude from the calculated bunch offset. In most cases, the decoherence signals for all four bunches are identical.

From the measured signals for the same machine settings, we see a slower decoherence for the beam with a higher intensity (Fig. 7.7). This is in agreement with the analytical expectations discussed in Chap. 4. To demonstrate the role of chromaticity, we compare decoherence for the same beam parameters for the natural ($\xi_x = -1.3$, $q_\mathrm{eff} = 1.3$) and the compensated ($\xi_x \approx 0$, $q_\mathrm{eff} = 0.5$) chromaticity (Fig. 7.8). Decoherence is slower for a smaller effective parameter q_eff similarly to the case without space charge.

The possible contribution of the transverse nonlinearities can be clarified by the comparison of the decoherence for the normal and for the distorted closed orbit (the maximum distortion is about 10 mm). The closed orbit is calculated by averaging BPM data over large number of turns (a few 100000 turns). The initial stage does not differ and the residual oscillations have similar amplitudes (Fig. 7.9).

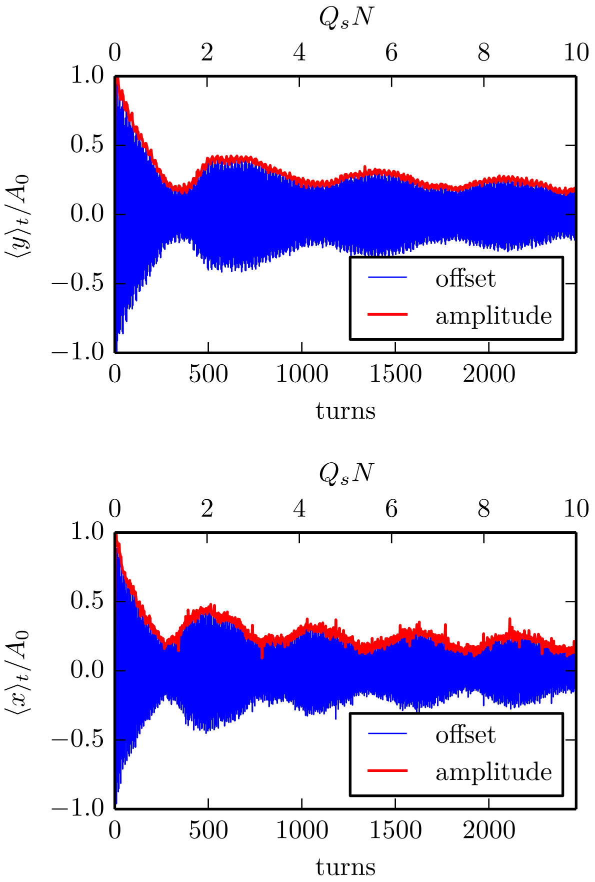

Figure 7.6.: Time evolution of the bunch offset in the vertical plane (the top plot) and the horizontal plane (the bottom plot) from BPM measurements at SIS18 after a transverse kick calculated by Eq. 7.11 and Eq. 7.10, respectively. One turn corresponds to 1.7μ and the kick results in the initial offset $A_0 \approx 4$ mm that is similar for both planes.

According to analytical predictions (Sec. 4.3) and simulation scans (Sec. 6.4), image charges can change the initial stage of decoherence process for $q_{\text{ic}} > 0.5$. We estimate the maximum value of the parameter q_{ic} from the beam parameters and the average radii of the SIS18 beam pipe for the horizontal and the vertical planes: $b_x = 100$ mm

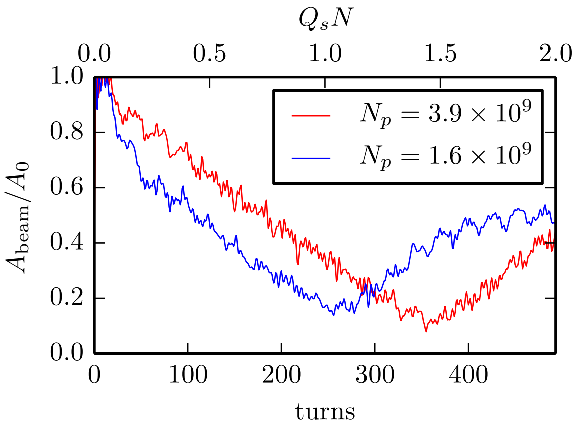

Figure 7.7.: Comparison of the vertical decoherence for the same machine settings and different intensities from the measurements in SIS18. The estimated space charge parameters: $q_{\rm sc} \approx 5$ (the red line), and $q_{\rm sc} \approx 2$ (the blue line).

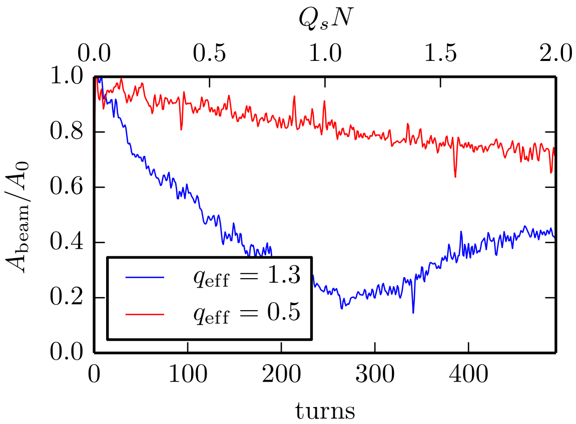

Figure 7.8.: The horizontal decoherence with space charge from measurements in SIS18: the blue line is for the natural chromaticity ($\xi_x = -1.3$), the red line is for the compensated chromaticity ($\xi_x \approx 0$).

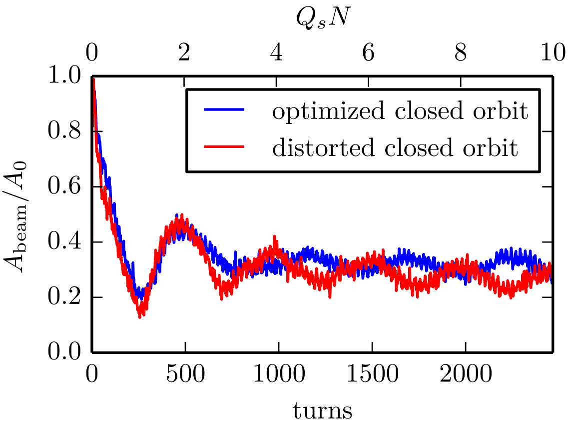

Figure 7.9.: The vertical decoherence with space charge from measurements in SIS18 for different closed orbit.

gives $q_{\mathrm{ic},x} = 0.05$, and $b_y = 70$ mm gives $q_{\mathrm{ic},y} = 0.15$. We conclude that image charges can be neglected for our observations.

Decoherence can be also modified by rf nonlinearities depending on the bunch length which is especially important for the later stage of decoherence and recoherence processes [33]. According to simulation results discussed in Sec. 6.5, rf nonlinearities can be neglected for the initial stage of decoherence process. Only the recoherence process and the further beating of head-tail modes are affected.

7.4 Experimental results and comparisons with simulations

In the previous section, we showed that the initial stage of the decoherence process in our measurements was governed by chromaticity and space charge. This means that simulations that include space charge and chromaticity kicks should be sufficient to reproduced the obtained experimental results. This can be done within the first synchrotron period, but the later stage of decoherence and recoherence processes is defined by interplay of different effects discussed above.

Performing simulations with the input beam parameters estimated from the measurements, we see that the decoherence process in simulations is faster than the decoherence process in measurements (Fig. 7.10). This indicates that q_{sc} is underestimated because the parameter q_{eff} can be accurately calculated from the momentum spread and chromaticity. We argue that the observed difference is due to the uncertainty in the transverse beam size measurements at SIS18 which was also the case in previous works [55, 33]. To prove this, we take the results of simulation scans for q_{eff} estimated

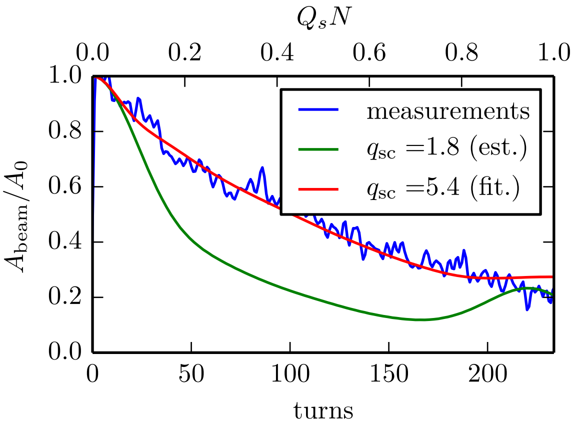

Figure 7.10.: Example of fitting of simulations to the measurements. The estimated parameters from measurements: $q_{\text{sc}} = 1.8$, $q_{\text{eff}} = 1.3$. The green line is from simulations with the estimated q_{sc}.

from measurements and different q_{sc}, and fit the time evolution of the bunch offset amplitude with a free parameter q_{sc} (Fig. 7.10).

Simulations reproduce decoherence for the natural and the compensated chromaticity (Fig. 7.11). Here we also see that if the condition $q_{\text{sc}} \gg q_{\text{eff}}$ is fulfilled, the oscillation amplitude practically does not decrease during the first synchrotron period due to the loss of decoherence.

In simulations, we set $A_0 = \sigma_0$ which corresponds to the case when the decoherence does not depend on the initial kick (see Fig. 6.11). This agrees with measurements where we also observed a weak dependence of decoherence on the kick strength (Fig. 7.12). Only for the strongest kick (the black line) decoherence is a bit faster. This can be related to the losses which are observed for the case of large initial offsets (Fig. 7.13). In our measurements, the number of lost particles depends on space charge and the kick strength which can be due to a resonance excitation of particles discussed in Sec. 6.2. A detailed comparison of the particle losses in simulations and measurements can be as subject of a dedicated study which is not covered in this work.

We verify the systematic behavior of the decoherence with space charge by comparing of the decoherence time (Fig. 7.14). The different combination of parameters q_{sc} and q_{eff} is obtained by varying the beam intensity and the bunch length. The measured decoherence time agrees very good with the decoherence time obtained from simulations. As expected, for larger space change parameter the decoherence process is slower. We observed also that the decoherence time approaches the synchrotron period for $q_{\text{sc}} = 9$ and q_{eff}. For higher effective parameter q_{eff}, we observe a faster decoherence.

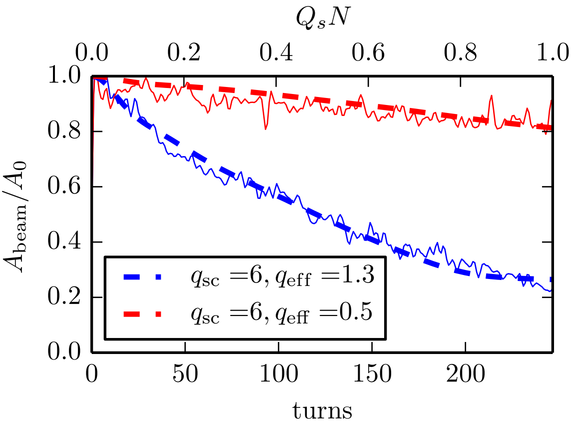

Figure 7.11.: Decoherence for the fixed beam parameters and different chromaticity settings from measurements in SIS18: the solid blue line for the natural chromaticity ($\xi_x = -1.3$, $q_{\mathrm{eff}} = 1.3$), the solid red line the compensated chromaticity ($\xi_x \approx 0$, $q_{\mathrm{eff}} = 0.5$). The dashed lines are from simulations with the fitted q_{sc}.

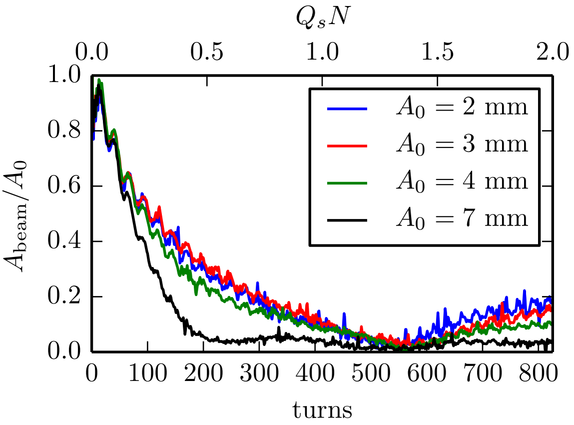

Figure 7.12.: Decoherence with space charge from measurements in SIS18 for different kick strength that correspond to different value of the initial amplitude A_0. The estimated parameters: $q_{\mathrm{sc}} = 9$ (fit), $q_{\mathrm{eff}} = 1.8$, and $Q_s = 2.4 \times 10^{-3}$.

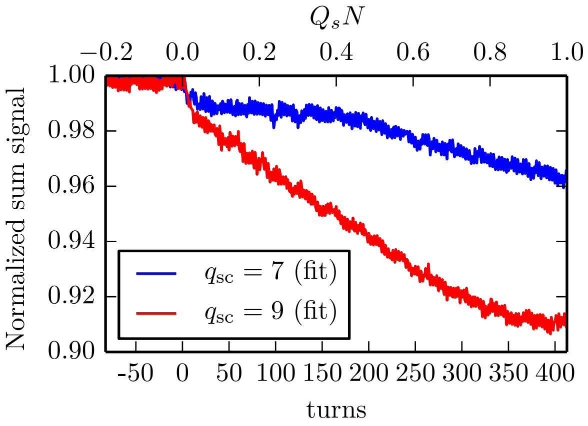

Figure 7.13.: Example of the time evolution of the sum BPM signal from the vertical plates normalized by the value before the kick for different intensities. Approximately 10% of the particles are lost during the first synchrotron period for $q_{\mathrm{sc}} = 9$ (fit). The estimated parameters: $q_{\mathrm{eff}} = 1.8$, $A_0 = 7\mathrm{mm}$, and $Q_s = 2.4 \times 10^{-3}$.

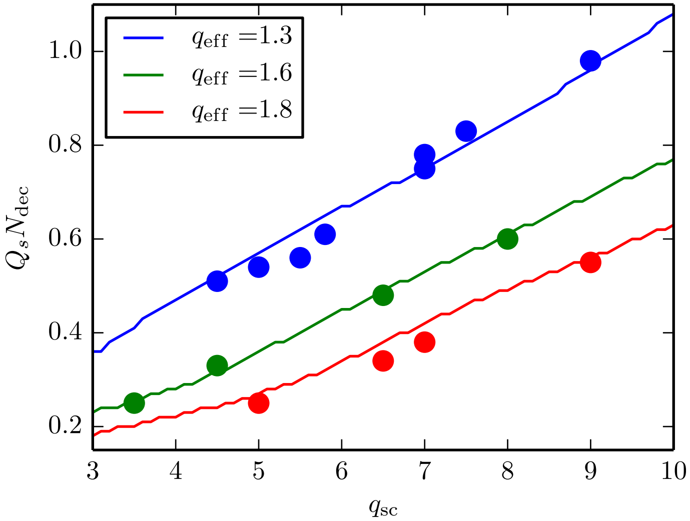

Figure 7.14.: Summary of the decoherence measurements in SIS18. The points correspond to the decoherence time obtained from the measured signals for different combinations of machine and beam parameters. Lines are the characteristic decoherence time from simulations for $A_0 = \sigma_0$.

8 Transverse feedback systems

In previous chapters, we discussed decoherence and emittance blowup in ion beams for different combination of space charge, chromaticity, and image charges. To preserve the beam quality, transverse feedback systems can be used. In this chapter, we start with a short description of basic principles of transverse feedback systems (TFS) (Sec. 8.1). For the optimal parameters TFS should damp bunch oscillations after the initial offset and prevent the emittance blowup. The efficiency of TFS can be reduced by the limited bandwidth, time delay errors, and noise. The simulation model of a realistic digital TFS implemented in the PATRIC code is described in Sec. 8.2. Simulation results for damping of the injection errors are presented Sec. 8.3.

8.1 Basics of a transverse feedback system

To damp beam oscillations after the injection error, the detected BPM signals are processed and transmitted to a kicker. The correction signal should be applied to the same part of the beam that generated the pick-up signals. This can be obtained by the proper delay which in some cases corresponds to several revolution turns. Following [82], we consider a simplified situation when the beam passes through the pick-up with the maximum transverse offset. If the phase advance between the pick-up and the kicker is $\Delta\Psi_{\mathrm{P-K}} = \pi/2$, the correction kick proportional to the measured displacement causes the change of the beam trajectory in the transverse phase space (Fig. 8.1). After one turn the amplitude of oscillations is corrected by

$$\Delta x = -gx, \tag{8.1}$$

where g is the feedback gain. Using a smooth approximation for the kick one can write a differential equation

$$\frac{\mathrm{d}x}{\mathrm{d}N} = -gx, \tag{8.2}$$

which corresponds to a damping with the characteristic time $1/g$ expressed in turns. Taking into account that the beam passes by BPM with different betatron phase, we get an additional factor $1/2$ for the damping time due to TFS

$$N_{\mathrm{damp}} = \frac{2}{g}. \tag{8.3}$$

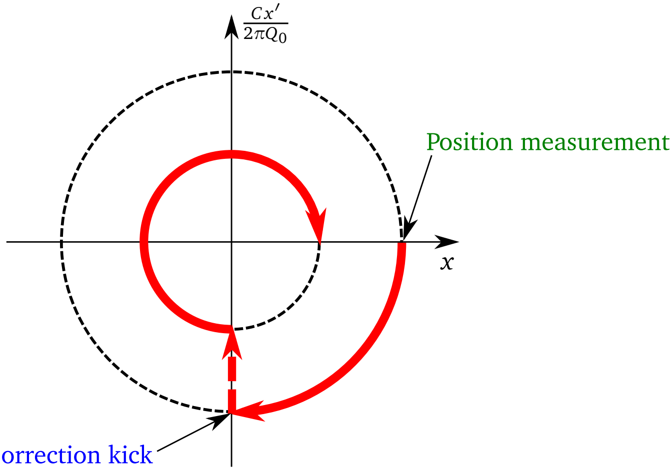

Figure 8.1.: The bunch trajectory in the normalized phase space.

For the case $\Delta\Psi_{\text{P–K}} \neq \pi/2$, to apply the correction kick, we combine the beam offsets of two consecutive turns (x_N and x_{N+1}) as

$$\Delta x'_{\text{CK},N+1} = \frac{g2\pi Q_0}{C}(\kappa_1 x_{N+1} + \kappa_2 x_N). \tag{8.4}$$

To obtain correction coefficients κ_1 and κ_2, we express coordinates of the beam at the position of the kicker $(x,x')^{\text{T}}_{\text{K},N+1}$ via the beam coordinates at the positions of the pick-up $(x,x')^{\text{T}}_{\text{P},N+1}$ and $(x,x')^{\text{T}}_{\text{P},N}$ using transfer matrices from Eq. 2.20. Then we rewrite $x'_{\text{K},N+1}$ using $x_{\text{P},N+1}$, $x_{\text{P},N}$, multiply by a factor $-g2\pi Q_0/C$, and we get

$$\begin{aligned}\kappa_1 &= -\frac{\cos(2\pi Q_0(N_{\text{wait}}+1) + \Delta\Psi_{\text{P–K}})}{\sin(2\pi Q_0)},\\ \kappa_2 &= \frac{\cos(2\pi Q_0 N_{\text{wait}} + \Delta\Psi_{\text{P–K}})}{\sin(2\pi Q_0)}.\end{aligned} \tag{8.5}$$

Here, N_{wait} is the number of *waiting* turns for which the correction kick is postponed.

Analytical estimations of the emittance blowup in the presence of active damping are discussed in Ref. [83]. In case of an ideal TFS, the emittance growth is

$$\frac{\Delta\epsilon_{\text{TFS}}}{\epsilon_0} = \frac{1}{2}\frac{A_0^2}{\sigma_0^2}\left(\frac{1}{1+N_{\text{dec}}/N_{\text{damp}}}\right)^2. \tag{8.6}$$

This equation was derived in assumption of $N_{\mathrm{damp}} \ll N_{\mathrm{dec}}$ and an exponential decay of the oscillation amplitude due to decoherence $A(N) = A_0 \exp(-N/N_{\mathrm{dec}})$. To preserve beam quality, the active damping should be faster than the characteristic decoherence time. Below we describe the simulation model that includes the TFS imperfections. It is used for study of the TFS efficiency for damping of oscillations after injection errors.

8.2 TFS simulation model in PATRIC

In this work, we developed and implemented a TFS model in the PATRIC code (Fig. 8.2). During the first turn, macro-particles are kicked at the fixed position passing through the excitation kicker. For simplicity the kick is applied at the position where the BPM signals will be generated. Then, calculation of the pick-up signals, TFS signal processing, and the kicker are included to the self-consistent particle tracking described in Chap. 5.

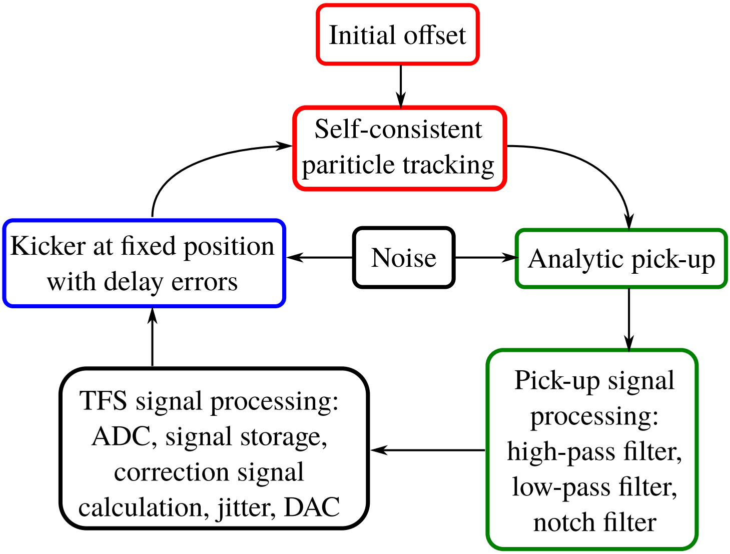

Figure 8.2.: Flowchart of the self-consistent particle tracking simulations with a transverse feedback system.

8.2.1 Pick-up signal processing

To model the analog BPM signals, we use the following method. At the beginning of the turn, we interpolate particles on two longitudinal grids with weights x and x', correspondingly. Using the grids with high resolution that expressed by N_z (the number of points per turn), we get the longitudinal distributions of the dipole moments $d_x(z)$ and $d_{x'}(z)$. To get the normalized delta signal at the pick-up u_N at the turn N, we use the combination

$$u_N[i] = d_x\left[\frac{C}{2} - \frac{iC}{N_z}\right]\cos\left(\frac{2\pi Q_0 i}{N_z}\right) + d_{x'}\left[\frac{C}{2} - \frac{iC}{N_z}\right]\sin\left(\frac{2\pi Q_0 i}{N_z}\right)\frac{C}{2\pi Q_0}, \tag{8.7}$$

which is similar to the matrix translation of the coordinates to the position of the pick-up placed at $s = C/2$ (Fig. 8.3). Here $i \in [0, N_z - 1]$ is the index that corresponds to a sample of the quasi-analog signal.

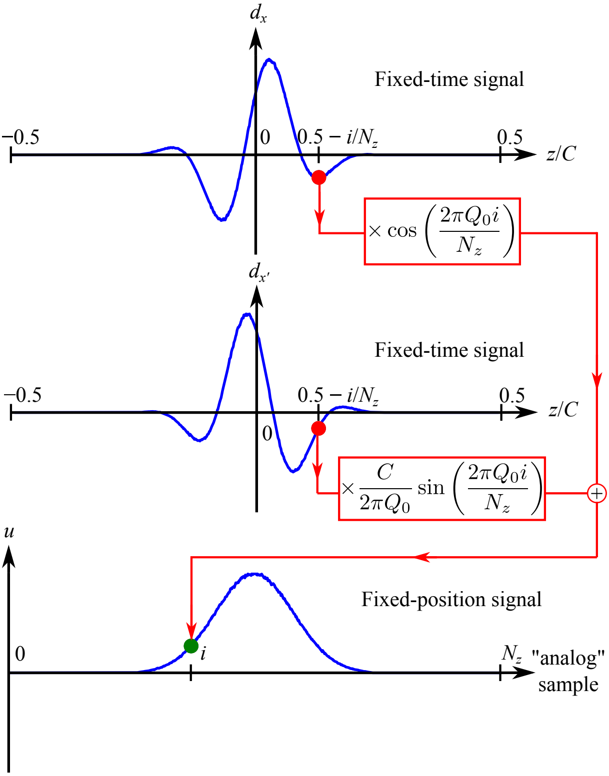

Figure 8.3.: Analytical calculation of the pickup signal at turn N. To obtain the normalized delta pick-up signal u, the values of the dipole moments $d_x(z)$ and $d_{x'}(z)$ are combined with the proper coefficients.

In TFS, notch filters or closed orbit suppressors are used to remove the revolution frequency harmonics from the pick-up signals [84, 85]. Without filtering, the offset of the closed orbit in the pick-up causes the change of the overall closed orbit in the machine, depending on g, and can result in a saturation of the kicker amplifiers. The notch filter can be implemented as the difference between the signals obtained by successive turns,

$$u_{\mathrm{out},N}[i] = u_{\mathrm{in},N}[i] - u_{\mathrm{in},N-1}[i]. \tag{8.8}$$

where $u_{\mathrm{out},N}$ and $u_{\mathrm{in},N}$ are the output and input signals at the turn N, correspondingly. Such filters remove information about the longitudinal profile of the beam which means that the sum signal can not be transmitted through the TFS signal processing unit.

To model a bandwidth limited system, we use a cascade of the first order high-pass (HPF) and low-pass filters (LPF) after the notch filter. They can be implemented by recurrence relations

$$u_{\mathrm{out},N}[i] = \kappa_{\mathrm{HPF}} u_{\mathrm{out},N}[i-1] + \kappa_{\mathrm{HPF}}(u_{\mathrm{in},N}[i] - u_{\mathrm{in},N}[i-1]), \tag{8.9}$$

$$u_{\mathrm{out},N}[i] = (1-\kappa_{\mathrm{LPF}}) u_{\mathrm{out},N}[i-1] + \kappa_{\mathrm{LPF}} u_{\mathrm{in},N}[i]. \tag{8.10}$$

Here the coefficient for the high-pass filter

$$\kappa_{\mathrm{HPF}} = \left\{ 2\pi \frac{Q_{\mathrm{L}}}{N_z} + 1 \right\}^{-1}, \tag{8.11}$$

is defined by a low cutoff frequency Q_{L} normalized by the revolution frequency. Similarly, for the low-pass filter we have

$$\kappa_{\mathrm{LPF}} = \left\{ \frac{1}{2\pi} \frac{N_z}{Q_{\mathrm{H}}} + 1 \right\}^{-1}, \tag{8.12}$$

where Q_{H} is a high cutoff frequency normalized by the revolution frequency.

8.2.2 TFS signal processing

An analog signal from the pick-up has to be sampled for the digital signal processing using analog-to-digital converter (ADC). In PATRIC, a quasi-analog delta signal with the high time resolution N_z is sampled with a lower frequency. We consider that the high cutoff frequency Q_{H} is defined by the sampling rate, and the number of samples per turn is

$$N_{\mathrm{SAMP}} = 2Q_{\mathrm{H}} = \frac{N_z}{N_{\mathrm{TS}}}, \tag{8.13}$$

where N_{TS} is the number of time samples corresponding to a single digital sample. Depending on the number of waiting turns, $N_{\mathrm{wait}} + 1$ sampled signals are stored. The signals of two last consecutive tuns are combined in the correction signal using Eq. 8.4. In the presence of the notch filter, the phase advance in Eq. 8.5 should be substituted by

$$\Delta\Psi_{\mathrm{P-K}} \leftarrow \Delta\Psi_{\mathrm{P-K}} + \pi Q_0 - \frac{\pi}{2}, \tag{8.14}$$

and the coefficients κ_1, κ_2 should be divided by the factor $2\sin(\pi Q_0)$.

As we discussed in Subsec. 8.2.1, the sum signal from the pick-up is suppressed by the notch filter. It means that the correction signal is proportional to the dipole moment of the $d_{x'}$ at the position of the kicker but not to the local offset of x'. In our simulations, the delta pick-up signals are normalized by the maximum line density of the bunch. Thus, the processed signal in the bunch center reflects the local offset.

To model time delay errors, we consider the contribution of the constant delay Δz_{CD}, and the random delay due to a jitter. The latter can change the duration of the signal corresponding to a single digital sample when it is transmitted to the digital-to-analog converter (DAC). We implement a jitter as a random variation of the sample length $N_{\mathrm{TS}} + \delta N_{\mathrm{RD}}$, where the delay amplitude δN_{RD} is generated according to a Gaussian distribution. Then, the correction signal passes through DAC which is modeled as the low-pass filter with the cutoff frequency Q_{H} (Eq. 8.13).

The combination of low-pass filters in the pick-up signal processing and DAC produces a time delay and a deformation of the signal shape (Fig. 8.4). The resulting time delay is about $\Delta z_{\mathrm{CD}} = C/N_{\mathrm{SAMP}}$ which is taken into account in the simulation scans.

8.2.3 TFS kicker and noise

The analytical pick-up described in Subsec. 8.2.1 is used for calculation of the correction signal at the beginning of the turn. The kicker placed at the fixed position applies the correction signal each simulation step. The kick strength is interpolated according to the longitudinal position of the particle that passes through the kicker taking into account the constant delay.

White noise in the TFS model is applied at two stages of the feedback loop: after the calculation of the delta pick-up signal and after the TFS signal processing. We quantify the noise amplitude A_{noise} expressed in meters, which for the pick-up corresponds to a set of random values in the range $[-1, 1]$ multiplied by $A_{\mathrm{noise}}\lambda_0$. For the kicker signal, the multiplication factor is $A_{\mathrm{noise}} 2\pi Q_0/C$.

8.3 Simulations with TFS

In this section, we discuss the role of different types of TFS imperfections. Starting with the low-intensity case we find that system bandwidth, constant delay errors, and noise could significantly reduce the TFS efficiency. The input parameters used in simulation scans are summarized in Tab. 8.1. They correspond to the characteristic decoherence time $N_{\mathrm{dec0}} \approx 56$ turns and the damping time $N_{\mathrm{damp}} = 60$ turns.

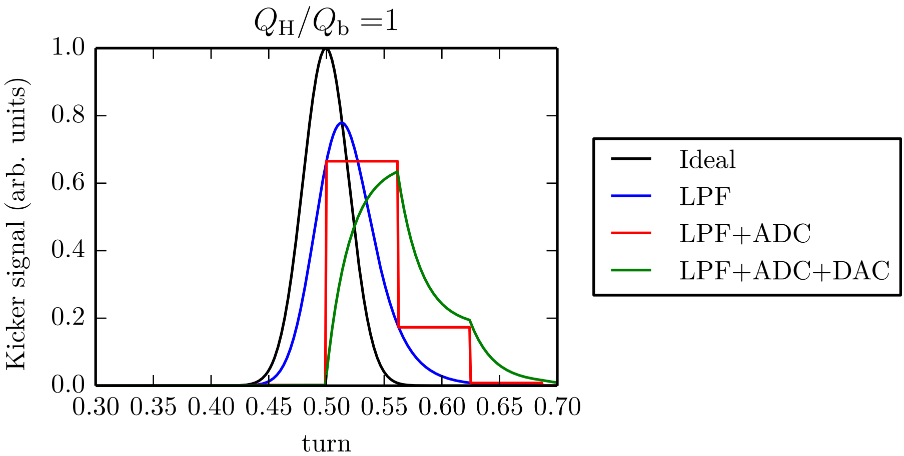

Figure 8.4.: Example of deformation of the correction signal due the combination of the low-pass filters from the pick-up signal processing and DAC. The signal is generated for a bunch with the constant local offset and a Gaussian longitudinal profile.

Simulation parameter	Symbol	Value
Horizontal tune	$Q_{0,x}$	4.29
Vertical tune	$Q_{0,y}$	3.27
Effective spread	q_eff	1
Synchrotron tune	Q_s	4×10^{-3}
TFS gain	g	0.033
Circumference	C	216 m
Rms bunch length	σ_z	$\approx$ 4.3 m

Table 8.1.: Parameters used for simulations with the TFS damping.

8.3.1 Limited bandwidth and sampling rate

We expect a reduction of the TFS efficiency when the bunch spectrum is not covered by the system bandwidth. Turn-by-turn bunch spectrum without intensity effects can be calculated from the local bunch offset given by Eq. 3.13. The position of the maximum in the spectrum can be estimated as

$$Q_{\mathrm{ib}}(N) = \frac{C q_{\mathrm{eff}}}{2\pi\sigma_z}(1 - \cos(2\pi Q_s N)) = Q_{\mathrm{b}} q_{\mathrm{eff}}(1 - \cos(2\pi Q_s N)), \tag{8.15}$$

where the characteristic bunch frequency is

$$Q_{\mathrm{b}} = \frac{C}{2\pi\sigma_z}. \tag{8.16}$$

Both frequencies are normalized by the revolution frequency. The time evolution of the intrabunch spectrum calculated as Fourier transform of the local bunch offset (Eq. 3.13) is shown in Fig. 8.5. The spectrum is moving toward the higher frequencies for $N < N_s/2$ and then returns back to the origin.

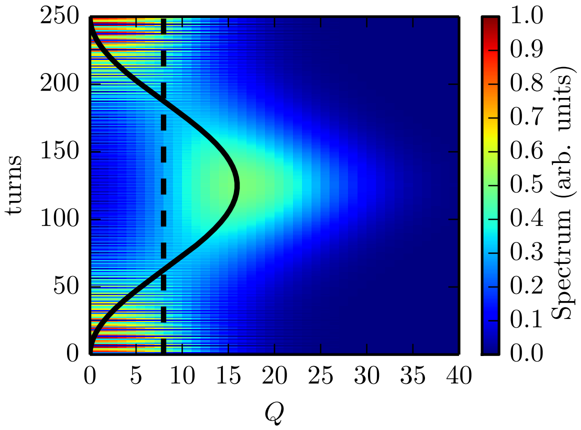

Figure 8.5.: Turn-by-turn bunch spectrum given by Fourier transform of the local bunch offset (Eq. 3.13) for $q_{\mathrm{eff}} = 1$ and $Q_{\mathrm{b}} = 8$. The solid black line is given by Eq. 8.15, and the dashed black line is given by Eq. 8.16.

High frequency cutoff

The role of the high cutoff frequency is presented in the simulation scan for $Q_{\mathrm{L}} = 0$, different Q_{H}, and the corresponding sampling rate $N_{\mathrm{SAMP}} = 2Q_{\mathrm{H}}$ (Fig. 8.6). A TFS with a high sampling rate can damp beam oscillations and prevent the emittance blowup. The TFS efficiency can be strongly reduced for $Q_{\mathrm{H}} < 2Q_{\mathrm{b}}q_{\mathrm{eff}}$ (the solid line). In this case, intrabunch oscillations can not be sufficiently resolved due to a low sampling rate.

When the high cutoff frequency is below the characteristic bunch frequency ($Q_\mathrm{H} < Q_\mathrm{b}$), only one sample per bunch can be used for the calculation of the correction signal.

Low frequency cutoff

To study the impact of the low cutoff frequency, we performed simulation scan for a TFS with a high sampling rate ($Q_\mathrm{H} = 512$) and different Q_L. In general, a higher value of Q_L results in a slower damping (Fig. 8.7). There are three characteristic ranges of frequencies with different TFS performance. The transverse oscillations can be damped and the transverse emittance can be preserved within the first synchrotron period for $Q_\mathrm{L} < Q_\mathrm{b}$ (the dashed white line). In this case, the damping is maintained by significant contribution of high-frequency intrabunch oscillations to the correction signal. The TFS efficiency can be strongly reduced for $Q_\mathrm{L} > 2Q_\mathrm{b}q_\mathrm{eff}$ (the solid line). The frequencies of the intrabunch oscillations are significantly suppressed by the high-pass filter. In the intermediate region, the damping is still possible within two synchrotron periods.

8.3.2 Delay errors

Starting with the random delay errors, we consider the case where TFS bandwidth does not limit damping efficiency ($Q_\mathrm{H} = 128$ and $Q_\mathrm{L} = 0$). For $N_z = 1024$ and $N_\mathrm{SAMP} = 256$, we performed scan for $\delta N_\mathrm{RD} \in [0, N_\mathrm{TS}]$. The results show a minor effect from random delay errors (Fig. 8.8). This can be understood by the fact that the bunch spectrum does not contain such high frequencies given short random delay errors.

In the previous section we showed that without space charge TFS can damp initial oscillations and can prevent the emittance blowup if the system bandwidth covers the full spectrum of the intrabunch oscillations. To examine the contribution of the constant delay error Δz_CD, we consider a TFS with a broad bandwidth $Q_\mathrm{L} = 0$ and $Q_\mathrm{H} = 512$. The simulation scan for $\Delta z_\mathrm{CD} \in [-\sigma_z, \sigma_z]$ is presented in Fig. 8.9. Small delay errors do not affect the TFS efficiency. For $\Delta z_\mathrm{CD}/\sigma_z \approx \pm 1/2q_\mathrm{eff}$ (the black lines), the TFS makes beam unstable which leads to a strong emittance blowup. As the kick is proportional to the dipole moment $d_{x'}$, the effect of anti-damping is significant when the central part of the bunch experience the strong kick. For longer delays ($\Delta z_\mathrm{CD}/\sigma_z > 1$), the bunch is kicked by a weak correction signal and damping is negligible. In this case, we observe the decoherence process and the following recoherence process.

8.3.3 Contribution of noise

As we discussed in Sec. 8.2, white noise is applied at two stages of the feedback loop and characterized by the amplitude A_noise. Here we discuss simulations for A_noise linearly proportional to the TFS gain. To clarify the contribution of the noise in TFS, we performed a simulation scan (Fig. 8.10) for the following parameters: $Q_\mathrm{L} = 0$, $Q_\mathrm{H} = 512$, $\Delta z_\mathrm{CD} = 0$, $\delta N_\mathrm{RD} = 0$, and $A_\mathrm{noise}/A_0 \in [0.02, 0.25]$.

A TFS with a large gain results in a fast reduction of the oscillation amplitude and suppresses recoherence. The strong noise leads to a fast emittance blowup during the

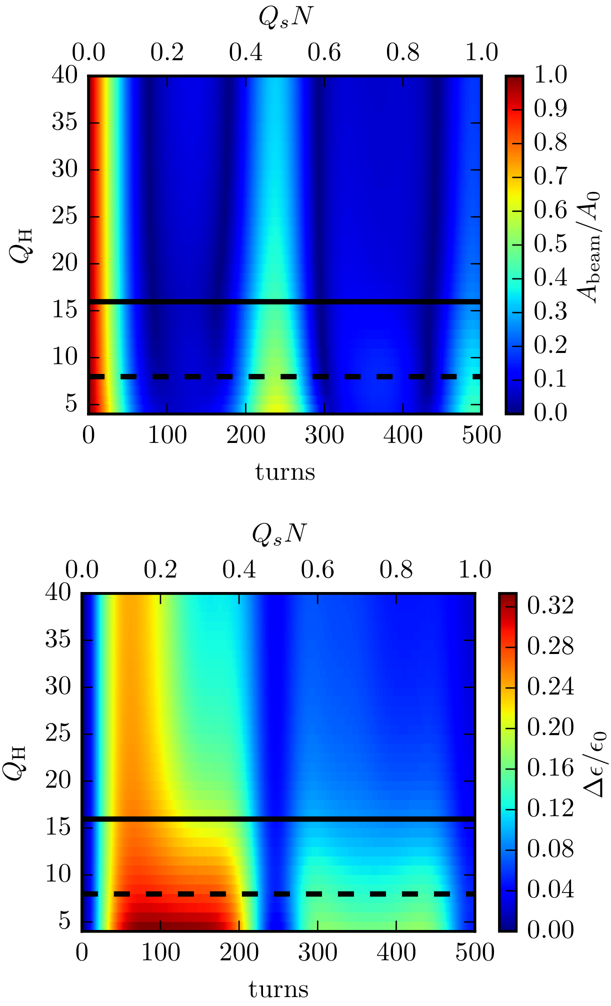

Figure 8.6.: Damping of coherent oscillations after the initial offset using TFS for different high cutoff frequencies. The top plot is the time evolution of the offset amplitude, and the bottom plot is the time evolution of the emittance blowup. The lowest high cutoff frequency is $Q_\mathrm{H} = 4$. The solid black lines are $Q_\mathrm{H} = 2q_\mathrm{eff}Q_\mathrm{b}$, and the dashed black lines are $Q_\mathrm{H} = Q_\mathrm{b}$. Simulation parameters are $q_\mathrm{sc} = 0$, $q_\mathrm{ic} = 0$, $q_\mathrm{eff} = 1$, $Q_\mathrm{b} = 8$, $Q_s = 4 \times 10^{-3}$, $Q_\mathrm{L} = 0$, and $N_\mathrm{damp} = 60$.

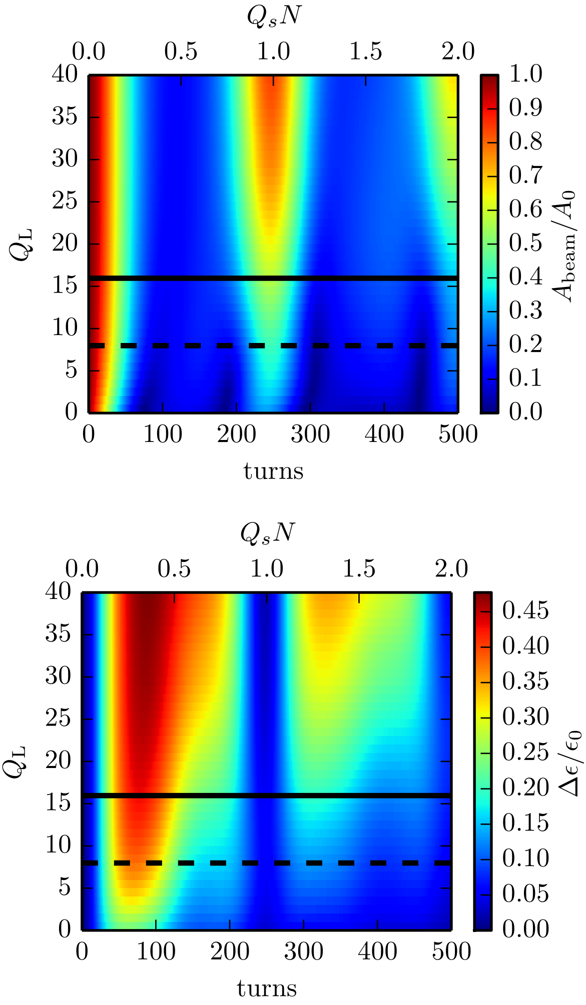

Figure 8.7.: Damping of coherent oscillations after the initial offset using TFS with different low cutoff frequency. The top plot is the time evolution of offset amplitude, and the bottom plot is the time evolution of the emittance blowup. The solid black lines are $Q_L = 2q_{\text{eff}}Q_b$, and the dashed black lines are $Q_L = Q_b$. Simulation parameters are $q_{\text{sc}} = 0$, $q_{\text{ic}} = 0$, $q_{\text{eff}} = 1$, $Q_b = 8$, $Q_s = 4 \times 10^{-3}$, $Q_H = 512$, and $N_{\text{damp}} = 60$.

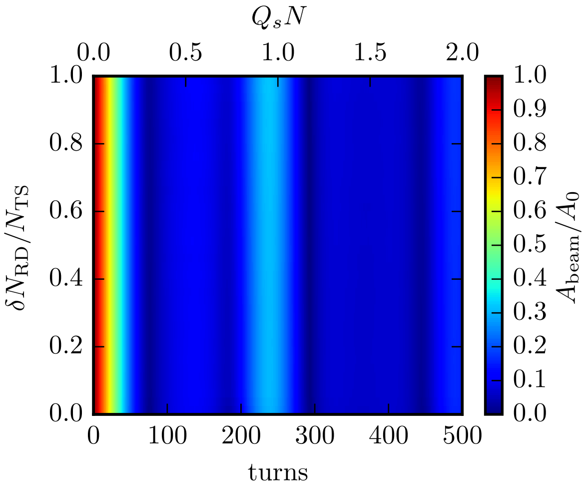

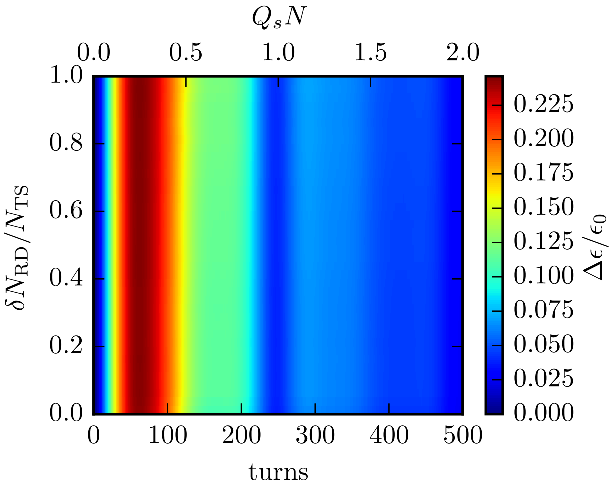

Figure 8.8.: Damping of coherent oscillations after the initial offset using TFS with different amplitudes of jitter. The top plot is the time evolution of offset amplitude, and the bottom plot is the time evolution of the emittance blowup. Simulation parameters are $q_{\mathrm{sc}} = 0$, $q_{\mathrm{ic}} = 0$, $q_{\mathrm{eff}} = 1$, $Q_{\mathrm{b}} = 8$, $Q_s = 4 \times 10^{-3}$, $Q_{\mathrm{L}} = 0$, $Q_{\mathrm{H}} = 128$, $N_{\mathrm{damp}} = 60$, and $N_z = 1024$.

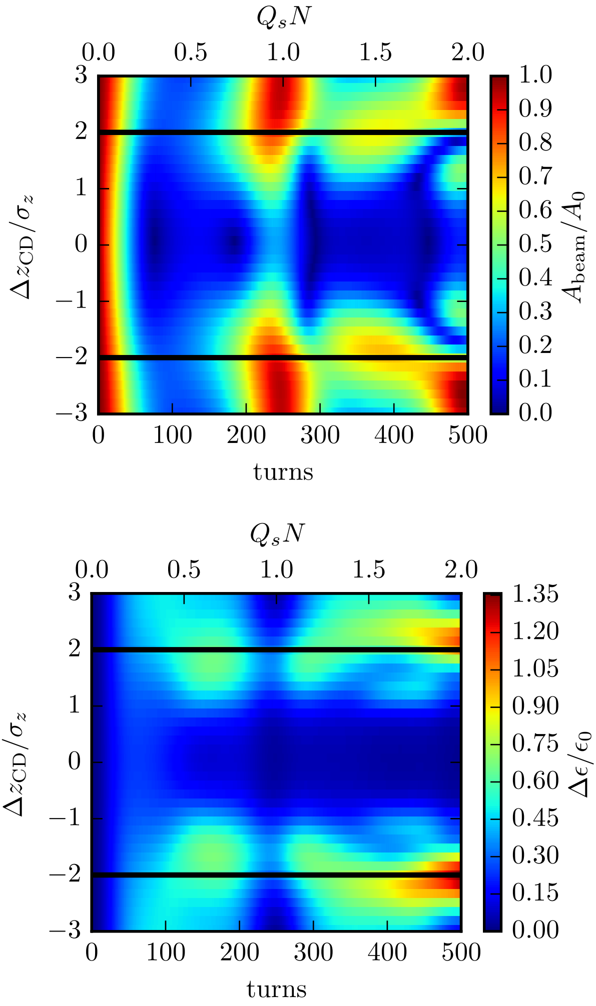

Figure 8.9.: Damping of coherent oscillations after the initial offset using TFS with different constant delays. The top plot is the time evolution of offset amplitude, and the bottom plot is the time evolution of the emittance blowup. The solid black lines are $\Delta z_{\rm CD}/\sigma_z = \pm 1/2q_{\rm eff}$. Simulation parameters are $q_{\rm sc} = 0$, $q_{\rm ic} = 0$, $q_{\rm eff} = 1$, $Q_{\rm b} = 8$, $Q_s = 4 \times 10^{-3}$, $Q_{\rm H} = 512$, $N_{\rm damp} = 60$, and $N_z = 1024$.

damping of the transverse oscillations. Then, the noise in the TFS contributes to the further emittance blowup.

For the TFS with a small gain ($N_{\mathrm{damp}} \approx N_{\mathrm{dec}}$), the amplitude of the beam oscillations reduces due to interplay of the TFS and decoherence. This results in an initial emittance blowup that reaches a maximum at $N \approx N_{\mathrm{dec0}}$ (the black vertical line in Fig. 8.10). The TFS with a high sampling rate can reduce this emittance blowup by further damping of intrabunch oscillations for $q_{\mathrm{eff}} = 1$. The contribution of noise is negligible in this case.

The initial emittance blowup due to decoherence and the TFS is small in the intermediate region. The TFS can not effectively damp the intrabunch oscillations due to the contribution of the noise in this case.

8.3.4 Role of space charge and image charges

According to the analytical model and the simulation study discussed in Chap. 4 and Chap. 6, space charge slows down the decoherence process which require a smaller TFS gain to damp the injection error and preserve the beam quality. We compare the simulation scan for different high cutoff frequencies shown in Fig. 8.6 with a similar scan in the presence of the moderate space charge and weak image charges (Fig. 8.11). A TFS with a high sampling rate can sufficiently damp oscillations following by the injection error or the initial kick and prevent the emittance blowup. The TFS efficiency is reduced for $Q_{\mathrm{H}} < Q_{\mathrm{b}}$, similarly to the case without space charge. The intrabunch oscillations, which are partly suppressed by space charge, are affected by contribution of image charges. This results in a characteristic range of high cutoff frequencies where the TFS efficiency is still limited (in this example the $Q_{\mathrm{H}} < q_{\mathrm{eff}} Q_{\mathrm{b}}$). For even stronger image charges ($q_{\mathrm{ic}} > 1$) decoherence can be faster than the synchrotron period and the coherent tune spread enchances intrabunch oscillations. To maintain damping, the high cutoff frequency of the TFS should be increased.

In the presence of space charge and image charges, a beam can also be unstable for particular values of the time delay errors (Fig. 8.12). The unstable regions are not symmetric in contrast to the case without intensity effect (Fig. 8.9). This can be understood form the asymmetry of the local bunch offset observed in simulations with space charge and image charges (Fig. 8.13). The local offset is affected by the resonance particle excitation due to coherent oscillations and space charge which was discussed in Sec. 6.2. Particles gain large transverse amplitudes in the regions where the resonance condition is fulfilled (the incoherent frequency is close the coherent frequency).

8.3.5 Conclusions from the simulation with TFS

In this chapter we discussed the simulation results for the TFS with imperfections. They can be summarized as following:

- the TFS efficiency can be significantly reduced for the case when the system bandwidth does not cover the characteristic width of the bunch spectrum,

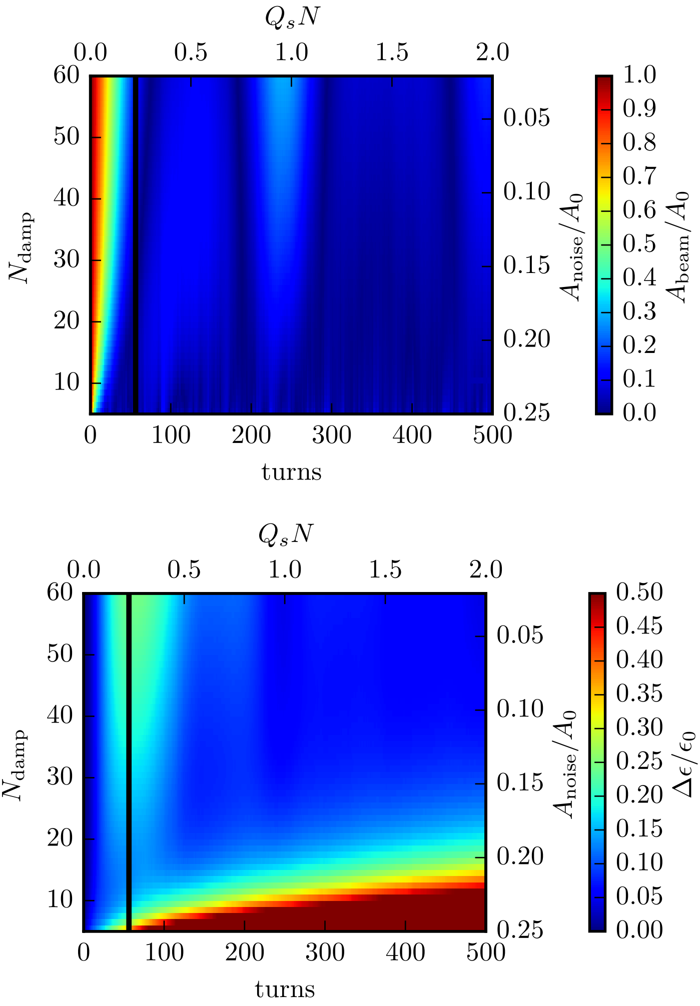

Figure 8.10.: Damping of coherent oscillations after the initial offset using TFS with different gain and noise amplitude. The top plot is the time evolution of offset amplitude, and the bottom plot is the time evolution of the emittance blowup. The solid black lines correspond to $N_{\mathrm{dec0}} \approx 56$ turns. Simulation parameters are $q_{\mathrm{sc}} = 0$, $q_{\mathrm{ic}} = 0$, $q_{\mathrm{eff}} = 1$, $Q_s = 4 \times 10^{-3}$, $Q_{\mathrm{H}} = 512$, and $N_z = 1024$.

- the TFS with the constant delay errors can make a bunch unstable,
- random delay errors due to a jitter do not affect damping efficiency,
- the strong noise in the system results in emittance blowup even if the bunch oscillations are damped,
- space charge and image charges changes the speed of the decoherence process and the shape of intrabunch oscillations. This affect the requirements for the system gain and bandwidth.

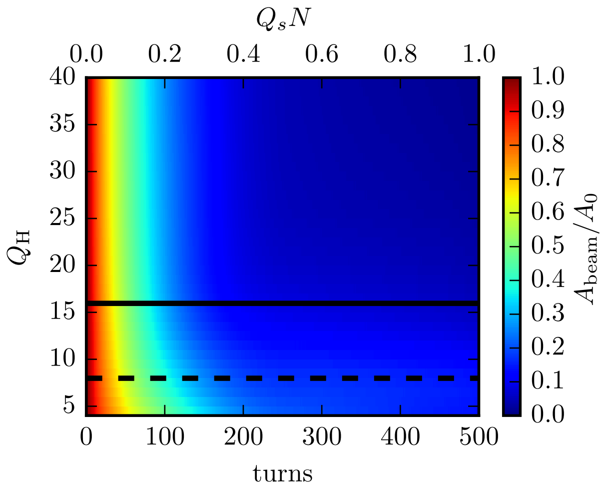

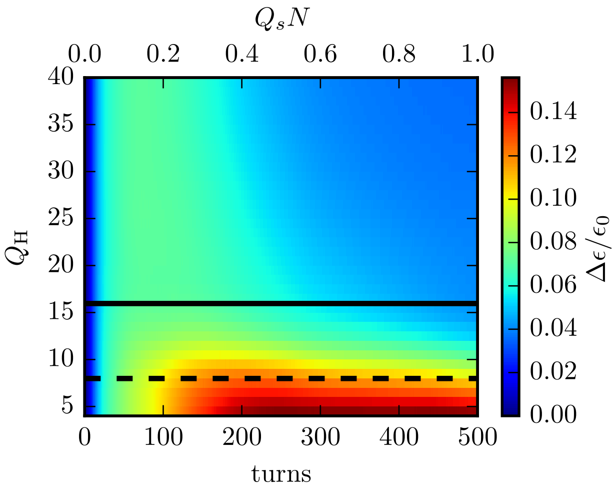

Figure 8.11.: Damping of coherent oscillations after the initial offset using TFS with different high cutoff frequency. The top plot is the time evolution of the offset amplitude, and the bottom plot is the time evolution of the emittance blowup. The lowest high cutoff frequency is $Q_\mathrm{H} = 4$. The solid black lines are $Q_\mathrm{H} = 2q_\mathrm{eff}Q_\mathrm{b}$, and the dashed black lines are $Q_\mathrm{H} = Q_\mathrm{b}$. Simulation parameters are $q_\mathrm{sc} = 8$, $q_\mathrm{ic} = 0.32$, $q_\mathrm{eff} = 1$, $Q_\mathrm{b} = 8$, $Q_s = 4 \times 10^{-3}$, $Q_\mathrm{L} = 0$, and $N_\mathrm{damp} = 60$. For comparison see Fig. 8.6.

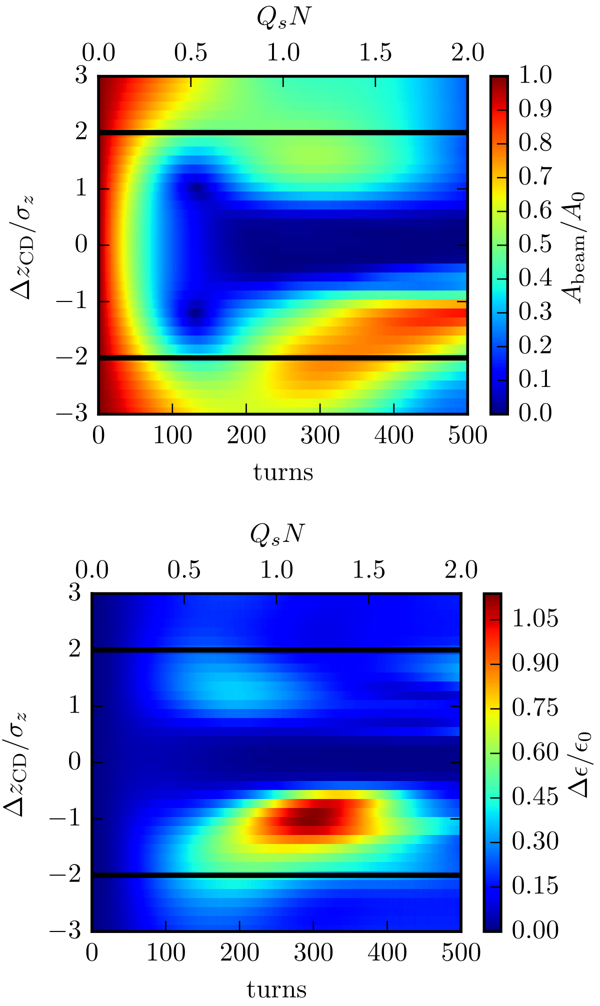

Figure 8.12.: Damping of coherent oscillations after the initial offset using TFS with different constant delays. The top plot is the time evolution of offset amplitude, and the bottom plot is the time evolution of the emittance. The solid black lines are $\Delta z_{\mathrm{CD}}/\sigma_z = \pm 1/2q_{\mathrm{eff}}$. Simulation parameters: $q_{\mathrm{sc}} = 25$, $q_{\mathrm{ic}} = 1$, $q_{\mathrm{eff}} = 1$, $Q_s = 4 \times 10^{-3}$, $Q_{\mathrm{H}} = 512$, $N_{\mathrm{damp}} = 60$, and $N_z = 1024$. For comparison see Fig. 8.9.

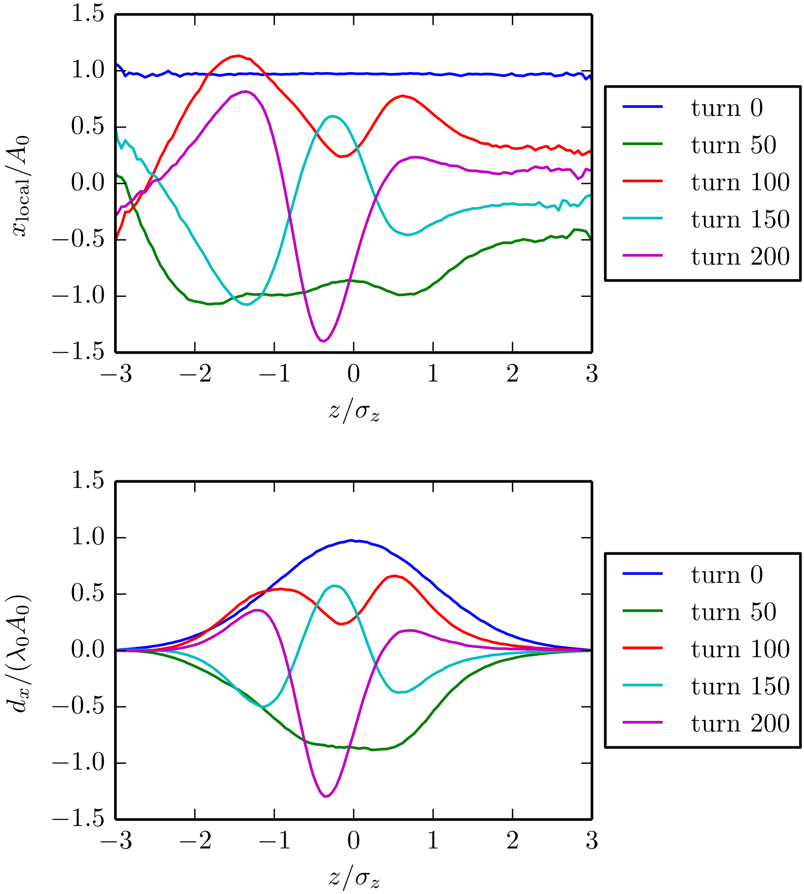

Figure 8.13.: Intrabunch oscillations in the presence of space charge and image charges. The top plot represents the local offset x_{local} along the bunch, and the bottom plot represents the dipole moment d_x along the bunch. Simulation parameters: $q_{\mathrm{sc}} = 25$, $q_{\mathrm{eff}} = 1$, $q_{\mathrm{ic}} = 1$, $Q_s = 4 \times 10^{-3}$, and $Q_{\mathrm{b}} = 8$.

9 Conclusions and Outlook

Decoherence causes the transverse emittance blowup of injected ion bunches in synchrotrons. A detailed understanding of the initial stage of decoherence for intense beams is necessary to determine requirements of transverse feedback systems, which are used to preserve the beam quality.

In the present work decoherence and emittance blowup are studied with a focus on interplay of chromaticity, space charge and image charges for bunched beams. Without intensity effects the relation of the transverse emittance and the oscillation amplitude following an arbitrary initial offset is given by the matched equivalent emittance. We find that a similar relation can be used for intense ion bunches with a modified beam oscillation amplitude during the initial stage of the decoherence process.

For coasting beams, we showed in particle tracking simulations and in our analytical model that the addition of space charge in the pulse response function slows down decoherence process. If the space charge tune shift is larger than the effective tune spread, space charge leads to the loss of decoherence. In the initial stage of decoherence the analytical model reproduces the particle tracking simulations and later deviations can be explained by beam losses and beam halo buildup due to resonant excitation of particles. The latter was illustrated in particle tracking simulations and in a particle-core approach, where we observed the excitation driven by space charge and coherent oscillations. The particles are in resonance when the incoherent tune is close to the coherent tune.

The 2D approach was extended to bunched beams as a longitudinally sliced model with different analytical expressions depending on the effective tune spread parameter q_{eff}, the space charge parameter q_{sc}, and the image charge parameter q_{ic}. In general there is a slower decoherence for stronger space charge. Image charges play no role for $q_{\text{ic}} < 0.5$. For $q_{\text{sc}} \gg q_{\text{eff}}$, decoherence is lost for majority of longitudinal slices, and the bunch offset amplitude does not change within the first synchrotron period. The decoherence process is dominated by image charges when the conditions $q_{\text{sc}} \gg q_{\text{eff}}$ and $q_{\text{ic}} > 1$ are fulfilled. In this case, the bunch offset amplitude decreases due to the coherent tune spread along the bunch. In the intermediate region ($q_{\text{ic}} \approx 1$, $q_{\text{sc}} > q_{\text{eff}}$), decoherence is governed by interplay of chromaticity, space charge and image charges. Simulation results reproduce the analytical expectations in all regimes.

The results of the dedicated experiments in the SIS18 synchrotron at GSI Darmstadt were presented in this work. The decoherence signal were stored for different combinations of machine and beam parameters. It was found that transverse and longitudinal nonlinearities play a minor role in the SIS18 synchrotrons. For the intensities achieved in the experiments it is shown that image charges can be neglected. The main contributors to the initial stage of decoherence process can be identified as chromaticity and space charge. Comparing the time evolution of the beam offset we find that the agreement between measurements and particle tracking simulations is good with the space charge parameter as a free fitting parameter. The measurements confirm the analytical expectations and the simulation results. The estimated space charge tune shift from the measured beam parameters differs from the value given by fitting simulations. This systematic discrepancy is due to uncertainty in the transverse beam size measurements which was the case in previous works [33, 55, 64].

Finally, the damping efficiency of transverse feedback systems was studied in particle tracking simulations. The TFS model with imperfections (a limited bandwidth of the system, delay errors, and noise) was implemented in the PATRIC code. The TFS efficiency can be significantly reduced if the TFS bandwidth does not cover the characteristic width of the bunch spectrum. Delay errors can make a bunch unstable. For a certain signal-to-noise ratio, a TFS produces an additional emittance blowup. Space charge and image charges change the speed of the decoherence process as well as the shape of intrabunch oscillations. This affects the requirements for the TFS gain and the TFS bandwidth.

Further research could focus on experimental studies of decoherence and emittance blowup for specific beam parameters in existing accelerator facilities. In general, the initial stage of decoherence is governed by a combination of different effects. For example, important contributors could be transverse nonlinearities or longitudinal nonlinearities in long bunches.

Acknowledgments

I would like to thank Prof. O. Boine-Frankenheim for offering me a PhD position in TEMF and giving constructive criticism on my work. He successfully guided me to improve scientific skills and supported the participation in conferences. I am grateful to Dr. Vladimir Kornilov for his professional guidance. Thanks to his help I entered the topic of intensity effects in particle beams. Many hours of fruitful discussions with him extremely advanced the present work and inspired me during the last years.

I want to thank Prof. Dr. Shaukat Khan for being the second referee in this thesis. During the PhD Committee meetings he commented my work and gave me important suggestions related to transverse feedback systems.

I thank the graduate school HGS-HIRe for additional training. With the financial support I attended the courses which broadened my knowledge about accelerator physics.

I wish to thank Dr. Vladimir Kornilov, Dr. Rahul Singh, Dr. Piotr Kowina, Dr. Sebastian Ratschow, Dr. Holger Liebermann, Dr. David Ondreka, Dr. Jens Stadlmann, Prof. Dr. Jens Oberrath, Dr. Peter Forck, and Dr. Uwe Niedermayer for the support during measurements in SIS18.

I thank my colleagues at TEMF and GSI for collaboration and for the productive environment. Oliver S. Haas was always open for discussions and had a creative suggestions. Dr. Sabrina Appel encouraged me to use the computer clusters at GSI, which made a great impact on my research. Dr. Paul Görgen helped with computer issues. During my stay in TEMF and GSI I had an opportunity to share offices with many colleagues. I wish to thank Oliver S. Haas, Lewin Eidam, Ivan Prokhorov, Dr. Todorka Banova, Dr. Sabrina Appel, Yun Ouédraogo, Yvonne Späck-Leigsnering, and Yao-Shuo Yuan for creating a good atmosphere.

Special thanks goes to Dr. William D. Stem and Dr. Vladimir Kornilov for proofreading this thesis and improving it with helpful comments.

Finally, I would like to express my gratitude to my family, especially my mother Liudmila Karpova for endless inspiration, my father Evgenii Karpov and sister Svetlana Karpova for encouraging me during all these years.

A Lists

Acronyms

GSI	GSI Helmholtzzentrum für Schwerionenforschung GmbH (Helmholtz center for heavy ion research)
UNILAC	UNIversal Linear ACcelerator
SIS18	SchwerIonenSynchrotron 18 (Heavy ion synchrotron 18)
FAIR	Facility for Antiproton and Ion Research in Europe GmbH
SIS100	SchwerIonenSynchrotron 100 (Heavy ion synchrotron 100)
PS	Proton Synchrotron
CERN	Organisation Européenne pour la Recherche Nucléaire (European Organization for Nuclear Research)
2D	Two Dimensional
rms	Root mean square
rf	Radio Frequency
KV	Kapchinskij-Vladimirskij
BTF	Beam Transfer Function
1D	One Dimensional
BPM	Beam Position Monitor
PATRIC	PArticle TRackIng Code [66]
6D	Six Dimensional
fp	Fixed-position monitoring
PIC	Particle-In-Cell
3D	Three Dimensional
FFT	Fast Fourier Transform
OTM	One-Turn-Matrix
APA	Average Phase Advance
MPI	Message Passing Interface

KRONOS	GSI cluster KRONOS
DC	Direct Current
IPM	Ionization Profile Monitor
MCP	Micro-Channel Plate
TFS	Transverse Feedback System
LPF	Low-pass filter
HPF	High-pass filter
ADC	Analog-to-Digital Converter
DAC	Digital-to-Analog Converter
SI	Système International d'unités (The International System of Units)

Symbols

Units are given in SI (Système international d'unités). An arrow denotes a vectorized quantity, where applicable the same symbol without the arrow is used for the absolute value of the quantity. The symbol $'$ denotes the derivative of the quantity with respect to the coordinate s. A dot over a quantity denotes the derivative of the quantity with respect to time. A mean value is indicated as $\langle\cdot\rangle$. The mean value calculated at the fixed position is denoted $\langle\cdot\rangle_{\mathrm{fp}}$. The indices $_x$ and $_y$ denote the horizontal and the vertical component of the quantity, respectively.

Term	Unit	Description
$\vec{F}$	N	Force
q	C	Charge
$\vec{E}$	V m^{-1}	Electric field
$\vec{v}$	m s^{-1}	Velocity
m	kg	Rest mass
$\vec{B}$	T	Magnetic field
$\vec{p}$	kg m s^{-1}	Momentum
c	m s^{-1}	Speed of light
ρ	m	Bending radius in the magnetic field
β		Relativistic factor $\beta = v/c$
γ		Relativistic factor $\gamma = (1-\beta^2)^{-1/2}$
t	s	Time
s	m	Longitudinal position of the reference particle
$k(s)$	m^{-2}	Quadrupole focusing strength
C	m	Synchrotron circumference

Term	Unit	Description
ϵ_{sp}	m	Single-particle emittance
$\beta(s)$	m	Beta function
$\alpha(s)$		Alpha function
$\gamma(s)$	m^{-1}	Gamma function
$\Psi(s)$		Betatron phase
ψ_0		Initial betatron phase
Q		Betatron tune
Q_0		Bare betatron tune
ϵ	m	Rms beam emittance
σ_x	m	Rms beam size
$\sigma_{x'}$		Rms beam divergence
$\sigma_{xx'}$	m	Correlation
$D(s)$	m	Dispersion function
α_c		Momentum compaction factor
η		Slip factor
ω_0	s^{-1}	Angular revolution frequency
γ_T		Transition γ
T_0	s	Revolution period
ΔQ_ξ		Chromaticity tune shift
ξ		Normalized chromaticity
h		Harmonic number $h = \omega_{\mathrm{RF}}/\omega_0$
V	V	Rf voltage
ϕ_0		Phase of the reference particle
ω_s	s^{-1}	Angular synchrotron frequency
Q_s		Synchrotron tune
N_p		Number of particles per beam
a	m	Beam radius
ϱ	m^{-3}	Density
λ	m^{-1}	Linear density
ε_0	$\mathrm{F\,m}^{-1}$	Vacuum permittivity
μ_0	$\mathrm{N\,A}^{-2}$	Vacuum permeability
J	A^{-2}	Current density
r	m	Radial coordinate
θ		Polar angle
E_{sc}	$\mathrm{V\,m}^{-1}$	Electric field due to space charge
B_{sc}	$\mathrm{V\,m}^{-1}$	Magnetic field due to space charge
F_{sc}	N	Space charge force
r_p	m	Classical particle radius
ΔQ_{sc}		Space charge tune shift parameter

Term	**Unit**	**Description**
I_k		Modified Bessel function of the order k
λ_0	m^{-1}	Peak linear density
b	m	Accelerator pipe radius
I	A	Beam current
ΔQ_{ic}		Image charge tune shift parameter
$Z_\perp$	Ω/m	Transverse dipole coupling impedance
R		Normalized beam transfer function (BTF)
R_0		Normalized BTF without space charge
w		Complex error function
x_n		Coherent mode of number n
Ω	s^{-1}	Angular frequency of the mode
Ω_{fw}	s^{-1}	Angular frequency of the fast wave
Ω_{sw}	s^{-1}	Angular frequency of the slow wave
ΔQ_{coh}		Coherent tune shift
δQ_{sw}		Tune spread of the slow wave
δp	$\mathrm{kg\,m\,s}^{-1}$	Momentum spread
A_0	m	Initial beam offset
ψ		Particle betatron phase
δQ_ξ		Chromaticity tune spread
G_0		Pulse response function
N_{dec0}	turn	Characteristic decoherence time
Δp_i	$\mathrm{kg\,m\,s}^{-1}$	Initial momentum shift of the particle
z_i	m	Initial longitudinal position of the particle
σ_z	m	Rms bunch length
q_ξ		Chromaticity parameter
F_ξ		Envelope of beam oscillations
N_s	turn	Synchrotron period
N_{dec}	turn	Characteristic decoherence time in bunches
sgn		Sign function
K		Normalized initial offset
σ_0	m	Initial rms beam size
ϵ_0	m	Initial rms beam emittance
$\epsilon_{\mathrm{equiv}}$	m	Matched equivalent emittance
$\Delta\epsilon_{\max}$	m	Maximum emittance growth
ΔN	turn	Time delay
q_{eff}		Effective parameter Eq. 3.21
δQ_{eff}		Effective tune spread
G_{b}		Pulse response function for bunches
G		Pulse response function with space charge

Term	**Unit**	**Description**
$\mathscr{H}$		Hilbert transform
p.v.		Cauchy principal value
A_{beam}	m	Beam oscillation amplitude
χ		2D space charge parameter
$G_{\mathrm{b,sc}}$		Bunch pulse response function with space charge
q_{sc}		Space charge parameter
$\Delta\epsilon$	m	Emittance growth
q_{ic}		Image charge parameter
$G_{\mathrm{b,ic}}$		Bunch pulse response function with image charges
Q_{coh}		Local coherent tune
N_{st}		Number of simulation steps per turn
Δs	m	Spatial step
$\Delta x'_{\mathrm{sc}}$		Transverse kick due to space charge
$\Delta x'_{\mathrm{ic}}$		Transverse kick due to image charges
x_{local}	m	Local offset of the beam
$\Delta x'_{\xi}$		Transverse kick due to image charges
Δz	m	Change of the particle longitudinal coordinate
f_{rf}		Normalized acceleration field in the rf cavity
Q_{eff}		Effective particle tune
x_0	m	Beam centroid coordinate
f_{sc}		Normalized space charge force
f_{ξ}		Normalized force due to chromaticity
U_{u}	V	Induced signal on the top BPM plate
U_{d}	V	Induced signal on the bottom BPM plate
U_{l}	V	Induced signal on the left BPM plate
U_{r}	V	Induced signal on the right BPM plate
S_x	mm^{-1}	Horizontal pick-up sensitivity
S_y	mm^{-1}	Vertical pick-up sensitivity
$\hat{U}$		Normalized BPM signal after BRL
$\beta_{x,\mathrm{IPM}}$	m	Horizontal beta function at the position of IPM
$\beta_{y,\mathrm{IPM}}$	m	Vertical beta function at the position of IPM
$D_{x,\mathrm{IPM}}$	m	Dispersion function at the position of IPM
ω_l	s^{-1}	Harmonic of the angular revolution frequency
ω_l^+	s^{-1}	Upper Schottky side band
ω_l^-	s^{-1}	Lower Schottky side band
$Q_{0,\mathrm{frac}}$		Fractional part of the bare tune
$\langle x \rangle_t$	m	Bunch offset calculated from measured data
$\Delta\Psi_{\mathrm{P-K}}$		Phase advance between the pick-up and the kicker
g		Feedback gain

Term	**Unit**	**Description**
N_{damp}	turn	Damping time due to TFS
$\Delta x'_{\mathrm{CK},N+1}$		Correction kick at the turn $N+1$
$(x,x')^{\mathrm{T}}_{\mathrm{K},N+1}$		Beam coordinates at the position of the kicker
$(x,x')^{\mathrm{T}}_{\mathrm{P},N+1}$		Beam coordinates at the position of the pick-up
κ_1		First correction coefficient
κ_2		Second correction coefficient
N_{wait}	turn	Number of waiting turns
$\Delta\epsilon_{\mathrm{TFS}}$	m	Emittance growth in the presence of a TFS
u	m	Normalized delta signal from the pick-up
N_z		Time resolution of the signal
i		Index
d_x	m	Dipole moment of x
$d_{x'}$		Dipole moment of x'
$u_{\mathrm{out},N}$	m	Output signal from the filter at the turn N
$u_{\mathrm{in},N}$	m	Input signal for the filter at the turn N
κ_{HPF}		Coefficient for the high-pass filter
Q_{L}		Low cutoff frequency
κ_{LPF}		Coefficient for the low-pass filter
Q_{H}		High cutoff frequency
N_{SAMP}		Sampling rate
N_{TS}		Number of time samples per digital sample
Δz_{CD}	m	Constant delay error
δN_{RD}	turn	Random delay error
A_{noise}	m	Noise amplitude
Q_{ib}		Normalized frequency of intrabunch oscillations
Q_{b}		Normalized characteristic bunch frequency

List of Figures

List of Tables

Bibliography

[1] A. W. Chao and W. Chou, “Editorial Preface,” *Rev. Accel. Sci. Technol.*, vol. 04, no. 01, pp. v–vi, 2011. [Online]. Available: http://www.worldscientific.com/doi/abs/10.1142/S1793626811000628 1

[2] “Editorial Preface,” *Rev. Accel. Sci. Technol.*, vol. 02, no. 01, pp. v–vi, 2009. [Online]. Available: http://www.worldscientific.com/doi/abs/10.1142/S1793626809000302 1

[3] “Accelerators for America’s Future Report,” *Dep. Energy, USA*, pp. 70–83, 2011. 1

[4] J. D. Cockcroft and E. T. S. Walton, “Experiments with High Velocity Positive Ions. (I) Further Developments in the Method of Obtaining High Velocity Positive Ions,” *Proc. R. Soc. London A Math. Phys. Eng. Sci.*, vol. 136, no. 830, pp. 619–630, 1932. [Online]. Available: http://rspa.royalsocietypublishing.org/content/136/830/619 1

[5] R. Wideröe, “Über ein neues Prinzip zur Herstellung hoher Spannungen,” *Arch. für Elektrotechnik*, vol. 21, no. 4, pp. 387–406, 1928. [Online]. Available: http://dx.doi.org/10.1007/BF01656341 1

[6] J. D. Lawson and G. Brianti, “50 Years of Synchrotrons,” 1997. [Online]. Available: http://cds.cern.ch/record/334108 1

[7] M. Oliphant, “The acceleration of particles to very high energies, Classified memo submitted to DSIR (1943), U. Birmingham Archive.” 1

[8] V. I. Veksler, “A new method of accelerating relativistic particles,” in *Comptes Rendus l’Academie Sci. l’URSS. 43*, 1944, pp. 329–331. 1

[9] E. M. McMillan, “The Synchrotron - A Proposed High Energy Particle Accelerator,” *Phys. Rev.*, vol. 68, no. 5-6, pp. 143–144, sep 1945. [Online]. Available: http://link.aps.org/doi/10.1103/PhysRev.68.143 1

[10] E. Courant and H. Snyder, “Theory of the alternating-gradient synchrotron,” *Ann. Phys. (N. Y).*, vol. 3, no. 1, pp. 1–48, 1958. 1

[11] W. Barth, W. Bayer, L. Dahl, L. Groening, S. Richter, and S. Yaramyshev, “Upgrade program of the high current heavy ion UNILAC as an injector for FAIR,” *Nucl. Inst. Methods Phys. Res. Sect. A*, vol. 577, no. 1-2, pp. 211–214, 2007. 2

[12] K. Blasche and B. Franczak, “The heavy ion synchrotron SIS,” in *Proceedings EPAC 1992*, Berlin, Germany, 1992, pp. 9–13. [Online]. Available: http://accelconf.web.cern.ch/AccelConf/e92/PDF/EPAC1992{_}0009.PDF 2, 63

[13] G. H. Rees, “Injection,” *CAS, Fifth Gen. Acchelerator Phys. Course, Vol 2*, 1995. 2

[14] “www.fair-center.eu.” 3, 105

[15] M. J. Barnes, J. Borburgh, B. Goddard, and M. Hourican, “Injection and extraction magnets: septa,” in *Proceedings, 2009 CAS-CERN Accel. Sch. Spec. course Magnets Bruges, Belgium, June 16 - 25, 2009*, 2011, pp. 167–184. [Online]. Available: http://inspirehep.net/record/891637/files/arXiv:1103.1062.pdf 2

[16] K. Wittenburg, “Halo and Bunch Purity Monitoring,” *Cern Accel. Sch. Rep. No. Cern.*, p. 557, 2008. 3

[17] K. G. Sonnad and J. R. Gary, “Control of beam halo formation through nonlinear damping and collimation,” *Phys. Rev. ST Accel. Beams*, vol. 8, no. 6, pp. 1–10, 2005. 3

[18] H. D. Zhang, R. B. Fiorito, A. G. Shkvarunets, R. A. Kishek, and C. P. Welsch, “Beam halo imaging with a digital optical mask,” *Phys. Rev. ST Accel. Beams*, vol. 15, no. 7, pp. 1–15, 2012. 3

[19] I. Strašík, I. Prokhorov, and O. Boine-Frankenheim, “Beam halo collimation in heavy ion synchrotrons,” *Phys. Rev. ST Accel. Beams*, vol. 18, no. 8, pp. 1–15, 2015. 3

[20] O. S. Brüning, P. Collier, P. Lebrun, S. Myers, R. Ostojic, J. Poole, and P. Proudlock, *LHC Design Report*. Geneva: CERN, 2004. [Online]. Available: https://cds.cern.ch/record/782076 4

[21] R. Rojko, “New Concepts for Transverse Beam Stability in High-Current Heavy-Ion Synchrotrons,” Ph.D. dissertation, TU Darmstadt, 2002. 5

[22] J. M. Cesaratto, J. D. Fox, C. H. Rivetta, D. Alesini, A. Drago, A. Gallo, F. Marcellini, M. Zobov, S. D. Santis, Z. Paret, A. Ratti, H. Qian, H. Bartosik, W. Hofle, and C. Zannini, “SPS Wideband Transverse Feedback Kicker :

Design Report," *Rep. No. SLAC-R-1037*, 2013. [Online]. Available: https://cds.cern.ch/record/1639553/files/CERN-ACC-NOTE-2013-0047.pdf 5

[23] J. D. Fox, J. Dusatko, C. Rivetta, O. Turgut, S. Linear, W. Hofle, U. W. C. Geneva, and S. D. S. L. B. L. Berkeley, "Wideband Vertical Intra-Bunch Feedback At the Sps - 2015 Results and Path Forward," in *Proceedings of IPAC2015*, Richmond, VA, USA, 2015, pp. 1353–1355. 5

[24] E. Keil, W. Schnell, and P. Strolin, *Feedback damping of horizontal beam transfer errors*. Geneva: CERN, 1969. [Online]. Available: https://cds.cern.ch/record/275323 5

[25] L. Vos, "Damping of coherent oscillations," *Nucl. Inst. Methods Phys. Res. Sect. A*, vol. 391, no. 1, pp. 56–63, 1997. 5

[26] J. Belleman, A. Blas, J.-L. Gonzalez, F. Caspers, W. Hofle, T. Kroyer, R. Louwerse, F. Pedersen, V. Rossi, and J. Tuckmantel, "PS transverse damping system for the LHC beams," *Report No. AB-Note-2005-027, CERN*, 2005. 5

[27] E. BENEDETTO, "Emittance growth induced by electron cloud in proton storage rings," Ph.D. dissertation, Polytechnic University of Turin, 2006. 5

[28] E. Métral, "Effect of space charge on Landau damping (talk)," *CARE-HHH-APD Work. GSI*, 2006. 6

[29] E. Metral, "Space charge experiments and benchmarking in the PS," *Cern LIS Meet. 02/04/2007*, pp. 1–29, 2007. 6

[30] E. Métral and H. B. Cern, "Achievable Space-Charge Tune Shift With Long Lifetime in the Cern PS and SPS," in *Proc. HB2008*, Nashville, Tennessee, USA, 2008, pp. 153–156. 6

[31] L. Vos, "Decoherence from space-charge," *CERN-SL-98-056 AP*, no. September 1998, pp. 7–12, 1998. [Online]. Available: https://cds.cern.ch/record/368731/files/sl-98-056.pdf 6, 17

[32] V. Kornilov and O. Boine-Frankenheim, "Transverse decoherence in bunches with space charge," in *Proceedings of HB2010*, Morschach, Switzerland, 2010, pp. 101–105. [Online]. Available: https://accelconf.web.cern.ch/accelconf/HB2010/papers/mopd21.pdf 6

[33] ——, "Transverse decoherence and coherent spectra in long bunches with space charge," *Phys. Rev. ST Accel. Beams*, vol. 15, no. 11, p. 114201, nov 2012. [Online]. Available:

http://arxiv.org/abs/1208.0426http://dx.doi.org/10.1103/PhysRevSTAB.15.114201http://link.aps.org/doi/10.1103/PhysRevSTAB.15.114201 6, 55, 72, 97

[34] G. Stupakov and A. Chao, “Collective Effects and Beam Decoherence Superconducting Super Collider,” *SSC Rep. No. SSCL-621*, no. April, p. 9, 1993. [Online]. Available: http://lss.fnal.gov/archive/other/ssc/sscl-621.pdf 6

[35] ——, “Study of beam decoherence in the presence of head-tail instability using a two-particle model,” in *Proceedings of PAC 1995*, vol. 5. Dallas, TX, USA: IEEE, 1995, pp. 3288–3290. [Online]. Available: http://ieeexplore.ieee.org/lpdocs/epic03/wrapper.htm?arnumber=505857 6

[36] M. Reiser, “Free energy and emittance growth in nonstationary charged particle beams,” *J. Appl. Phys.*, vol. 70, no. 4, p. 1919, 1991. [Online]. Available: http://scitation.aip.org/content/aip/journal/jap/70/4/10.1063/1.349474 6

[37] ——, *Theory and Design of Charged Particle Beams*. Weinheim, Germany: WILEY-VCH, 2008. 6

[38] O. Boine-Frankenheim, “The FAIR Accelerators: Highlights and Challenges,” in *Proceedings of IPAC10*, vol. 10, 2010, p. 2430. [Online]. Available: http://accelconf.web.cern.ch/Accelconf/IPAC10/papers/weyra01.pdf 6

[39] A. Burov and I. Introduction, “Efficiency of feedbacks for suppression of transverse instabilities of bunched beams,” vol. 084402, pp. 1–11, 2016. 6

[40] J. C. Maxwel, “A Dynamical Theory of the Electromagnetic Field,” *JSTOR Philos. Trans. R. Soc. London, Vol. 155*, no. January, pp. 459–512, 1865. [Online]. Available: http://www.jstor.org/stable/10.2307/108892 8

[41] S. Y. Lee, *Accelerator physics*. Singapore: World Scientific Publishing Co. Re. Ltd., 1999. 9, 10, 13, 20

[42] D. A. Edwards and M. J. Syphers, *An Introduction to the Physics of High Energy Accelerators*. Weinheim, Germany: Wiley-VCH Verlag GmbH, jan 2004. [Online]. Available: http://adsabs.harvard.edu/abs/1993iphe.book.....Ehttp://doi.wiley.com/10.1002/9783527617272 10, 27

[43] J. Rossbach and P. Schmüser, “Basic course on accelerator optics,” *Proc. Cern Accel. Sch. Cern*, pp. pp. 17–88, 1994. 12

[44] M. A. Furman, “Electric field of a 2D elliptical charge distribution inside a cylindrical conductor,” *Phys. Rev. ST Accel. Beams*, vol. 10, no. 8, pp. 1–6, 2007. 14

[45] K. Schindl, “Space charge,” *Cern Accel. Sch. Basic Course Gen. Accel. Physics, Loutraki, Greece*, pp. 1–6, 1999. 14, 18

[46] I. Kapchinskij, V. Vladimirskij, I. M. Kapchinsky, and V. V. Vladimirsky, “Limitations of proton beam current in a strong focusing linear accelerator associated with strong space charge,” ... *Conf. High Energy Accel.* ..., pp. 274–288, 1959. 15

[47] M. Chao, A. W. ,Tinger, *Handbook of accelerator physics and engineer*. Singapore: World Scientific Publishing Co. Re. Ltd., 1999. 16, 20

[48] A. Burov and V. Lebedev, “Transverse instabilities of coasting beams with space charge,” *Phys. Rev. ST Accel. Beams*, vol. 12, no. 3, p. 034201, mar 2009. [Online]. Available: http://link.aps.org/doi/10.1103/PhysRevSTAB.12.034201 16

[49] K. Y. Ng, “Space-Charge Tune Shift of a Bi-Gaussian Beam,” *Fermilab Rep. TM-2241*, pp. 0–13, 2004. 16

[50] K. Ng, “Landau Damping of Space-Charge Dominated Fermilab Booster Beam,” in *Proc. HB2008*, Nashville, Tennessee, USA, 2008. [Online]. Available: http://lss.fnal.gov/archive/2008/conf/fermilab-conf-08-410-ad.pdf 17

[51] A. W. Chao, *Physics of Collective Beam Instabilities in High Energy Accelerators*. John Wiley & Sons, Inc., 1993. 19, 20

[52] D. Pestrikov, “Dipole coherent oscillations and fluctuations of a coasting ion beam with strong space charge,” *Nucl. Inst. Methods Phys. Res. Sect. A*, vol. 562, no. 1, pp. 65–75, jun 2006. [Online]. Available: http://linkinghub.elsevier.com/retrieve/pii/S0168900206005274 19

[53] ——, “Self-consistent dipole coherent oscillations of a coasting ion beam with strong space charge,” *Nucl. Inst. Methods Phys. Res. Sect. A*, vol. 578, no. 1, pp. 65–77, jul 2007. [Online]. Available: http://linkinghub.elsevier.com/retrieve/pii/S0168900207011473 19

[54] O. Boine-Frankenheim, V. Kornilov, and S. Paret, “Measurement and simulation of transverse Schottky noise with space charge,” *Phys. Rev. ST*

Accel. Beams, vol. 11, no. 7, p. 074202, jul 2008. [Online]. Available: http://link.aps.org/doi/10.1103/PhysRevSTAB.11.074202 19

[55] S. Paret, V. Kornilov, O. Boine-Frankenheim, and T. Weiland, "Transverse Schottky and beam transfer function measurements in space charge affected coasting ion beams," *Phys. Rev. ST Accel. Beams*, vol. 13, no. 2, p. 022802, feb 2010. [Online]. Available: http://link.aps.org/doi/10.1103/PhysRevSTAB.13.022802 19, 72, 97

[56] K.-Y. Ng, *Physics of Intensity Dependent Beam Instabilities*. World Scientific Publishing Co. Re. Ltd., 2006. [Online]. Available: http://books.google.com/books?id=pXg1{_}7m3{_}UgC{&}pgis=1 19, 20, 23

[57] I. C. Hsu, "The decoherence and recoherence of the betatron oscillation signal and an application," *Part. Accel.*, vol. 34, pp. 43–52, 1990. 22

[58] A. Hofmann, "Landau damping," *CERN Accelerator School, Report No. CERN-1995-006*, p. 275, 1995. [Online]. Available: http://cds.cern.ch/record/302483 23, 30

[59] M. G. Minty, W. L. Spence, and S. Linear, "Injection envelope matching in storage rings," in *Proc. Part. Accel. Conf.*, 1995, pp. 1–3. 27

[60] R. E. Meller, A. W. Chao, J. M. Peterson, S. G. Peggs, and M. Furman, "Decoherence of Kicked Beams," *SSC Rep. No. SSC-N-360*, 1987. [Online]. Available: http://mafurman.lbl.gov/SSC-N-360.pdf 27

[61] M. Minty, A. Chao, and W. Spence, "Emittance growth due to decoherence and wakefields," in *Proceedings of PAC 1995*, vol. 5. Dallas, TX, USA: IEEE, 1995, pp. 3037–3039. [Online]. Available: http://ieeexplore.ieee.org/lpdocs/epic03/wrapper.htm?arnumber=505776 27

[62] V. Kornilov and O. Boine-Frankenheim, "Simulation studies & code validation for the head-tail instability with space charge," in *Proceedings ICAP09*, San Francisco, CA, USA, 2009, pp. 58–63. [Online]. Available: http://epaper.kek.jp/ICAP2009/papers/tu2iopk02.pdf 28

[63] S. Paret, V. Kornilov, and T. Weiland, "Transverse schottky and btf measurements and simulations in space-charge affected coasting ion beams," in *Proceedings of HB2010*, no. 5, Morschach, Switzerland, 2010, pp. 368–372. 30

[64] S. Paret, "Transverse Schottky Spectra and Beam Transfer Functions of Coasting Ion Beams with Space Charge," Ph.D. dissertation, TU Darmstadt, 2010. 30, 68, 97

[65] “https://wiki.gsi.de/Linux/KronosCluster.” 40, 50

[66] O. Boine-Frankenheim and V. Kornilov, “Implementation and Validation of Space Charge and Impedance Kicks in the Code Patric for Studies of Transverse Coherent Instabilities in the Fair Rings,” in *Proceedings of ICAP 2006*, Chamonix Mont-Blanc, 2006, pp. 267–270. [Online]. Available: https://accelconf.web.cern.ch/accelconf/icap06/PAPERS/WEA3MP04.PDF 40, 42, 99

[67] R. W. Hockney and J. W. Eastwood, *Computer Simulation Using Particles*. Bristol, PA, USA: Taylor \& Francis, Inc., 1988. 40, 42

[68] V. Kapin, “A method for numerical solution 2D poissons equation with image fields,” in *Proc. EPAC 2002*, 2002, pp. 1637–1639. 42

[69] B. Montague, “Fourth-Order Coupling Resonance Excited By Space-Charge Forces in a Synchrotron,” 1968. [Online]. Available: http://www.osti.gov/energycitations/product.biblio.jsp?osti{_}id=4814684 45

[70] A. U. Luccio and N. L. D’Imperio, “Eigenvalues of the One-turn Matrix,” Brookhaven National Laboratory, Tech. Rep. December, 2003. 45

[71] R. Bartolini, A. Bazzani, M. Giovannozzi, W. Scandale, and E. Todesco, “Tune evaluation in simulations and experiments,” *Part. Accel.*, vol. 52, pp. 147—-77, 1996. [Online]. Available: http://cdsweb.cern.ch/record/292773?ln=en 45

[72] “see e.g. http://www-unix.mcs.anl.gov/mpi/.” 46

[73] T. P. Wangler, K. R. Crandall, R. Ryne, and T. S. Wang, “Particle-core model for transverse dynamics of beam halo,” *Phys. Rev. ST Accel. Beams*, vol. 1, no. 8, p. 084201, dec 1998. [Online]. Available: http://link.aps.org/doi/10.1103/PhysRevSTAB.1.084201 51

[74] C. K. Birdsall and A. B. Langdon, *Plasma Physics via Computer Simulation*. IOP Publishing Ltd., Bristol, 1991. 53

[75] U. Springer, “High resolution measurement of betatron tune at SIS-18,” Ph.D. dissertation, Goethe university Frankfurt, 2010. 64

[76] P. Forck, P. Kowina, and D. Liakin, “Beam Position Monitors,” *Cern Accel. Sch. Rep. No. Cern.*, pp. 1–42, 2009. 64

[77] T. Giacomini, S. Barabin, P. Forck, D. Liakin, and V. Skachkov, “Development of residual gas profile monitors at GSI,” in *In Proceedings of Beam Instrumentation Workshop*, Knoxville, United States of America, 2004. 64

[78] P. Forck, A. Bank, T. Giacomini, and A. Peters, “Profile monitors based on residual gas interaction,” in *DIPAC 2005*, Lyon, France, 2005. 64

[79] A. Verdier, “Chromaticity,” *CERN Accelerator School, Report No. CERN-1995-006*, p. 275, 1995. [Online]. Available: http://cds.cern.ch/record/302483 67

[80] F. Caspers, “Schottky signals for longitudinal and transverse bunched-beam diagnostics,” *Cern Accel. Sch. Rep. No. Cern.*, 2009. 67, 68

[81] W. Schottky, “Über spontane Stromschwankungen in verschiedenen Elektrizitätsleitern,” *Ann. Phys.*, vol. 362, no. 23, pp. 541–567, 1918. [Online]. Available: http://dx.doi.org/10.1002/andp.19183622304 67

[82] D. Boussard, “Cure of instabilities,” *CERN Accelerator School, Report No. CERN-1995-006*, 1995. 77

[83] L. Vos, “Transverse emittance blow-up from dipole errors in proton machines,” in *EPAC 1998*, no. 6, Stockholm, pp. 1365–1367. [Online]. Available: http://cds.cern.ch/record/359255 78

[84] M. Chanel, R. Maccaferri, and J. Perrier, “Momentum Stochastic Cooling with Digital Notches,” in *EPAC 1990*, Nice, 1990. 81

[85] C. Christiansen, “Closed Orbit Signal Suppressor for the TFS of the PSB,” *CERN/PS/BR.80-05*. 81

Ivan Karpov – Curriculum Vitae

EDUCATION

Technische Universität Darmstadt, **2013 – present**
Darmstadt, Germany

PhD candidate

Thesis title: Damping of coherent oscillations in intense ion beams.

Physics' Department, Novosibirsk State University, **2011 – 2013**
Novosibirsk, Russia

Master's Degree in Physics, GPA is 5.00 out of 5.00

Thesis title: Penetration of the powerful laser pulse into the narrow metal capillary

Physics' Department, Novosibirsk State University, **2007 – 2011**
Novosibirsk, Russia

Bachelor's Degree in Physics, GPA is 4.97 out of 5.00

Thesis title: Formation of an electron beam in a diode with the anode plasma counterflow.

Lyceum 36, Irkutsk, Russia **2004 – 2007**

Complete secondary education, GPA is 4.9 out of 5.00

WORK EXPERIENCE

Computational Electromagnetics Laboratory, **01.10.2013 – present**
TU Darmstadt and GSI Darmstadt, Germany

PhD student

- study of the emittance blowup of the ion bunches after the single turn injection in presence of space charge and image charges.
- study of active damping of the injection errors in synchrotrons with realistic transverse feedback systems.

Accelerator physics' department, **01.08.2011 – 23.09.2011**
GSI Darmstadt, Germany
Summer student

- simulation study of transport of laser accelerated ion beams.

Plasma physics' department Lab.10, **2009 – 2013**
BINP SB RAS, Novosibirsk, Russia
Laboratory assistant

- simulation study of laser wakefield acceleration within a narrow metal capillary.
- study of electron beam generation in a diode with a plasma anode in the Gas-Dynamic Trap.
- development of diagnostics based on an interference filter for measurements of plasma parameters.
- preparation of grant applications and grant reports (project 14.B37.21.0784 supported by The Ministry of education and science of Russia).

SCHOLARSHIPS AND GRANTS

- Scholarship for PhD research, TU Darmstadt	**01.10.2013 – 28.02.2017**
- Scholarship of Dynasty Foundation	**2013**
- Scholarship of academician A.D. Sakharov	**2010 – 2013**
- Scholarship of the Academic Council of NSU	**2010 – 2012**
- Scholarship of Baker Hughes	**2011 – 2012**
- Scholarship of the Government of Novosibirsk Region	**2012**
- Grant for participation in 31st Summer Student Program at GSI Darmstadt	**2011**

PUBLICATIONS

- I. Karpov, V. Kornilov, O. Boine-Frankenheim. Early transverse decoherence of bunches with space charge, Phys. Rev. Accel. Beams 19, 124201 (2016).
- I. Karpov, V. Kornilov, O. Boine-Frankenheim. Emittance growth in bunches with space charge due to damping of transverse oscillations, volume 2015-1 of GSI Report. GSI Helmholtzzentrum für Schwerionenforschung, Darmstadt, 2015.
- I. Karpov, V. Kornilov, O. Boine-Frankenheim. Transverse decoherence of ion bunches with space charge and feedback system, Proceedings of HB2014, East-Lansing, MI, USA, 2014.

ORAL PRESENTATIONS

- I. Karpov, V. Kornilov, O. Boine-Frankenheim. Transverse decoherence with space charge, in the DPG Spring meeting, Darmstadt, 2016.
- I. Karpov, V. Kornilov, O. Boine-Frankenheim. Emittance growth in bunches with space charge due to damping of transverse oscillations, in EuCARD2/XBeams Workshop on Space Charge, Oxford, 2015.
- I. Karpov, V. Kornilov, O. Boine-Frankenheim. Transverse decoherence and emittance growth of ion bunches with space charge, in the DPG Spring meeting, Wuppertal, 2015.
- I. Karpov. Decoherence of kicked beams with space charge, in HGS-HIRe Graduate Days, Nonnenau, 2015.

SCHOOLS AND COURSES

- CERN Accelerator school, Intensity Limitations in Particle beams, CERN, Switzerland, 2015.
- CERN Accelerator school, Advanced Accelerator Physics, Warsaw, Poland, 2015.
- HGS-HIRe Soft skill courses I,II,III, Buchenau, Germany, 2014 - 2015.
- CERN Accelerator school, Introduction to Accelerator Physics, Prague, Czech Republic, 2014.
- HGS-HIRe Lecture Week on Accelerator Physics, Ronneburg, Germany, 2014.

COMPUTER SKILLS

- Programming: C/C++, Python, Cython, MPI, Shellscript (Bash).
- Scientific Computing: Parallelization (MPI), Slurm, Lustre, Numpy, Mathematica, Particle tracking simulations (PATRIC, PyORBIT, MAD-X).

PERSONAL DETAILS

- Date of birth: 25.06.1990
- Citizenship: Russian, Polish
- Languages: Russian (native), English (fluent), Polish (fluent), German (intermediate)
- Hobbies: Salsa, Aikido, triathlon, running